# Soft core-shell particles at fluid interfaces: theory and experiment

Inaugural-Dissertation

zur Erlangung des Doktorgrades
der Mathematisch-Naturwissenschaftlichen Fakultät
der Heinrich-Heine-Universität Düsseldorf

vorgelegt von

**Jannis Hendrik Kolker**
aus Dortmund

Düsseldorf, Juni 2022

aus dem Institut für Theoretische Physik II: Weiche Materie
der Heinrich-Heine-Universität Düsseldorf

Gedruckt mit der Genehmigung der
Mathematisch-Naturwissenschaftlichen Fakultät der
Heinrich-Heine-Universität Düsseldorf

Referent: Prof. Dr. Hartmut Löwen

Korreferent: Prof. Dr. Liesbeth M.C. Janssen

Tag der mündlichen Prüfung: 20.09.2022

# Abstract

In the research field of condensed matter, soft core-shell systems represent a wide range of complex systems with fundamental and applied relevance. Whether in general or in the case of specifically polymeric structured systems, such as microgels or polymer-grafted cores (hairy particles), core-shell systems offer a wide range of phenomena and effects at all levels of coarseness. In combination with the effects of an acting fluid interface on the core-shell system, static and dynamic phenomena such as forming effects of coronae at the interface and hysteresis can occur.

Therefore, this thesis is divided into two parts, on the one hand core-shell systems in contact with a fluid interface are investigated for their elastic properties in general and on the other hand more structured systems, such as microgels or polymer grafted cores (hairy particles), are investigated for their special (bulk) properties at the interface. This investigation ranges from the (static) interaction at the interface of coronae to (dynamic) hysteresis effects when the solvent conditions change.

The general investigation of a coarse-grained core-shell system with a coupled architecture at an (equatorially acting) interface provides a complete analysis of the linear response to such an interfacial loading and includes the investigation of the deformation behaviour for different stiffnesses as well as different size ratios for the core and the shell. Different Poisson ratios including different degrees of auxeticity are also analysed, giving insight into the deformation behaviour of such a material/systems. In addition, the stress field is investigated, revealing inhomogeneous stress behaviour within the deformed core-shell system.

However, the study of polymeric structured systems, such as microgels or polymer-grafted cores (hairy particles), and their properties provides insight into how their (static) bulk phenomena are affected by the presence of an fluid interface. While both systems form a corona at the interface in a (more) diluted situation (single-body system), microgels show core-hysteresis for their widely studied bulk volume phase transition. Furthermore, they (microgels, as a many-body system) induce different types of interactions between interfaces for different solvent conditions. In this thesis, the core-hysteresis is quantified by the lateral expansion and the surface pressure at the interface, while the induced interaction between two interfaces packed with microgels is verified by the effective osmotic pressure between the two interfaces.

The (single-body) core-hysteresis is further investigated as a function of the crosslinker density, revealing that a lower crosslinker density causes a larger amount of hysteresis. No hysteresis is found in the comparative situation in the bulk.

Therefore, the adsorbed initial state is considered as a particular kinetically trapped state.

However, the interaction between the interfaces is studied in more detail as a function of the density of the microgel itself (in the many-body system and the solvent conditions), for which different osmotic pressures occur. In particular, when the microgel packing is (more) diluted and solvent conditions are poor, a negative osmotic pressure is found, while in all other situations (dense microgel packing and/or good solvent conditions) a positive osmotic pressure occurs.

For the polymer grafted cores (hairy particles), the effective interaction between the core and the interface is explicitly investigated under good solvent conditions, resulting in an equilibrium distance of the core to the interface. In addition, the effective pair interaction between the two cores induced by the corona formed at the interface is analysed and found to be repulsive. A similar set-up in the bulk also reveals a repulsive effective pair interaction. Established effective pair interactions such as the Jagla or star polymer interaction are fitted to the data and provide information on effective (intrinsic) parameters such as the effective corona and core size or the effective softness of the Jagla potential.

# Kurzfassung

Im Forschungsbereich der kondensierten Materie stellen weiche Kern-Schale Systeme eine breite Palette komplexer Systeme mit fundamentaler und angewandter Relevanz dar. Ob im Allgemeinen oder im Fall spezifischer (polymerisch) strukturierter Systeme, wie Mikrogele oder polymergepfropfte Kerne (haarige Partikel), Kern-Schale Systeme bieten eine große Bandbreite an Phänomenen und Effekten in allen Stufen des Coarse Graining. In Kombination mit den Auswirkungen einer wirkenden Flüssigkeitsgrenzfläche (auf das Kern-Schale System) können statische und dynamische Phänomene wie Verformungseffekte zu Koronae und Hysteresen auftreten.

Daher ist diese Arbeit zweigeteilt, zum einen werden Kern-Schale Systeme, die in Kontakt mit einer flüssigen Grenzfläche stehen auf ihre elastischen Eigenschaften im Allgemeinen untersucht und zum anderen werden stärker strukturierte Systeme, wie Mikrogele oder polymergepfropfte Kerne (haarige Partikel), auf ihre speziellen (Bulk-)Eigenschaften an der Grenzfläche hin untersucht. Diese Untersuchung reicht von der (statischen) Wechselwirkung an der Grenzfläche der Koronae bis hin zu (dynamischen) Hystereseeffekten bei einer Änderung der Lösemittelbedingungen.

Die allgemeine Untersuchung eines vergröberten Kern-Schale Systems mit einer gekoppelten Architektur an einer (äquatorial wirkenden) Grenzfläche bietet eine vollständige Analyse der linearen Reaktion auf eine Grenzflächenbelastung und umfasst die Untersuchung des Verformungsverhaltens für unterschiedliche Steifigkeiten sowie unterschiedliche Größenverhältnisse für den Kern und die Schale. Es werden verschiedene Poissonzahlen einschließlich verschiedener Auxetizitätsgrade analysiert, welche Einblicke in das Verformungsverhalten eines solchen Materials geben. Darüber hinaus wird das Spannungsfeld untersucht, welches ein inhomogenes Spannungsverhalten innerhalb des verformten Kern-Schale Systems offenbart.

Die Untersuchung strukturierter Polymersysteme, wie Mikrogele oder polymergepfropfte Kerne (haarige Partikel), und ihrer Eigenschaften gibt Aufschluss darüber, wie ihre (statischen) Bulkeffekte durch das Vorhandensein einer Grenzfläche beeinflusst werden. Während sich bei beiden Systemen in einer verdünnten Situation (Einkörpersystem) an der Grenzfläche eine Korona bildet, zeigen Mikrogele eine Kernhysterese für ihren (vielfach untersuchten) Volumenphasenübergang. Darüber hinaus induzieren sie (Mikrogele als Vielkörpersystem) verschiedene Arten von Wechselwirkungen zwischen Grenzflächen bei unterschiedlichen Lösemittelbedingungen. Die Kernhysterese wird in dieser Arbeit durch die laterale Ausdehnung und den Oberflächendruck an der Grenzfläche quantifiziert, während die induzierte

Wechselwirkung zwischen zwei, mit Mikrogelen besetzen, Grenzflächen durch den effektiven osmotischen Druck zwischen den beiden Grenzflächen nachgewiesen wird.

Die (Einkörper-)Kernhysterese wird in Abhängigkeit von der Vernetzerdichte näher untersucht, wobei sich zeigt, dass eine geringere Vernetzungsdichte eine größere Hysterese verursacht. Bei den Vergleichssituationen im Bulk wird keine Hysterese festgestellt. Daher wird der adsorbierte kollabierte Ausgangszustand als ein besonderer, kinetisch arretierter Zustand betrachtet. Die Wechselwirkung zwischen den Grenzflächen wird in Abhängigkeit von der Dichte der Mikrogele selbst (im Vielkörpersystem und den Lösungsmittelbedingungen), für die unterschiedliche osmotische Drücke auftreten, genauer untersucht. Insbesondere bei einer verdünnten Mikrogelpackung und schlechten Lösemittelbedingungen wird ein negativer osmotischer Druck festgestellt, während in allen anderen Situationen (dichte Mikrogelpackung und/oder gute Lösemittelbedingungen) ein positiver osmotischer Druck beobachtet wird.

Für die polymergepfropften Kerne (haarige Partikel) wird die effektive Wechselwirkung zwischen dem Kern und der Grenzfläche unter guten Lösungsmittelbedingungen explizit untersucht, wobei sich ein Gleichgewichtsabstand des Kerns zu der Grenzfläche ergibt. Außerdem wird die effektive Paarwechselwirkung zwischen den beiden Kernen, die durch die an der Grenzfläche gebildete Korona hervorgerufen wird, analysiert und als abstoßend quantifiziert. Eine ähnliche Situation im Bulk zeigt ebenfalls eine abstoßende effektive Paarwechselwirkung. Etablierte effektive Paarwechselwirkungen wie die Jagla- oder Sternpolymerwechselwirkung werden an die Daten gefittet und geben Aufschluss über effektive (intrinsische) Parameter wie die effektive Korona- und Kerngröße oder die effektive Weichheit des Jagla-Potentials.

# Eidesstattliche Versicherung

Ich versichere an Eides Statt, dass die Dissertation von mir selbständig und ohne unzulässige fremde Hilfe unter Beachtung der „Grundsätze zur Sicherung guter wissenschaftlicher Praxis an der Heinrich-Heine-Universität Düsseldorf“ erstellt worden ist.

Düsseldorf, ____________________ ____________________________

# Preface

The content of this dissertation is based on articles and appendix Chapters that I co-authored, and that have been published in / submitted to peer-reviewed scientific journals or contain data and result, which will be published. The articles are reproduced in Chapter 2 and are listed in the following (in topical order):

- **P1** J. Kolker, J. Harrer, S. Ciarella, M. Rey, M. Ickler, L. M. C. Janssen, N. Vogel and H. Löwen, *Interface-induced hysteretic volume phase transition of microgels: simulation and experiment*, Soft Matter, 2021, **17**, 5581-5589.
- **P2** J. Kolker, L. Fischer, Andreas M. Menzel and H. Löwen, *Elastic Deformations of Spherical Core-Shell Systems Under an Equatorial Load*, Journal of Elasticity, 2022, DOI:10.1007/s10659-022-09897-1.

My contributions to these scientific articles are specified in Chapter 2.

The appendix Chapters are attached in Chapter 3 and are listed in the following (in topical order):

- 3.1 *Microgels trapped between two interfaces.*
- 3.2 *Hairy particles at interfaces.*

My contributions to these scientific appendix Chapters are specified in Chapter 3.

# Acknowledgments

First of all, I would like to thank Prof. Hartmut Löwen for the opportunity to do my doctorate at his chair. I am also indebted to him for the exciting topic and the supervision of the thesis. Furthermore, I would like to thank Prof. Liesbeth M. C. Janssen for co-supervising the thesis. Together with her and Simone Ciarella, to whom I am also indebted, I had many helpful discussions regarding the simulative implementation of my research topic and a nice visit to Eindhoven at the beginning of my thesis. I would also like to thank Isha Malhotra, who took on my project as part of the collaboration. I would also like to thank Prof. Nikolas Vogel, Johannes Harrer, Marcel Rey and Maret Ickler for the many helpful discussions, also regarding the experimental implementation of the system under consideration. Further thanks go to Prof. Andreas M. Menzel and Lukas Fischer for their support and cooperation in a joint analytical project. Furthermore, I would like to thank the staff of the Institute of Theoretical Physics II for the productive working atmosphere and the many professional discussions and good advice. Special thanks also go to Claudia Stader and Joachim Wenk for their administrative support and to Jens Grauer, Alexander Sprenger and Paul Monderkamp for helpful discussions and proofreading of this thesis. Finally, I would like to thank my family for their emotional support.

# Contents

# Chapter 1

# Introduction

Core-shell systems are an essential part of soft condensed matter research. The preparation of such systems can be done in many various ways [1, 2]. These include spherical colloidal particles with a polymer coating [3–5], micelles [6] or as polymer networks with different degrees of cross-linking in the inner and outer parts [7–9]. In particular, the latter can be used by the applied side for dynamic and reversible emulsion stabilisers [10–14] or as vehicles for drug delivery [15, 16], as they have the property of adsorbing and releasing molecules. But in general, soft-core shell systems are not limited to these applications, microreactors [17, 18] and smart elastic materials [19, 20] represent another area on the application side. Core-shell systems can also be used as model systems for square-shoulder-like interactions [21–31] and can therefore be used as toy models for basic question in the field of statistical mechanics/physics [3, 16, 32, 33]. Microgels represent a special part in this range of core-shell toy models, as they can be used in the context of crystal lattice melting [34, 35], solid-solid transition [36] and complex self-assembly [37–39].

A commonly used class of microgels are PNiPAm microgel particles which undergo a volume phase transformation in aqueous dispersions at 32 °C. This volume transformation is supported by experimental studies [40–43], computer simulations [41, 44–56] and statistical theory [57–64]. While this property is a very specific feature of a soft core-shell particle group, there is another, more fundamental property for which soft particles are also commonly used: auxetic materials. These materials have the unique property of expanding or contracting perpendicular to the direction of tension or compression, respectively, and can be identified, constructed and analysed [65–68].

These rich fundamental phenomena and application-related effects can be extended when these systems are brought into contact with interfaces. Interfaces themselves also represent complex systems with different properties, and the interaction between an interface system and complex (soft) bulk structures is a heavily studied area of research. For adsorbed core-shell particles, an attractive interface expands the particle in the lateral direction and acts like an expansion in a radially outward symmetric arrangement [69–71]. There is a wide range of applications specifically for PNiPAm microgels in contact with interfaces, from emulsion stabilisation [10–12] to surface structuring [37, 72, 73]. As the isotropy is broken in an adsorbed microgel, ”fried-egg”-like structures are formed in which the core and shell are deformed into a disc-like shape and a quasi two-dimensional layer results, referred as corona. When a microgel is adsorbed at an interface, the volume phase transition (of the single microgel) is strongly hindered by the presence of an interface. These phenomena are conjectured by experimental [70, 74, 75] and numerical findings [70, 76, 77]. Moreover, such an interfacial microgel system generates (core) hysteresis in lateral expansion and surface pressure (Publication **P1**).

The same formation at the interface (corona) applies to polymer-grafted cores, referred as hairy particles [78–81], at an interface [82]. Many body systems of such adsorbed polymeric grafted cores (hairy particles) form a large variety of different packing phases at interfaces [82]. Although the underlying pair interaction potential is assumed to be Jagla-like [83], the study of the pair potential at the interface for monomer-resolved coronae provides an interesting and detailed insight into this effect and gives the opportunity to compare the Jagla approach with other (predicted) pair potentials, such as the star polymer potential [84–86].

In this thesis, mainly core-shell particle systems at interfaces are studied. The microscopic details of the interface formed by two immiscible fluids are given here in a coarse-grained phenomenological approach to model the interface. The analysis of the systems in contact with the interface is structured in two ways, first the deformation of a (coarse-grained) core-shell system under an equatorial interface-like loading is investigated in Publication **P2**. This investigation is carried out in the framework of linear elasticity theory and extends previous approaches for single particles [87] and hollow capsules [88]. In this study, a complete analytical solution of the deformation is provided and a detailed analysis of the deformation behaviour for different stiffnesses and size ratios of the core and shell is given. Moreover, different Poisson ratios are investigated, ranging from incompressible to highly auxetic deformation, and the stress field of the loaded core-shell system reveals a inhomogeneity in the behaviour of the system.

Second, in Publication **P1** and the Chapters 3.1 and 3.2 polymer-structured core-shell systems such as microgels and polymer-grafted cores (hairy particles) are investigated. In Publication **P1**, for a single adsorbed monomer-resolved microgel (and linear polymer), the dynamic behaviour is analysed for the volume phase transition at an interface initiated by a change in solvent conditions. For this transition, hysteresis was recently found in experiments [70,89] and is also confirmed in this thesis from the simulation side (Publication **P1**). Furthermore, the hysteresis is investigated as a function of the crosslinker density (in the microgel up to the linear polymer) and it is found that a larger amount of hysteresis occurs at a lower degree of crosslinking. It is therefore assumed that the collapsed adsorbed state of the microgel is a kinetically trapped state.

Furthermore, in Chapter 3.1, slit-like configurations of two interfaces with different packings of adsorbed (monomer-resolved) microgels are analysed in relation to the induced osmotic pressure between the two interfaces for different solvent conditions. In the specific case of a diluted packing and poor solvent conditions, a negative osmotic pressure is induced, while in all other cases a positive osmotic pressure occurs. In Chapter 3.2 (monomer-resolved) polymer-grafted cores (hairy particles) are studied under good solvent conditions. This investigation ranges from the analysis of the effective core-interface interaction (the equilibrium distance of the core to the interface), to the effective pair interaction at the interface (in the equilibrium position) and in the bulk. In both cases, the pair interactions are found to be repulsive.

In the following, the physical background is established for the phenomena discussed in this thesis. Next, the methods used in this thesis are described. In the second Chapter, the scientific publications are reproduced and in the third Chapter the scientific appendices are presented. In the last Chapter, the conclusion of this thesis is given.

## 1.1 Background

In this section, the physical background of the underlying effects is briefly discussed. First, the physical understanding of an interface and the associated description is given, and then the different types of materials that are modelled to be in contact with the interface are introduced.

### 1.1.1 Interfaces

Interfaces can be assigned to microscopic *interphase* regions of condensed matter. These regions arise when the attractive forces between molecules are stronger than the thermal aggregation [90]. In classical soft matter physics, this can be assigned to liquid-fluid and solid-fluid systems. Although the exact location of the interface is not well defined, the concept of a theoretical two-dimensional interface (in a three-dimensional environment) is very fruitful [91]. At the boundary region between condensed and non-condensed matter (interface), cohesive forces become important because the attractive force of a condensed molecule at the interface is reduced by half compared to its bulk number of neighbours. Thus, if the area $A$ of the interface is increased by the area $dA$ (molecule size), more molecules are involved in the interface forming effect and lose about half of their cohesive energy. This amount of lost cohesive energy per molecule area is defined as surface tension $\gamma$, which serves as a (macroscopic) thermodynamic quantity. Following the literature [90], the thermodynamic work required to expand an interface is defined as follows,

$$\mathrm{d}W = \gamma \mathrm{d}A. \tag{1.1}$$

Furthermore, note that there is a slight difference in the formation conditions for a liquid-fluid and a solid-fluid interface. Since the molecules of the liquid phases have a sufficiently large freedom of movement, the density of the interface molecules is constant [92–95]. In contrast, in solids the number of interfacial molecules is approximately constant due to the strong intermolecular bonds, but the density is not [92–95]. Because of these conditions both systems, but in particular liquid-fluid interfacial systems, strive to minimise their surface area. In the case of incompressible liquids, this occurs under volume-preserving conditions.

In addition to understanding the surface tension $\gamma$ as the (macroscopic) amount of cohesive energy per area, this quantity can also be understood as a vectorial repulsive force per length $\boldsymbol{\gamma} = \gamma \hat{\mathbf{m}}$, with the unit conormal vector $\hat{\mathbf{m}} = \hat{\mathbf{n}}_I \times \hat{\mathbf{t}}$, where $\hat{\mathbf{n}}_I$ is the unit vector normal and $\hat{\mathbf{t}}$ is the unit vector tangential to the interface. Therefore, $\boldsymbol{\gamma}$ represents a repulsive force per length that attempts to minimise the interface. In the literature, these forces are referred as capillary forces [90], and the thermodynamic work (for a rectangular area extension) is then defined as,

$$\mathrm{d}W = 2\boldsymbol{\gamma} \cdot l \mathrm{d}\mathbf{r} \tag{1.2}$$

where $2l\mathrm{d}\mathbf{r}$ is the extended (rectangular) area with $l$ being a finite side length and $\mathrm{d}\mathbf{r}$ being the (orthogonal) direction of extension. The factor 2 reflects the occurrence of two interfaces.

In the case of a system with three (liquid/fluid) components, see Figure 1.1, the Neumann triangle method [90] gives the following equilibrium condition for the three interfacial forces per length (between the two phases $i$ and $j$) $\boldsymbol{\gamma}_{ij}$ with $i, j = 1, 2, 3$,

$$\boldsymbol{\gamma}_{12} + \boldsymbol{\gamma}_{23} + \boldsymbol{\gamma}_{31} = \mathbf{0}. \tag{1.3}$$

This condition results from the mutual cancellation of the interface forces per length at their intersection in equilibrium. Since the three forces per length form a triangle, geometry dictates the relationships $\gamma_{ij} \leq \gamma_{jk} + \gamma_{ki}$ with $i, j, k = 1, 2, 3$ (triangle inequalities) for an equilibrium configuration of the three-phase system. Assuming phase 2 to be an incompressible liquid droplet within a system of two immiscible fluids 1 and 3, certain limits can be derived for this phase. The limit of $\gamma_{12} > \gamma_{23} + \gamma_{31}$ corresponds to the positioning of the droplet in the fluid phase 3 and for $\gamma_{23} > \gamma_{31} + \gamma_{12}$ to the droplet position in the fluid phase 1. However, the condition $\gamma_{31} > \gamma_{12} + \gamma_{23}$ stands for the complete spreading of the droplet at the interface of the two fluid phases 1 and 3 and thus represents a special case.

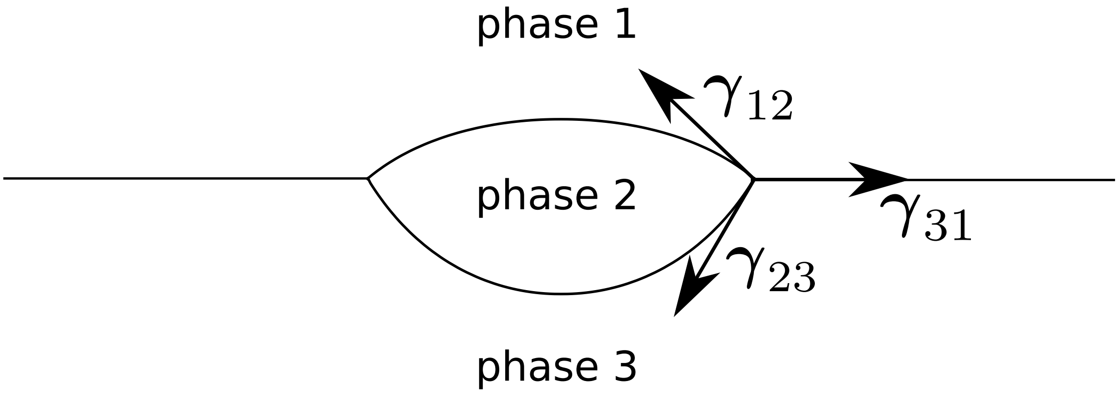

Figure 1.1: Schematic sketch of a three liquid/fluid component system.

Furthermore, if the droplet (phase 2) is considered as a rigid particle, which means that the two interfacial forces per length $\boldsymbol{\gamma}_{12}$ and $\boldsymbol{\gamma}_{23}$ are considered as antiparallel, then (1.3) simplifies to the Young-Dupré relation [90, 96],

$$\gamma_{31} \cos(\theta) + \gamma_{23} = \gamma_{12} \tag{1.4}$$

where $\theta$ is the angle between the surface of the rigid droplet and the interface formed by the immiscible fluid phases 1 and 3. Due to the rigidity of the droplet, the spreading at the interface is suppressed [87]. Therefore, only the two cases of complete positioning in the fluid phase 1 or 3 are the limiting cases. For highly attractive interfaces ($\gamma_{31} > \gamma_{12} + \gamma_{23}$), for which a liquid droplet would spread, new effects occur for a droplet (phase 2) with finite elasticity, e.g. the formation of a corona at the interface. It is assumed that such a coronal structure forms when the fluid interface has such a high surface tension that neither the Young-Dupré relation nor the Neumann triangle method are sufficient to describe the interfacial effects. Therefore plastic effects occur [87].

In the monomer-resolved simulations in Publication **P1** and the Chapters 3.1 and 3.2, the interface is modelled as an external potential $V_{\text{ext}}$ in the $z$ direction. In detail,

$$V_{\text{ext}}(\tilde{z}) = \begin{cases} V_{\text{LJ}}(\tilde{z}) & \tilde{z} \geq \tilde{z}_a \\ V_{\text{LJ}}(\tilde{z}_a) + (\tilde{z}_a - \tilde{z}) \left.\frac{dV_{\text{LJ}}(\tilde{z})}{d\tilde{z}}\right|_{\tilde{z}=\tilde{z}_a} & \tilde{z} < \tilde{z}_a \end{cases} \tag{1.5}$$

with a Lennard-Jones potential

$$V_{\text{LJ}}(\tilde{z}) = 4\varepsilon_{\text{ext}} \left[ \left(\frac{\sigma_{\text{ext}}}{\tilde{z}}\right)^{12} - \left(\frac{\sigma_{\text{ext}}}{\tilde{z}}\right)^{6} \right], \tag{1.6}$$

where $\varepsilon_{\text{ext}}$ is an attractive energy strength, $\tilde{z} = z - 2^{\frac{1}{6}}\sigma_{\text{ext}}$ is a shifted coordinate, $\sigma_{\text{ext}}$ is an effective interaction length, and $\tilde{z}_a$ is a matching point, for which the

the Lennard-Jones part and the steep linear part (and their derivatives) merge continuously. The interface favours the positioning of the resolved monomers at $\tilde{z} = 0$, in the minimum of the potential. The attractive energy strength $\varepsilon_{\text{ext}}$ takes the same role as the surface tension $\gamma_{31}$ in this modelling, since the reduction of the interface area $\mathrm{d}A$ is mimicked by the energetically favourable positioning of a resolved monomer at the minimum of the external potential $V_{\text{ext}}$, thus occupying a finite area at the interface. To ensure a stiff minimum corresponding to a sharp interface, $\sigma_{\text{ext}}$ is chosen to be $0.5\sigma$. The strength of the attraction energy is set to $\varepsilon_{\text{ext}} = 5.5\varepsilon$ to ensure sufficiently strong adsorption at the interface, see Publication **P1**. The simulation units for length and energy are $\sigma$ and $\varepsilon$. In addition to the simulated situation of $\gamma_{31} > \gamma_{12}, \gamma_{23}$, the interfacial potential $V_{\text{ext}}$ also mimics the situation $\gamma_{12} > \gamma_{23}$ with phase 1 for negative $\tilde{z}$ values. The steep linear increase in this region mimicking a large difference in chemical potential between the two phases 1 and 3 and thus a large surface tension $\gamma_{12}$ (compared to $\gamma_{23}$). The additional effects that would arise from the influence of further surface tensions considerations are neglected due to the mimicked situation. The steep linear part of the potential that mimics the chemical potential is discussed and modelled differently in Publication **P1** and the Chapters 3.1 and 3.2.

For the coarse-grained spherical core-shell system in Publication **P2**, the surface tension of the interface of phase 1 and 3 is modelled as a force per length $\boldsymbol{\gamma}_{31}$ acting at the equator of the surface of the system. In detail,

$$\boldsymbol{\gamma}_{31} = \frac{\lambda}{R_{\text{s}}} \delta \left( \theta - \frac{\pi}{2} \right) \mathbf{n} \tag{1.7}$$

with $\lambda$ as the amplitude of the equatorial force per length, $R_s$ as the radius of the shell, $\delta$ as the Dirac delta distribution, $\theta$ as the polar angle and $\mathbf{n}$ as the normal vector of the undeformed spherical system. Here the surface tensions $\boldsymbol{\gamma}_{12}$ and $\boldsymbol{\gamma}_{23}$ are assumed to be equal but neglected.

### 1.1.2 Soft materials

On the mesoscopic scale, elastic soft materials are assumed to be continuous regardless of their microscopic structure. Furthermore, most of these elastic materials respond linearly to small loads [97]. Within this linear range, their continuum mechanics can be described by various elastic moduli, e.g. the Young's modulus $E$, the shear modulus $\mu$, the bulk modulus $K$ and the Poisson ratio $\nu$. All these moduli are generally known and measured by experiments for different classes of materials. The elastic modulus $E$ provides information about the response to a load perpendicular to the elastic material and the shear modulus $\mu$ to a shear load. A compression is quantified by the compression modulus $K$ and the Poisson ratio $\nu$ provides information about the deformation perpendicular to the tensile direction. A linear relationship between the strain (derived from the deformation) and the stress is referred as Hooke's law [97] in the literature, for more details see section (1.2.2). For homogeneous and isotropic materials, Hooke's law provides a constitutive equation for which two elastic moduli are sufficient for description. In detail, the constitutive equation is given by

$$\frac{E}{1+\nu}\left(\underline{\boldsymbol{\epsilon}}+\frac{\nu}{1-2\nu}\mathrm{Tr}\left(\underline{\boldsymbol{\epsilon}}\right)\underline{\mathbf{I}}\right)=\underline{\boldsymbol{\sigma}}, \tag{1.8}$$

where $\underline{\boldsymbol{\sigma}}$ is the stress tensor and $\underline{\boldsymbol{\epsilon}}$ is the strain tensor. The factors $E/(1+\nu)$ and $E\nu/((1-2\nu)(1+\nu))$ are the Lamé parameters, expressed by the Young's modulus $E$ and the Poisson ratio $\nu$ [97]. The Lamé parameters can be expressed in all pairs of elastic moduli for isotropic and homogeneous systems.

In Publication **P2**, an analysis of a strictly coupled architecture of a core-shell system under equatorial loading is performed. This investigation ranges from different core and shell sizes to different stiffnesses and Poisson ratios including auxetic materials ($\nu < 0$). Furthermore, the stress field within a deformed core-shell system is analysed. Therefore, Publication **P2** provides insights into the basic properties of soft core-shell systems and their linear response under external interfacial loading.

Since these elastic moduli are attributed to elastic materials without information about the underlying structure, linear elasticity theory provides only coarse-grained results. For more detailed results a further assumptions of the microscopic structure of the system must be carried out. In the following, this is done for the properties of polymers and polymer networks.

### 1.1.3 Polymers

Polymers are repeating arrangements of macromolecules. The unit cells of such a repeating element are referred as monomers. Within a polymer chain, the monomers are chemically bonded together, usually covalently, in a linear (two bonded neighbours) or in a more complex fashion, such as cross-linkers (more than two bonded neighbours). A monomer can therefore be divided into a bead (macromolecule) and a linking bond. Polymer physics is concerned with the chain properties of a polymer chain. The simplest model for a polymer chain, the freely-joined chain, assumes no (long-range) interaction between the beads and the same bond length $|\mathbf{b}_i| = b$. In Publication **P1** and the Chapters 3.1 and 3.2, the covalent bonds are described by a finite extensible nonlinear elastic (FENE) potential [46,77] with $\tilde{k}_\mathrm{F} = 15\varepsilon/\sigma^2$ as the effective spring constant and $\tilde{R}_0 = 1.5\sigma$ as the maximum bond extension, which here corresponds to the bond length $b$.

The free-joined chain serves as a simple model for flexible homopolymer chains [98, 99] and is a typical representative from the group of ideal chains. In polymer physics, the end-to-end distance $\mathbf{R}$ is an important quantity. For an ideal chain [98, 99], the mean end-to-end distance $\langle \mathbf{R} \rangle$ ($\langle \ldots \rangle$ denotes the canonical average) is zero, since the orientation of the bonds is randomly distributed. However, two other quantities suffice to characterise an ideal chain: the maximum end-to-end distance (contour length) $R_{\max}$ and the mean squared end-to-end distance $\langle \mathbf{R}^2 \rangle$. The first quantity can be calculated by multiplying the number of beads $N$ by the absolute bond length between two beads $b$ to $R_{\max} = \sum_{i=1}^{N} |\mathbf{b}_i| = Nb$. For the mean squared end-to-end distance $\langle \mathbf{R}^2 \rangle$, the orientation of the bonds must be taken into account, leading to the following result,

$$\langle \mathbf{R}^2 \rangle = \sum_{j=1}^{N} \sum_{i=1}^{N} \langle \mathbf{b}_i \cdot \mathbf{b}_j \rangle = \sum_{j=1}^{N} \sum_{i=1}^{N} \delta_{ij} b^2 = Nb^2. \tag{1.9}$$

The second to last step exploits the fact that the averaged scalar product only contributes when the two bonds $\mathbf{b}_i$ and $\mathbf{b}_j$ are equal; in all other cases the scalar product averages out to zero. A typical feature for the group of ideal chains is the proportionality of the mean square end-to-end distance $\langle \mathbf{R}^2 \rangle$ to the number of beads $N$ in (1.9).

When considering a more realistic polymer chain, self-avoidance becomes important [98, 99]. This leads to a different relationship between the mean squared end-to-end distance $\langle \mathbf{R}^2 \rangle$ and the number of beads $N$

$$\langle \mathbf{R}^2 \rangle \sim N^{2\nu} \tag{1.10}$$

with $\nu > 1/2$ (ideal chain: $\nu = 1/2$). The larger exponent $\nu$ reflects the effect that the chain occupies more space because the beads do not penetrate each other, and the polymer therefore swells. A simple approximation [98, 99] for an effective short-range potential (causing also a long-range potential) describing such self-avoidance is given by

$$v_{\text{eff}} \left( \mathbf{r}_n - \mathbf{r}_m \right) \approx k_{\mathrm{B}} T v(T) \delta \left( \mathbf{r}_n - \mathbf{r}_m \right) \tag{1.11}$$

with $k_{\mathrm{B}}$ as Boltzmann constant, $T$ as temperature, $v(T)$ as temperature dependent effective excluded volume and $\delta$ as Dirac delta function. The given part of the interaction potential between the beads described by the Dirac delta function in (1.11) is described in the monomer-resolved simulations in Publication **P1** and the Chapters 3.1 and 3.2 by a repulsive Weeks-Chandler-Andersen [100] potential, where $\sigma$ represents a finite bead length and $\varepsilon$ a repulsive strength.

The temperature-dependent effectively excluded volume $v(T)$ is related to the second virial coefficient [101], which can be shown by the average interaction energy for a homogeneous monomer density of the effective short-range interaction

$$F_{\text{int}} = \frac{1}{2} \rho^2 \int d^3\mathbf{r}_n \int d^3\mathbf{r}_m v_{\text{eff}} \left( \mathbf{r}_n - \mathbf{r}_m \right) = \frac{V}{2} \rho^2 k_{\mathrm{B}} T v(T). \tag{1.12}$$

Where $\rho$ is the homogeneous monomer density and $V$ is the volume. Comparing the average interaction energy and the virial expansion of the canonical free energy [98,99], the relation between the temperature-dependent effectively excluded volume $v(T)$ and the second virial coefficient becomes clear,

$$v(T) = 2B_2(T). \tag{1.13}$$

In addition to the repulsive self-avoidance interaction, the second virial coefficient $B_2(T)$ (and thus the effectively excluded volume $v(T)$) can generally also exhibit attractive interactions. Therefore, in most cases, a temperature condition can be derived for which the second virial coefficient vanishes due to the mutual cancellation of the attractive and repulsive interactions, $B_2(\theta) = 0$. The temperature $\theta$ (at which the mutual cancellation occurs) is referred to in the literature as the Flory or Theta-temperature [98,99,102]. Therefore, a real polymer chain behaves like an ideal chain (up to the second virial order) for the Flory temperature. When attractive interactions prevail in the equilibrium configuration of the polymer chain, the corresponding state is referred as the collapsed state ($\nu < 1/2$). In the opposite case, when repulsive interactions predominate, the corresponding state is called the swollen state ($\nu > 1/2$). A concrete attractive bead-bead interaction potential $V_\alpha$ obtained in the monomer-resolved simulations in Publication **P1** and Chapter 3.1, is presented in the next section on polymer networks (1.1.4).

In Publication **P1**, a polymer adsorbed at an interface is investigated in the transition region between the collapsed state and the swollen state. The study found hysteresis for a collapsed adsorbed polymer in surface pressure, indicating the collapsed state as a special kinetically hindered state for an adsorption process. Furthermore, polymer-grafted cores (hairy particles) in the swollen state are investigated in Chapter 3.2. For one polymer-grafted core (hairy particle), the effective interaction with the interface is analysed and its equilibrium distance to the interface is revealed. For two polymer-grafted cores (hairy particles), the effective pair interaction between the cores induced by the coronae, formed at the interface, is investigated in this equilibrium distance from the interface.

### 1.1.4 Polymer networks

For the description of polymer networks, especially microgels, in aqueous solutions, the Flory-Rehner theory is sufficient [102, 103]. Within the framework of this theory [102, 103], the elastic properties of the polymer network are described coarsely in the context of rubber elasticity and it is assumed that the chemical potentials of the solvent molecules inside and outside the polymer network, $\mu_s^{\text{in}}$ and $\mu_s^{\text{out}}$, must be equal in equilibrium. Therefore, the condition is,

$$\mu_s^{\text{in}} = \mu_s^{\text{out}}. \tag{1.14}$$

The osmotic pressure $\Pi$ provides a convenient way to link the condition (1.14) to the change in Helmholtz free energy $\Delta F$. While (1.14) causes a vanishing osmotic pressure $\Pi$, thermodynamics dictates the relation to the change in Helmholtz free energy $\Delta F$ [102, 103] as,

$$\Pi = -\frac{N_A}{\nu_s}\frac{\partial \Delta F}{\partial N_s} = -\frac{\mu_s^{\text{in}} - \mu_s^{\text{out}}}{\nu_s} = 0, \tag{1.15}$$

where $\nu_s$ is the molar volume of the solvent, $N_A$ as Avogadro's number and $N_s$ as the number of solvent molecules. For neutral networks, the change in Helmholtz free energy $\Delta F$ consists of two energy terms, the mixing energy of the solvent particles and the polymer segments (not necessarily monomers) $\Delta F_{\text{mix}}$ and the elastic energy $\Delta F_{\text{el}}$,

$$\Delta F = \Delta F_{\text{mix}} + \Delta F_{\text{el}}. \tag{1.16}$$

The former is motivated by the Flory-Huggins theory (lattice mixing theory), the latter by the (statistical) theory of rubber elasticity.

The mixing energy $\Delta F_{\text{mix}}$ is defined by [102, 103]

$$\Delta F_{\text{mix}} = N_s k_{\text{B}} T \left[\ln\left(1-\varphi\right) + \chi\varphi\right] \tag{1.17}$$

where $\varphi$ is the volume fraction of the polymer and $\chi$ is the interaction strength between polymer and solvent. The volume fraction $\varphi$ is defined as [102]

$$\varphi = \frac{\xi N_p}{N_s + \xi N_p}, \tag{1.18}$$

where $N_p$ is the number of polymer molecules and $\xi$ is the ratio of the molecular volumes of a polymer molecule and a solvent molecule [103]. The quantity $\nu_s/N_A$ represents the volume of a solvent molecule and in this context also the volume of a lattice site. The logarithmic term in (1.17) describes the entropy change for the volume fraction of the solvent molecules. Further entropic terms (known from the lattice theory of mixing [103]) are neglected here, since the number of polymer segments is infinitesimal small compared to the number of solvent molecules. However, the interaction parameter $\chi$ of the polymer segment and the solvent particle is defined at the microscopic level in terms of lattice theory as,

$$\chi = \frac{\Delta F_{\text{PS}}}{2k_{\text{B}}T}, \tag{1.19}$$

where $\Delta F_{\text{PS}}$ is the free energy difference for a (hypothetical) lattice site exchange between a solvent particle and a polymer segment.

The elastic energy $\Delta F_{\mathrm{el}}$ is defined by the entropy change $\Delta S_{\mathrm{el}}$, known from the statistical theory of (isotropic) rubber elasticity [102, 103], as,

$$\Delta F_{\mathrm{el}} = -T\Delta S_{\mathrm{el}} = -\frac{3N_c k_{\mathrm{B}} T}{2}\left[\ln(\alpha) - \alpha^2 + 1\right], \tag{1.20}$$

where $N_c$ is the number of chains in the network and $\alpha$ is the (linear) swelling ratio [102, 103]. $\alpha$ is defined by the fraction of the volume $V$ and the reference volume $V_0$ as follows,

$$\alpha = \left(\frac{V}{V_0}\right)^{\frac{1}{3}} = \left(\frac{\varphi_0}{\varphi}\right)^{\frac{1}{3}}, \tag{1.21}$$

where $\varphi_0$ is the reference volume fraction. The reference volume $V_0$ and the reference volume fraction $\varphi_0$ are related by the fact that $V_0\varphi_0$ represents the (occupied) volume of the whole polymer network. Therefore, the term $V_0\varphi_0/(\nu_s/N_a)$ can be interpreted as the lattice sites occupied by the entire polymer network, which is equivalent to $\xi N_p$. However, the definition of the reference volume $V_0$ is a non-trivial venture and still subject to current research [103].

Considering the two parts of the change in the Helmholtz free energy $\Delta F$ and using the relations (1.15) and (1.14), the equation of state (EOS) is given by,

$$\begin{aligned}\frac{N_c\nu_s}{V_0 N_{\mathrm{A}}}\left[\frac{\varphi}{2\varphi_0} - \left(\frac{\varphi}{\varphi_0}\right)^{\frac{1}{3}}\right] &= \varphi + \ln(1-\varphi) + \chi\varphi^2 \\ &= \underbrace{\left(\chi - \frac{1}{2}\right)}_{B_2}\varphi^2 + \mathcal{O}\left(\varphi^3\right).\end{aligned} \tag{1.22}$$

Here the series expansion of the volume fraction $\varphi$ originates from a virial expansion of the osmotic pressure (which provides the form of $B_2$) with an additive term proportional to $\varphi^{\frac{1}{3}}$. However, the parameter $\chi$ (significantly) affects the second virial coefficient $B_2$ of the EOS (1.22). Therefore, the value $\chi = 1/2$ takes on a very similar role as the Flory temperature $\theta$ in polymer physics, since for this value the second virial coefficient $B_2$ disappears. For values smaller than 1/2, the network system is in a state of good solvent conditions (swollen state), indicated by a small volume fraction $\varphi$ as the solution of the EOS and in agreement with the Flory-Huggins theory for good mixing conditions. For values greater than 1/2, the network faces poor solvent conditions (collapsed state) and the solvent particles and polymer segments segregate. This effect is reflected in a larger volume fraction $\varphi$ as solution.

For PNiPAm networks, the following rough calculation can be performed [103]. Since $\chi$ depends roughly on the free energy difference $\Delta F_{\mathrm{PS}}$ for a (hypothetical) lattice site change in (1.19), a calculation of the entropy $\Delta S_{\mathrm{PS}}$ and the enthalpy $\Delta H_{\mathrm{PS}}$

is sufficient for PNiPAm polymers in aqueous solutions. When a hydrophobic molecular segment, such as a PNiPAm polymer segment, enters an aqueous solution, the water molecules are forced to rearrange their hydrogen bonds and form a clathrate. This formation acts like a cage for the hydrophobic segment [103]. Since order is established in this process, the entropy change $\Delta S_{\mathrm{PS}}$ is assumed (roughly) to be negative. This assumption is supported by the fact that a clathrate is also an ice-like structure, therefore the process of transferring a polymer segment into an aqueous solution generates latent freezing heat, which means that the enthalpy change $\Delta H_{\mathrm{PS}}$ is negative (and so is the entropy change $\Delta S_{\mathrm{PS}}$). Therefore, the free energy of a (hypothetical) lattice side change $\Delta F_{\mathrm{PS}} = \Delta H_{\mathrm{PS}} - T\Delta S_{\mathrm{PS}}$ increases with temperature $T$. Due to this microscopic behaviour of $\Delta F_{\mathrm{PS}}$, the solvent conditions are good for low temperatures $T$ ($\chi < 1/2$, swollen state/small volume fraction $\varphi$) and poor for high temperatures $T$ ($\chi > 1/2$, collapsed state/large volume fraction $\varphi$).

In the monomer-resolved simulations in Publication **P1** and Chapter 3.1, the different solvent conditions are accounted by an attractive bead-bead interaction $V_\alpha$ (in addition to the repulsive bead-bead interactions). The interaction potential $V_\alpha$ is defined as,

$$V_\alpha(r) = \begin{cases} -\alpha\varepsilon & \text{if} \quad r \leq 2^{\frac{1}{6}}\sigma \\ \frac{1}{2}\alpha\varepsilon\left[\cos\left(\gamma\left(\frac{r}{\sigma}\right)^2 + \beta\right) - 1\right] & \text{if} \quad 2^{\frac{1}{6}}\sigma < r \leq R_0\sigma \\ 0 & \text{otherwise} \end{cases} \tag{1.23}$$

where $\gamma = \pi\left(2.25 - 2^{\frac{1}{3}}\right)^{-1}$ and $\beta = 2\pi - 2.25\gamma$ [104]. $r$ is the distance between the beads and $\alpha$ is a dimensionless parameter that controls the effective strength of attraction. Since the bead-bead interaction significantly affects the configurations of the system, an attractive bead-bead interaction can effectively be mapped to an attractive solvent-solvent interaction, although the solvent is only implicitly considered. The value $\alpha = 0$ corresponds to no attraction between the beads, so in this case only the repulsive bead-bead interaction is crucial and the network is in the swollen state. Since this is the same behaviour found for a low temperature (regime), the effective attraction strength $\alpha$ can be interpreted as an effective temperature. For values $\alpha \geq 1$, the attractive interaction is strong (relative to the repulsive interaction) and thus decisive for the bead-bead interaction and the network is in the collapsed state. Again, the same behaviour is found between the effective attractive strength $\alpha$ and the respective temperature regime [46]. The volume phase transition at $\chi = 1/2$ (and in the experiments for 32°C) results for this attractive interaction potential associated with the repulsive interactions by the value $\alpha \sim 0.6$ for the effective attractive strength [44, 46].

In Publication **P1**, the mixing conditions associated with the different values of $\chi$ (good ($\alpha = 0$) and poor ($\alpha \geq 1$) solvent conditions) are investigated. The swelling isotropy is broken by the fluid interface. However, kinetic effects become visible, e.g. a hysteresis between a microgel (polymer network) adsorbed under poor solvent conditions and a microgel (polymer network) adsorbed under good conditions, followed by a collapse (poor conditions) at the interface. This effect is investigated using lateral expansion and surface pressure from the simulational and experimental side.

In Chapter 3.1 an interfacial system with two interfaces in a slit-like configuration is investigated. A dense and a (more) diluted packed situation are represented there by one and two microgels positioned and adsorbed, respectively, in an interfacial Wigner-Seitz cell within the interfacial configuration. Both are in the same (swollen or collapsed) state. With sufficiently small distances between the two interfaces, an effective negative or positive osmotic pressure arise between the interfaces in the various cases. A particular situation in which a negative effective osmotic pressure is induced is the case of a diluted system in the collapsed state. In all other situations, the effective osmotic pressure is positive.

## 1.2 Theoretical description

In this section, the theoretical methods used for the problems treated are briefly discussed. On the simulation side, the Langevin equations [105, 106] are integrated and the limit of Brownian dynamics [106, 107] is derived, which is used (to solve the equations of motion) in Publication **P1** and the Chapters 3.1 and 3.2. The (purely) theoretical side is served by the introduction of linear elasticity theory and the derivation of the Navier-Cauchy equations [108], which are solved under the boundary conditions in (1.7) in Publication **P2**.

### 1.2.1 Brownian Dynamics

In (pure) molecular dynamics simulations, Newton's equations of motion are solved numerically for systems with a very large number of particles. This approach is based on statistical mechanics and classical physics and is sufficient for a coarse grain set-up, since for example a polymer consists of thousands of molecules. Thus, by knowing the initial positions and initial momentum, the system is numerically solved by calculating the given interactions. In a system with slowly evolving ("countable") heavyweight particles and rapidly evolving ("uncountable") lightweight particles, an coarsening of Newton's to Langevin's equations of motion is appropriate. The Langevin equations contain an additional random force term $\mathbf{F}_i^R$ that describes the interaction between the lightweight particles and the heavyweight particles in a coarse-grained (stochastic) way. The Langevin equations are defined as

$$m_i \frac{d}{dt} \mathbf{v}_i = \mathbf{F}_i - m_i \beta \mathbf{v}_i + \mathbf{F}_i^R \tag{1.24}$$

where $m_i$ denotes the mass of particle $i$, $\mathbf{v}_i$ denotes the velocity, $\mathbf{F}_i$ denotes an external force and $m_i\beta\mathbf{v}_i$ denotes a drag force. A physical example of the random force $\mathbf{F}_i^R$ are solvent particles (lightweight particles) exerting impacts and collisions on polymers or colloids (heavyweight particles), which are not explicitly calculated. For heavyweight particles in a bath of lightweight particles the distribution of the random force $\mathbf{F}_i^R$ approaches a Gaussian distribution, due to the sum of many collisions on the heavyweight particles (central limit theorem), and is thus uniquely defined by the first two cumulatives (mean $\left\langle \mathbf{F}_i^R(t)\right\rangle$ and variance $\left\langle \mathbf{F}_i^R(t)\cdot\mathbf{F}_i^R(t')\right\rangle$). However, these cumulatives are given by [106],

$$\left\langle \mathbf{F}_i^R(t)\right\rangle = \mathbf{0}, \tag{1.25}$$

$$\left\langle \mathbf{F}_i^R(t)\cdot\mathbf{F}_i^R(t')\right\rangle = 6k_\mathrm{B}Tm_i\beta\delta\left(t-t'\right), \tag{1.26}$$

where $\langle\ldots\rangle$ denotes the canonical average.

Since the Langevin equations (1.24) are linear first order ordinary differential equations in velocity $\mathbf{v}_i$, the integrating method implies the use of an integrating factor. According to Ref. [106], this integrating factor is used as $\exp\left(\beta\int d\tilde{t}\right)$ and integration is performed from $t_0$ to $t_0+t$. Further integration provides the equation for the position $\mathbf{r}_i$ of the particle $i$. The equations for the velocity $\mathbf{v}_i$ and the position $\mathbf{r}_i$ of the particle $i$ can then be written as follows [106],

$$\begin{aligned}\mathbf{v}_i\left(t_0+t\right)-\mathbf{v}_i\left(t_0\right)\exp\left(-\beta t\right)=&\frac{1}{m_i}\int_0^t \exp\left(-\beta\left(t-s\right)\right)\mathbf{F}_i\left(s+t_0\right)ds\\&+\frac{1}{m_i}\int_0^t \exp\left(-\beta\left(t-s\right)\right)\mathbf{F}_i^R\left(s+t_0\right)ds,\end{aligned} \tag{1.27}$$

$$\begin{aligned}\mathbf{r}_i\left(t_0+t\right)-\mathbf{r}_i\left(t_0\right)=&\mathbf{v}\left(t_0\right)\frac{1-\exp\left(-\beta t\right)}{\beta}\\&+\frac{1}{m_i}\int_0^t ds\int_0^s ds'\exp\left(-\beta\left(s-s'\right)\right)\mathbf{F}_i\left(s'+t_0\right)\\&+\frac{1}{m_i}\int_0^t ds\int_0^s ds'\exp\left(-\beta\left(s-s'\right)\right)\mathbf{F}_i^R\left(s'+t_0\right).\end{aligned} \tag{1.28}$$

From the equations (1.27) and (1.28), two limits can be derived, the underdamped limit and the overdamped limit. The equations simplify in the underdamped limit ($\beta\to 0$) to the velocity Verlet algorithm [109]. In this case, Newton's equations of motion (for the heavyweight particles) can be recognised again and the effects of the lightweight particles thus cancel out.

In the overdamped limit case, the dynamic equations become the equations of Brownian motion. In this case ($\beta^{-1}\to 0$), two random variables $\mathbf{A}_{i,1}(t)$ and $\mathbf{A}_{i,2}(t)$ (resulting from the integration of the random force $\mathbf{F}_i^R(t)$) appear in the calculation of the velocity and position of the particle $i$ [106],

$$\mathbf{v}_i\left(t_0+t\right) = \mathbf{A}_{i,1}\left(t\right) \tag{1.29}$$

$$\mathbf{r}_i\left(t_0+t\right) = \mathbf{r}_i\left(t_0\right) + \frac{1}{m_i\beta}\mathbf{F}_i t + \mathbf{A}_{i,2}\left(t\right). \tag{1.30}$$

The Gaussian distributions of $\mathbf{A}_{i,1}(t)$ and $\mathbf{A}_{i,2}(t)$ satisfy the following relations [106],

$$\langle\mathbf{A}_{i,1}\rangle = \langle\mathbf{A}_{i,2}\rangle = 0, \tag{1.31}$$

$$\langle|\mathbf{A}_{i,1}|^2\rangle = \frac{3k_\mathrm{B}T}{m_i}, \tag{1.32}$$

$$\langle|\mathbf{A}_{i,2}|^2\rangle = \frac{6k_\mathrm{B}T}{m_i\beta}t, \tag{1.33}$$

$$\langle\mathbf{A}_{i,1}\cdot\mathbf{A}_{i,2}\rangle = 0. \tag{1.34}$$

Therefore, the velocity $\mathbf{v}_i$ is calculated by a pure stochastic approach and the position $\mathbf{r}_i$ by a mixture of stochastic and deterministic forces.

Since the set-up in Publication **P1** and the Chapters 3.1 and 3.2 requires a bath of (lightweight) solvent particles in which the polymer beads of the linear polymers and microgels dissolve, the equations of motion of the polymer beads are simulated by Brownian dynamics to implicitly preserve the influence of the solvent particles. The simulations are carried out with the HOOMD Blue package [110], version 2.9.0, in combination with several Python packages.

### 1.2.2 Linear elasticity

For the purpose of describing the small (linear) deformation of an elastic material, the continuum theory of linear elasticity is introduced. Therefore, an overview of the basics of linear elasticity theory is given here, based on Ref. [97]. Second-rank tensors and matrices are marked by an underscore.

Within the theory of elasticity two states are compared, the undeformed state (thermodynamic ground state) $\mathbf{r}$ and the deformed state $\mathbf{r}'$. The two states are compared by the difference of the two states $\mathbf{u}$ (linear theory),

$$\mathbf{u} = \mathbf{r}' - \mathbf{r}. \tag{1.35}$$

Moreover, the deformation $\mathbf{u} := \mathbf{u}\left(\mathbf{r}\right)$ can be understood as a deformation field describing the deformation at each point of the undeformed state $\mathbf{r}$ of the elastic material. For the distances between two infinitesimally close points $\mathrm{d}\mathbf{r}$ and $\mathrm{d}\mathbf{r}'$, (1.35) gives the following differential,

$$\mathrm{d}\mathbf{r}' = \mathrm{d}\mathbf{r} + \mathrm{d}\mathbf{u}. \tag{1.36}$$

Using the relation (1.36), the square of the differential line element $\mathrm{d}\mathbf{r}'^2$ can be calculated as,

$$\begin{aligned} \mathrm{d}\mathbf{r}'^2 =& \mathrm{d}\mathbf{r}' \cdot \mathrm{d}\mathbf{r}' = (\mathrm{d}\mathbf{r} \cdot \mathrm{d}\mathbf{r} + \mathrm{d}\mathbf{r} \cdot \mathrm{d}\mathbf{u} + \mathrm{d}\mathbf{r} \cdot \mathrm{d}\mathbf{u} + \mathrm{d}\mathbf{u} \cdot \mathrm{d}\mathbf{u}) \\ \overset{\mathrm{d}\mathbf{u}=(\nabla\mathbf{u})\cdot\mathrm{d}\mathbf{r}}{=}& (\underline{\mathbf{I}} + 2\underline{\boldsymbol{\epsilon}}) : \mathrm{d}\mathbf{r}\mathrm{d}\mathbf{r}, \end{aligned} \tag{1.37}$$

where the chain rule is applied in the last step, ":" is the Frobenius inner product, $\underline{\mathbf{I}}$ is the unit matrix and $\underline{\boldsymbol{\epsilon}}$ is defined as the strain tensor in (1.37) with,

$$\underline{\boldsymbol{\epsilon}} = \frac{1}{2}\left[\nabla\mathbf{u} + (\nabla\mathbf{u})^{\mathrm{T}}\right] + \mathcal{O}\left((\nabla\mathbf{u})^2\right). \tag{1.38}$$

Due to the symmetry of this tensor, there are six independent real components in three spatial dimensions. Furthermore, this tensor does not change for two types of deformations, namely uniform translations and rotations. A Uniform translation is excluded due to the deviatoric nature of the strain tensor and a rotation due to its symmetry.

The volume change in three dimensions is described by

$$\mathrm{d}^3 r' = \det\left(\frac{\partial\mathbf{r}'}{\partial\mathbf{r}}\right)\mathrm{d}^3 r \overset{(1.35)}{=} \det\left(\underline{\mathbf{I}} + \nabla\mathbf{u}\right)\mathrm{d}^3 r. \tag{1.39}$$

The determinant can be written as [111]

$$\det\left(\underline{\mathbf{I}} + \nabla\mathbf{u}\right) = 1 + \mathrm{Tr}\left(\nabla\mathbf{u}\right) + \mathcal{O}\left((\nabla\mathbf{u})^2\right) \tag{1.40}$$

This expression already shows that a volume change for $\mathrm{Tr}\left(\nabla\mathbf{u}\right) = \mathrm{Tr}\left(\underline{\boldsymbol{\epsilon}}\right) = \nabla\cdot\mathbf{u} \neq 0$ occurs. A conserved volume thus satisfies the condition $\nabla \cdot \mathbf{u} = 0$. Using the definition of Poisson ratio $\nu$, for an arbitrary coordinate system where the $x$-axis is the direction of tension [97],

$$\nu = -\frac{\epsilon_{yy}}{\epsilon_{xx}} = -\frac{\epsilon_{zz}}{\epsilon_{xx}}, \tag{1.41}$$

where $\epsilon_{xx}, \epsilon_{yy}, \epsilon_{zz}$ are the diagonal entries of $\underline{\boldsymbol{\epsilon}}$, (1.39) can be simplified and transformed to

$$\frac{\mathrm{d}^3 r'}{\mathrm{d}^3 r} = 1 + \varepsilon_{xx}\left(1 - 2\nu\right) + \mathcal{O}\left((\nabla\mathbf{u})^2\right). \tag{1.42}$$

From (1.42) and (1.40), certain volume properties can be derived for values of $\nu$. For $\nu = 1/2$ the volume change is independent of the strain tensor $\underline{\boldsymbol{\epsilon}}$ and the volume is conserved despite deformation, the material is incompressible. Furthermore, for $\nu = 0$ there is a volume change determined only by $\epsilon_{xx}$, so the length changes only in the tensile direction. For $\nu = -1$ there is the same deformation in three dimensions in all spatial directions as for the deformation in the tensile direction.

For any coarse-grained volume $V$ within the deformed material (in static equilibrium), external forces can act in the bulk or on the surface $\partial V$. According to Newton's third law, external forces in the volume $V$ and at its surface $\partial V$ cause counterforces in static equilibrium, therefore conservation of momentum is assumed,

$$\int_{\partial V} \mathrm{d}S \underline{\boldsymbol{\sigma}} \cdot \mathbf{n} + \int_V \mathrm{d}V \mathbf{f}_{\mathrm{bulk}} = \int_V \mathrm{d}V \left(\nabla \cdot \underline{\boldsymbol{\sigma}} + \mathbf{f}_{\mathrm{bulk}}\right) = 0 \tag{1.43}$$

Here $\underline{\boldsymbol{\sigma}}$ denotes the (symmetric) stress tensor (acting on the surface) and $\mathbf{f}_{\mathrm{bulk}}$ denotes a force, such as gravity, acting on the bulk of the material within the volume $V$. The angular momentum is also conserved in static equilibrium, therefore the relation $\underline{\boldsymbol{\sigma}} = \underline{\boldsymbol{\sigma}}^{\mathrm{T}}$ [97] holds. Equation (1.43) implies that the difference between the undeformed $V$ and the deformed volume $V'$ is small ($V \approx V'$), which is why this theory is limited to small deformations.

In order to incorporate the elasticity theory into the thermodynamic context, an elastic work $\delta W$ must be defined (the differential of the elastic work is denoted here by $\delta$ so that this is not confused with a integration variable). The elastic work density $\delta w$ is defined by the (inner) product of the local external force density $\nabla \cdot \underline{\boldsymbol{\sigma}}$ and the differential of the deformation $\delta \mathbf{u}$. By integration over the (full) volume $V$, the work $\delta W$ is then defined as,

$$\begin{aligned} \delta W = \int_V \mathrm{d}V \delta w = \int_V \mathrm{d}V \left(\nabla \cdot \underline{\boldsymbol{\sigma}}\right) \cdot \delta \mathbf{u} &= \underbrace{\oint_{\partial V} \mathrm{d}S \left(\mathbf{n} \cdot \underline{\boldsymbol{\sigma}}\right) \cdot \delta \mathbf{u}}_{=0} - \int_V \mathrm{d}V \underline{\boldsymbol{\sigma}} : \nabla \delta \mathbf{u} \\ &= - \int_V \mathrm{d}V \underline{\boldsymbol{\sigma}} : \delta \underline{\boldsymbol{\epsilon}}, \end{aligned} \tag{1.44}$$

where the second to last step exploits the fact that the term $(\mathbf{n} \cdot \underline{\boldsymbol{\sigma}})$ is zero or orthogonal to $\delta \mathbf{u}$ on the surface of the volume. The last step utilises the fact that the derivatives can be interchanged $\nabla \delta \mathbf{u} = \delta \left(\nabla \mathbf{u}\right)$ and that the Frobenius inner product with the symmetric tensor $\underline{\boldsymbol{\sigma}}$ eliminates the antisymmetric component of the tensor $\nabla \mathbf{u}$. The term for the elastic work density is then given as

$$\delta w = -\underline{\boldsymbol{\sigma}} : \delta \underline{\boldsymbol{\epsilon}}. \tag{1.45}$$

The density of the Helmholtz free energy $f = F/V$ is given by

$$\mathrm{d}f = -s \mathrm{d}T + \underline{\boldsymbol{\sigma}} : \mathrm{d}\underline{\boldsymbol{\epsilon}}, \tag{1.46}$$

with $s = S/V$ as the entropy density. The thermodynamic relation for the stress tensor at constant temperature $T$ is therefore given by

$$\underline{\boldsymbol{\sigma}} = \left(\frac{\partial f}{\partial \underline{\boldsymbol{\epsilon}}}\right)_T. \tag{1.47}$$

Hooke's law [97] assumes that the density of the Helmholtz free energy $f$ is quadratic in the strain tensor, which is given for isotropic and homogeneous materials as,

$$f = \frac{1}{2}\lambda \mathrm{Tr}\left[\underline{\boldsymbol{\epsilon}}\right]^2 + \mu \underline{\boldsymbol{\epsilon}} : \underline{\boldsymbol{\epsilon}}, \tag{1.48}$$

with the two Lamé parameters $\lambda$ and $\mu$ [97]. The latter also represents the shear modulus. Furthermore, for the stress tensor and the consideration of (1.47) the following relation is obtained

$$\underline{\boldsymbol{\sigma}} = \lambda \underline{\mathbf{I}} \mathrm{Tr}\left[\underline{\boldsymbol{\epsilon}}\right] + 2\mu \underline{\boldsymbol{\epsilon}}. \tag{1.49}$$

This relation is also given as a constitutive equation (1.8) in the section on soft materials (1.1.2), with $\lambda = E\nu/((1-2\nu)(1+\nu))$ and $\mu = E/(2(1+\nu))$.

By performing the divergence of (1.49) and neglecting any external force $\mathbf{f}_{\text{bulk}} = \mathbf{0}$ on the bulk in (1.43), the homogeneous Navier-Cauchy equations in static equilibrium can be derived. Explicitly, the equations are given as

$$\begin{aligned} \nabla \cdot \underline{\boldsymbol{\sigma}} &\overset{(1.49),(1.38)}{=} \mu \nabla^2 \mathbf{u}(\mathbf{r}) + (\lambda + \mu)\nabla(\nabla \cdot \mathbf{u}(\mathbf{r})) \overset{(1.43)}{=} \mathbf{0} \\ &\Leftrightarrow (1-2\nu)\nabla^2 \mathbf{u}(\mathbf{r}) + \nabla(\nabla \cdot \mathbf{u}(\mathbf{r})) = \mathbf{0}. \end{aligned} \tag{1.50}$$

While in the last step the Lamé parameters $\lambda$ and $\mu$ are expressed as a function of the Young modulus $E$ and the Poisson ratio $\nu$. Due to the homogeneity of the equations, the dependence of the elastic modulus cancels out and they are transformed into the form (1.50) used in Publication **P2**. The homogeneous Navier-Cauchy equations thus describe the displacement field $\mathbf{u}$ of an isotropic and homogeneous medium under equilibrium conditions, with constant Lamé parameters and no external force $\mathbf{f}_{\text{bulk}}$ acting on the bulk.

In Publication **P2**, the homogeneous Navier-Cauchy equations (1.50) are solved considering the boundary conditions in (1.7) to study the deformation of a core-shell system in an interfacial confinement.

## 1.3 Experimental approach

In this section an overview of the basics of the experiments is given, based on Ref. [70]. In the experimental set-up, the PNiPAm microgels are crosslinked with N,N'-methylenebis(acrylamide). The crosslinking density is varied between 1% and 5%, see Publication **P1**, and the synthesis is carried out by precipitation polymerisation according to literature protocols [8]. Furthermore, a Langmuir-Blodgett trough (KSV NIMA) is used, made from Teflon with a trough area of $243\,\mathrm{cm}^2$ and controllable barriers made of polyoxymethylene. A Wilhelmy plate measures the surface pressure, which is set to zero at 20°C, and a silicon substrate

(LG Silicon Inc.) mounted at a 45° angle emphorises the microgels through the air-water interface. However, the temperature of the water phase (within the trough) is controlled by a water circuit fed by a thermostat (VWR) and measured by an included thermometer. For a detailed set-up, see figure 1.2.

The microgel dispersion, diluted to 0.05 %, is mixed with ethanol in a 1:1 ratio. The ethanol is used as a spreading agent. The respective initial volume state of the microgels is achieved by a water temperature of 70°C (60°C preheated) for the collapsed and 22°C for the swollen state. These initial states are equilibrated at the interface for 20 minutes. The heating and cooling of the water phase occurs in different ways: In the heating process, the temperature is increased by 10°C every 10 minutes (linear increase), while in the cooling process the thermostat is turned off and the temperature decreases to room temperature (exponential decrease). However, during the heating or cooling process, the dipper is raised at a speed of 0.1 mm/min so that the silicon wafer moves through the interface. This protocol ensures that for all temperatures the lateral expansion of the microgels at the interface is maintained and the respective surface pressure can be assigned.

The morphology of the microgels is then analysed ex situ using scanning electron microscopy (SEM, Zeiss Gemini 500) and atomic force microscopy (AFM, JPK Nano Wizard, cantilever: Anfatec NSC 18). The SEM images are acquired by scanning along the substrate with a finite step of 1mm using a 30$\mu$m aperture, a current of 1kV and the in-lens detector. The AFM images taken in AC mode have a resolution of 514 x 514 pixels [8]. For the images of the SEM the analysis is done in detail with a specially developed image analysis software [70]. The AFM images are studied with the program Gwyddion.

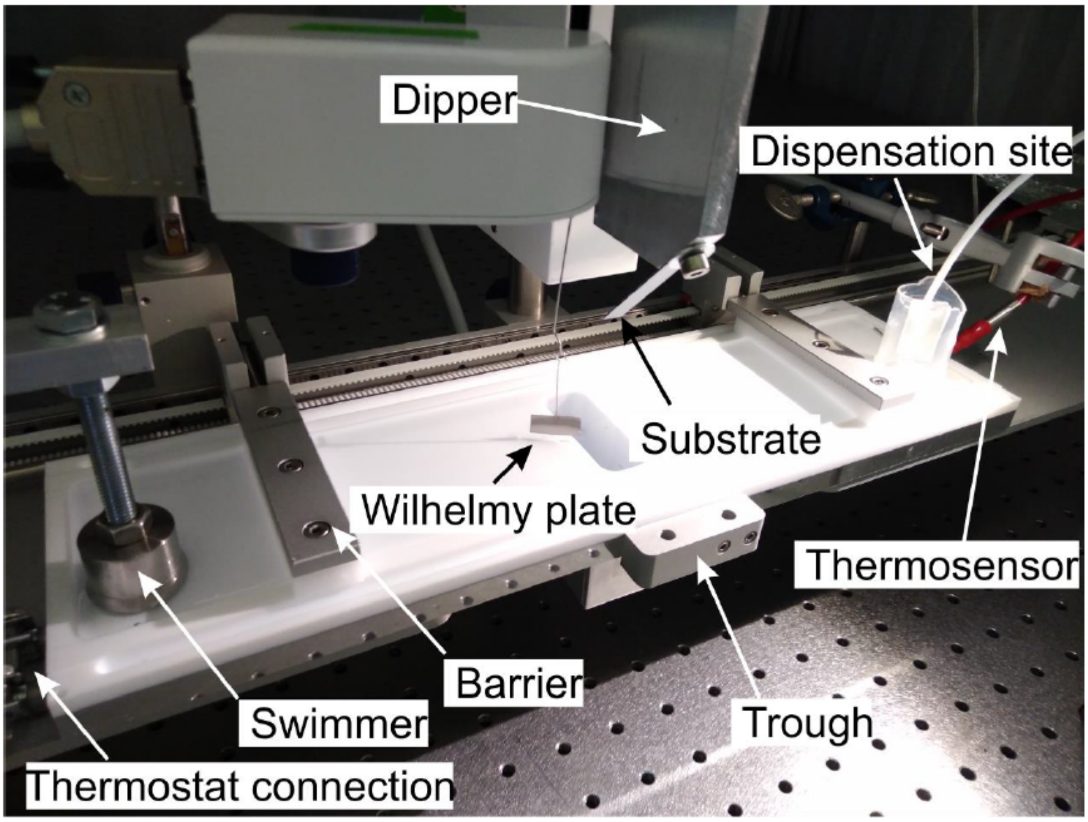

Figure 1.2: Langmuir-Blodgett trough set-up, where the corresponding components are labelled. Reprinted (adapted) with permission from [70]. Copyright 2019 American Chemical Society.

# Chapter 2

# Scientific Publications

In the following, Publications **P1**–**P2** that form the basis of this dissertation are reproduced. For each publication, I present a summary of my contributions and a notice on copyright and licensing.

# P1 Interface-induced hysteretic volume phase transition of microgels: simulation and experiment

Reproduced from

J. Kolker, J. Harrer, S. Ciarella, M. Rey, M. Ickler, L. M. C. Janssen, N. Vogel and H. Löwen,
*Interface-induced hysteretic volume phase transition of microgels: simulation and experiment,*
Soft Matter, 2021, **17**, 5581-5589,

Digital Object Identifier (DOI): `https://doi.org/10.1039/D1SM00111F`

### Statement of contribution

SC and me developed the numerical code and I performed the numerical evaluations. JH, MR and MI performed the experiments. All authors discussed the results and edited the manuscript.

### Copyright and license notice

Soft Matter

ROYAL SOCIETY OF CHEMISTRY

PAPER

View Article Online
View Journal | View Issue

Check for updates

Cite this: *Soft Matter*, 2021, 17, 5581

# Interface-induced hysteretic volume phase transition of microgels: simulation and experiment†

Jannis Kolker, *[a] Johannes Harrer, *[b] Simone Ciarella, [c] Marcel Rey, [b] Maret Ickler,[b] Liesbeth M. C. Janssen,[c] Nicolas Vogel [b] and Hartmut Löwen [a]

Thermo-responsive microgel particles can exhibit a drastic volume shrinkage upon increasing the solvent temperature. Recently we found that the spreading of poly(*N*-isopropylacrylamide) (PNiPAm) microgels at a liquid interface under the influence of surface tension hinders the temperature-induced volume phase transition. In addition, we observed a hysteresis behavior upon temperature cycling, *i.e.* a different evolution in microgel size and shape depending on whether the microgel was initially adsorbed to the interface in expanded or collapsed state. Here, we model the volume phase transition of such microgels at an air/water interface by monomer-resolved Brownian dynamics simulations and compare the observed behavior with experiments. We reproduce the experimentally observed hysteresis in the microgel dimensions upon temperature variation. Our simulations did not observe any hysteresis for microgels dispersed in the bulk liquid, suggesting that it results from the distinct interfacial morphology of the microgel adsorbed at the liquid interface. An initially collapsed microgel brought to the interface and subjected to subsequent swelling and collapsing (resp. cooling and heating) will end up in a larger size than it had in the original collapsed state. Further temperature cycling, however, only shows a much reduced hysteresis, in agreement with our experimental observations. We attribute the hysteretic behavior to a kinetically trapped initial collapsed configuration, which relaxes upon expanding in the swollen state. We find a similar behavior for linear PNiPAm chains adsorbed to an interface. Our combined experimental – simulation investigation provides new insights into the volume phase transition of PNiPAm materials adsorbed to liquid interfaces.

Received 21st January 2021,
Accepted 3rd May 2021

DOI: 10.1039/d1sm00111f

rsc.li/soft-matter-journal

## 1 Introduction

Soft microgels consisting of a swollen polymer network possess fascinating properties. Their soft nature allows them to undergo significant deformations, for example when adsorbed to an interface.[1,2] In addition, stimuli-responsive properties can be encoded in their molecular structure, allowing microgels to undergo sharp transitions between swollen and collapsed states upon an external stimulus.[3–5] This dynamic behavior has important consequences. From an applied side, stimuli-responsive microgels serve as dynamic and reversible emulsion stabilizers[6–10] or vehicles for drug-delivery, due to their ability to take up and release molecules on demand.[4,11] From a fundamental side, soft microgels serve as model systems for classical many-body systems to model atomistic physical phenomena such as melting of crystal lattices,[12,13] solid–solid phase transitions,[14] or complex self-assembly.[15–17]

Among the most prominent microgel systems are cross-linked poly(*N*-isopropylacrylamide) (PNiPAm)-based microgels, which exhibit a drastic volume shrinkage in aqueous dispersion above 32 °C.[18–20] During this volume phase transition, non-polar groups of the PNiPAm microgel aggregate and bound water is expelled from the macromolecule to increase the entropy of the system.[3,19,20] This volume phase transition has been extensively explored through experimental studies,[5,20–22] computer simulations[5,23–35] and statistical theory.[36–44]

However, in many actual applications such as emulsion stabilization[6–8] or surface patterning[15,45,46] microgel particles are exposed and attracted to a liquid interface, where the spatial isotropy of the microgel is broken and a more complex behavior results. Therefore it is important to understand their

---

[a] *Institut für Theoretische Physik II, Heinrich-Heine-Universität Düsseldorf, Universitätsstrasse 1, D-40225 Düsseldorf, Germany. E-mail: kolker@thphy.uni-duesseldorf.de*

[b] *Institute of Particle Technology, Friedrich-Alexander University Erlangen-Nürnberg, Cauerstrasse 4, 91058 Erlangen, Germany. E-mail: johannes.harrer@fau.de*

[c] *Soft Matter and Biological Physics, Department of Applied Physics, Eindhoven University of Technology, P. O. Box 513, 5600MB Eindhoven, The Netherlands*

† Electronic supplementary information (ESI) available. See DOI: 10.1039/d1sm00111f

structural and dynamical properties when confined to a liquid interface. In fact, it was shown that at liquid interfaces, microgels deform into a fried-egg-like structure[1,2,47–49] where the core possesses a disk-like shape and the surrounding dangling polymer chains form a quasi two-dimensional layer close to the interface, termed the corona. Correspondingly, the volume phase transition is strongly modified due to the presence of the interface. Recent experiments[50–52] have analyzed the volume phase transition at the interface and showed that the volume phase transition in the lateral direction is strongly hindered by the presence of the liquid interface. In addition, a hysteresis behaviour upon swelling and deswelling of microgels dependent on whether the microgels were deposited in the swollen or collapsed state was found.[50,53] Though monomer-resolved computer simulations have considered the microgel structure at an interface,[50,54,55] the hysteretic behaviour was not yet reproduced in computer simulations.

Here we present extensive Brownian dynamics simulations to confirm and investigate the hysteresis on a monomer-resolved scale. The microgel particle is modelled by a coarse-grained polymer network with effective beads.[23,24] The interface is described by an external effective potential attractive for the beads. Within our simulations we are able to reproduce and quantify the hysteresis behavior and the corresponding structural change of the microgel particle. In our protocol the microgel particle is first equilibrated in the bulk either in the collapsed (high temperature) or in the swollen (low temperature) state and then brought to the interface and "equilibrated" there again. Fig. 1 schematically outlines the temperature cycling experiments used for this investigation. A swollen particle adsorbed to the interface responds reversibly to further collapsing and swelling (resp. heating and cooling) cycles. An initially collapsed particle adsorbed to the interface, however, experiences structural changes upon temperature cycling. Instead of reversible regaining its initial size, the microgel remains significantly more expanded after undergoing a temperature cycle. We attribute this hysteretic behaviour to an initial kinetically trapped collapsed state. This behavior is purely induced by the interface, as a similar temperature cycling of a bulk microgel does not show any hysteresis. We investigate these interfacial volume phase transitions as a function of crosslinker density. In both experiments and simulations, we find that less crosslinked microgels exhibit a larger hysteresis. In addition, we show that even linear PNiPAm chains adsorbed to an interface undergo a hysteretic behavior upon temperature cycling, indicating that the hysteresis does not only depend on the architecture of the microgel, but originates from the molecular nature of the polymer itself.

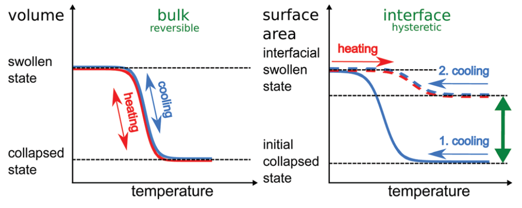

Fig. 1 Schematic visualization of the interface-induced hysteresis effect (right) compared to the bulk behavior (left). Bulk: reversibility between the swollen and collapsed state within a cooling–heating cycle for a microgel particle. Interface: hysteresis in the first cooling–heating cycle of an interface-adsorbed microgel particle. For subsequent cycles reversibility occurs.

## 2 Materials and methods

We adopt the modelling proposed in ref. 25 and 55–57 describing a microgel particle on a monomer-resolved level with no explicit solvent. In detail, the microgel particle consists of two types of beads, monomers and crosslinkers, which define its internal architecture. A monomer is covalently linked to either a neighbouring other monomer or to a crosslinker by springs and the maximum number of these bonds is two. A crosslinking bead, on the other hand, has four of such bonds. In terms of all other interactions (next nearest neighbour interactions, *etc.*) monomers and crosslinkers do not differ. The covalent bonds are described by a finite-extensible-nonlinear-elastic (FENE) potential[25,55] (see ESI†) with a characteristic energy scale $\varepsilon$, a maximal bond expansion $\tilde{R}_0 = 1.5\sigma$ and an effective spring constant $\tilde{k}_f = 15\varepsilon/\sigma^2$. The remaining bead–bead interactions are modelled by a repulsive Week–Chandler–Andersen (WCA) potential[25,55] given explicitly in the ESI† which contains the size $\sigma$ of the repulsive monomers as a length and the repulsion strength $\varepsilon$, as the same energy scale as for the FENE potential. Henceforth we choose $\sigma$ and $\varepsilon$ as units of length and energy.

To incorporate the thermoresponsivity of the microgel particle effectively, a further attractive bead–bead pair potential[25] is added given by

$$V_\alpha(r) = \begin{cases} -\alpha\varepsilon & \text{if } r \le 2^{\frac{1}{6}}\sigma \\ \frac{1}{2}\alpha\varepsilon\left[\cos\left(\gamma\left(\frac{r}{\sigma}\right)^2 + \beta\right) - 1\right] & \text{if } 2^{\frac{1}{6}}\sigma < r \le R_0\sigma \\ 0 & \text{otherwise} \end{cases} \tag{1}$$

with $\gamma = \pi\left(2.25 - 2^{\frac{1}{3}}\right)^{-1}$ and $\beta = 2\pi - 2.25\gamma$.[58] Importantly, the effective attraction strength is controlled by the parameter $\alpha$, which mimics the quality of the solvent in an implicit manner. The value $\alpha = 1.55$ describes a strong attraction (relative to the bead repulsions) imitating poor solvent conditions[25,58] and therefore mimicking the collapsed state of the microgel. For good solvent conditions the value $\alpha = 0$ is used such that there is no attraction at all,[25,58] reflecting the swollen state. In our simulations, we varied the effective attraction strength $\alpha$ between the two extreme cases in the range $0 \le \alpha \le 1.55$ and refer to the $\alpha = 0$ case as the "fully swollen state" and the $\alpha = 1.55$ case as the "fully collapsed state". As the solvent quality is controlled by temperature in the experiments, $\alpha = 0$ corresponds to a low temperature, below the volume phase transition of the PNiPAm microgels, and $\alpha = 1.55$ to a high temperature situation above the volume phase transition. For the connection between the effective attraction strength $\alpha$ and the temperature dependence on PNiPAm microgels we refer to ref. 25. The internal architecture of the microgel particle is as in ref. 23, 25 and 55 and depends on the crosslinker density. In our simulations we represent each microgel particle by a total number of $N$ = 5500 beads, which includes a fraction of homogeneously distributed crosslinkers. The percentage of crosslinkers is an important parameter in our simulations and will be systematically varied between 0 and 4.5%.

To mimic the effect of an air–water interface, we follow ref. 50 and add an external potential; the potential is defined such that the interface normal is along the $z$ direction. Explicitly, for each bead, the external potential is a combination of an effective Lennard-Jones potential on the water side and a steep linear potential on the air side. We introduce a typical range $\sigma_{\mathrm{ext}}$ for the effective bead–interface interaction and a shifted $z$-coordinate $\tilde{z}$ by $\tilde{z} = z - 2^{\frac{1}{6}}\sigma_{\mathrm{ext}}$; the derivative of the potential (*i.e.* the force) is defined to be continuous at a matching point $\tilde{z}_a < 0$. In detail,

$$V_{\mathrm{ext}}(\tilde{z}) = \begin{cases} V_{\mathrm{LJ}}(\tilde{z}) & \tilde{z} \geq \tilde{z}_a \\ V_{\mathrm{LJ}}(\tilde{z}_a) + (\tilde{z}_a - \tilde{z})\left.\dfrac{\mathrm{d}V_{\mathrm{LJ}}(\tilde{z})}{\mathrm{d}\tilde{z}}\right|_{\tilde{z}=\tilde{z}_a} & \tilde{z} < \tilde{z}_a \end{cases} \tag{2}$$

with the Lennard-Jones potential

$$V_{\mathrm{LJ}}(\tilde{z}) = 4\varepsilon_{\mathrm{ext}}\left[\left(\frac{\sigma_{\mathrm{ext}}}{\tilde{z}}\right)^{12} - \left(\frac{\sigma_{\mathrm{ext}}}{\tilde{z}}\right)^{6}\right], \tag{3}$$

where $\varepsilon_{\mathrm{ext}}$ is an attraction energy strength. Therefore the interface tries to pin all beads to the position $\tilde{z}$ = 0 where the potential is minimal. Physically this attraction towards the interface results from surface tension reduction by reducing the bare air–water interfacial area when a bead is adsorbed at the interface. The large difference in the bead chemical potential between the air and the water phase is reflected by the steep increase of $V_{\mathrm{ext}}(\tilde{z})$ for $\tilde{z} < \tilde{z}_a$. In the following we have chosen $\varepsilon_{\mathrm{ext}} = 5.5\varepsilon$, to ensure a sufficiently strong adsorption strength towards the interface (a calculation for comparison with the experiment can be found in the ESI†), and $\sigma_{\mathrm{ext}} = 0.5\sigma$ corresponding to a relatively deep and stiff minimum around $\tilde{z}$ = 0. A harmonic expansion around the origin $\tilde{z}$ = 0 yields a large spring constant of $22\varepsilon/\sigma^2$ which is enforcing a bead monolayer as observed by the very thin corona formed by polymer chains expanding at the liquid interface. Finally we have chosen the matching position $z_a$, *i.e.* the point where the Lennard-Jones behavior changes to a constant force, as $\tilde{z}_a = -0.01\sigma$.

We simulate the bead dynamics as Brownian dynamics with an implicit solvent, whereby the short-time bead self-diffusion coefficient $D_0$ sets a characteristic Brownian time scale $\tau_{\mathrm{B}} = D_0/\sigma^2$. The latter defines our unit of time in the following. A finite time step of $\Delta t = 0.00005\tau_{\mathrm{B}}$ is used to integrate the equations of motion with an Euler forward scheme. All of the Brownian dynamics simulations are performed with the HOOMD-Blue package[59] and are visualized by OVITO.[60]

In our modelling it is important to distinguish between a solvent bath temperature $T^*$ – which sets the Brownian fluctuations – and the implicit temperature influence on the effective bead–bead attraction strength $\alpha$. Since the temperature change is small compared to the absolute room temperature, we have fixed the solvent bath temperature to $k_{\mathrm{B}}T^* = \varepsilon$ throughout all of our simulations but changed solely the effective attraction strength $\alpha$, in agreement with typical protocols in the literature.[23,25] For simplicity, there is no distinction between the interactions of the beads in the interface and in the bulk.

Our simulation protocol is as follows: first we equilibrate the microgel particle in the bulk (*i.e.* in the absence of the interface external potential (2)) and thus gain an equilibrated initial bead configuration. This is done separately for the ''fully swollen state'' with $\alpha$ = 0 and for the ''fully collapsed state'' with $\alpha$ = 1.55. We then instantaneously expose the initial bead configuration to the potential (2) such that the $z$-coordinate of the center of mass of the particle is a distance of $10\sigma$ apart from the interface position at $\tilde{z}$ = 0. We then relax the system for a long waiting time $t_{\mathrm{w}}$ of typically $5 \times 10^3\tau_{\mathrm{B}}$. The relaxed configuration is – in the presence of the interface – subject to a sudden change in the attraction parameter $\alpha$ from 0 to 1.55 or, respectively from 1.55 to 0. Physically this means that the solvent quality temperature is abruptly changed from high to low (or *vice versa*). We then allow the system to undergo relaxation for another waiting time; this relaxation process is referred to as ''collapsing'' (if $\alpha$ has been suddenly increased), or as ''swelling'' (if $\alpha$ has been suddenly decreased). Finally we reverse $\alpha$ to its initial value, thus establishing one ''cycle''. After a third waiting time the resulting configuration is compared to the first configuration at the same $\alpha$ relaxed at the interface from its initial bulk state. If there is a significant difference in the extent of the configuration, the system is called hysteretic. The protocol is repeated several times leading to a ''cycling process'' which is composed of alternating ''swelling'' and ''collapsing'' processes. Appropriate averages are taken to ensure that the behavior does not suffer from peculiarities of the initial configuration.

The diagnostics to identify hysteresis is done *via* monitoring the lateral radius of gyration, $R_{\mathrm{lat}}(t)$, as a function of time $t$. The lateral (or projected) radius of gyration is defined as

$$R_{\mathrm{lat}}{}^2(t) = \frac{1}{N}\sum_{i=1}^{N}(x_i(t) - X_0(t))^2 + (y_i(t) - Y_0(t))^2 \tag{4}$$

with $\vec{r}_i(t) = (x(t)),y(t),z(t))$ as the location of the bead $i$, and $\vec{R}_0(t) = (X_0(t), Y_0(t), Z_0(t)) = \frac{1}{N}\sum_{i=1}^{N}\vec{r}_i(t)$ is the instantaneous center of the microgel particle. Finally, we can also infer the lateral osmotic pressure from the fraction of beads in the interfacial region. Here, by definition, a bead is in the interfacial region if its $\tilde{z}$-coordinate lies between $-0.5\sigma$ and $0.5\sigma$. We also analyze the internal core–corona structure in more detail by using a ''hull parameter'' $\Delta(r)$, which brings us also into a position to extract a core radius $R_{\mathrm{c}}$ and an outer corona radius. Details of the procedure are described in the ESI.†

### 2.1 Experiments

PNiPAm microgels crosslinked by *N*,*N*′-methylenebis (acrylamide) with different crosslinking densities are synthesized by precipitation polymerisation according to a previously published protocol.[61] The cycling experiments involving the differently crosslinked microgels are conducted in a similar fashion as developed in an earlier publication.[50] When starting from the collapsed state, 0.05 w% microgels dispersed in an ethanol/water mixture (1 : 1) with a temperature of 70 °C are spread at the air/water interface on a Langmuir–Blodgett trough (KSV Nima), which is preheated to the initial temperature of 60 °C. Similarly, when starting from the swollen state, the microgel dispersion is spread at room temperature. The trough is heated using a thermostat by increasing the temperature by 10 °C every 10 minutes. Conversely, the trough is passively cooled by switching off the thermostat. The interfacial arrangement as a function of temperature is then deposited onto a silicon wafer $(0.5 \times 10\ \mathrm{cm}^2)$ lifted at $0.1\ \mathrm{mm\ min}^{-1}$ through the interface, while the corresponding surface pressure is measured using the Wilhelmy plate method. The microgels are characterized *ex situ* by image analysis of scanning electron microscopy (Zeiss Gemini 500) images of the transferred interfacial layer. From these images, the size of the microgel core is quantified by a custom-written Matlab software.[50]

## 3 Results and discussion

### 3.1 Non-hysteretic microgel swelling in the bulk

First, as a reference, we simulate the bulk behavior of a microgel. Fig. 2 shows the time evolution of the radius of gyration during swelling and collapsing together with typical initial and final simulation snapshots before and after the swelling and collapsing processes. The initial configurations (marked with (b) and (d)) are equilibrated for a long relaxation time of typically $5000\tau_B$, and are therefore practically fully relaxed. After a sudden increase (or decrease) of effective attraction $\alpha$ (mimicking an increase or decrease the temperature, respectively) the radius saturates quickly (*i.e.* within a relaxation time of roughly $1000\tau_B$) indicating equilibration. After a long relaxation for a simulation time of about $2500\tau_B$ two final configurations marked with (c) and (e) in Fig. 2 are reached. These two final configurations (c) and (e) are similar to the initial conditions (d) and (b) in Fig. 2, *i.e.* both swollen and both collapsed configurations exhibit a similar radius of gyration. Importantly, this implies that swelling and subsequent collapsing are completely reversible in this bulk experiment on the accessible time scale of the simulation, or in other terms, there is no hysteresis. This non-hysteretic bulk behavior in size is in agreement with experiments.[22] Once the reversible behavior of the volume phase transition is established, one can trivially add a cycle of subsequent swelling and collapsing processes, which always results in an equilibrated state. Likewise, one can perform a multi-cycle process by adding many subsequent swelling and collapsing processes. Again one finds reversible behavior such that after each cycling process the system is in the same equilibrated state. The latter feature will change significantly at interfaces which we shall show next.

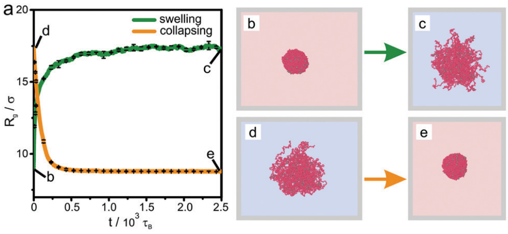

Fig. 2 (a) Volume phase transition of a microgel in bulk. Radius of gyration $R_g$ (in terms of the bead size $\sigma$) as a function of time $t$ for a microgel particle in the bulk for both a collapsing process (yellow line) and a swelling process (green line) with the corresponding error bars in black as obtained by simulation. The processes start from equilibrated configurations (shown as typical simulation snapshots (b) and (d)). Typical snapshots (c) and (e) after a long simulation time of $2500\tau_B$ are also given. There is no notable hysteresis in the bulk. The data are obtained for a crosslinking density of 4.5%.

### 3.2 Liquid interface-induced hysteresis of microgel morphology

**3.2.1 The swelling and collapsing process at the interface.** Next, a microgel with an equilibrated bulk configuration is placed at the interface *in silico* (as described in Materials and methods) and relaxed there for a long initial relaxation time of $5000\tau_B$. Subsequently, a swelling and collapsing process is initiated by an instantaneous change in the solvent quality, encoded in the effective attraction $\alpha$. The evolution of the lateral radius of gyration following this change of $\alpha$ is presented in Fig. 3 for both a swelling and a collapsing event. Similar to Fig. 2, typical initial and final snapshots are given in Fig. 3 both with a top view onto the microgel and a lateral view from the side. The side view clearly shows the oblate core–corona morphology[55,62] of the microgel, which is induced by lateral stretching caused by the reduction of the bare water–air interfacial tension. This is also accompanied by the fact that the lateral radius of gyration is significantly larger than its bulked value shown in Fig. 2. The important message taken from Fig. 3 is the presence of a hysteresis, observed from the difference in the collapsed dimensions for the two phase transition scenarios. In particular, the collapsed state (e′), reached after a relaxation time of $2500\tau$ from an initially swollen microgel at the interface, is much less contracted than the starting collapsed configuration (b′) from the initial interfacial adsorption of a bulk collapsed microgel. This difference is clearly evidenced by the different lateral radii of gyration, and is also consistent with previous experimental findings.[50,52,63]

The hysteretic behavior found for the volume phase transition at the interface in the collapsing process is in contrast to the swelling process where the swollen end state (c′) practically exhibits the same lateral radius of gyration as the initial state (d′) of a microgel adsorbed to the interface from a swollen bulk conformation. The clue to understand this difference lies in the

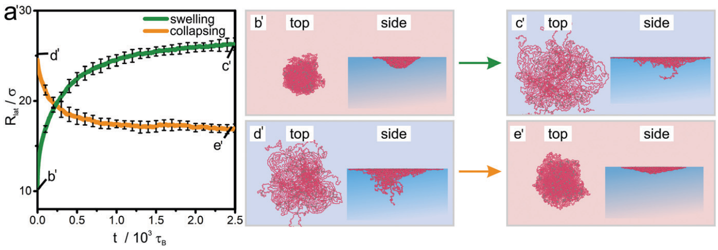

Fig. 3 (a) Volume phase transition of a microgel at an interface. Lateral radius of gyration $R_{\text{lat}}$ (in terms of the bead size $\sigma$) is shown as a function of time $t$ for a microgel at the liquid interface for both a collapsing process (yellow line) and a swelling process (green line) with the corresponding error bars in black as obtained by simulation. The processes are started from configurations relaxed at the interface for a total time of $5000\tau_B$ (shown as typical simulation snapshots (b′) and (d′). Typical snapshots (c′) and (e′) after a long relaxation time of $2500\tau_B$ are also given. There is a notable hysteresis for the collapsing but not for the swelling process. The data are obtained for a crosslinking density of 4.5%.

nature of the starting state (b′). In the collapsed state at the interface, the equilibration is kinetically hindered by the strong attractive interactions between the beads. Therefore we hypothesize that they are kinetically trapped since they cannot escape quickly to relax all constraints. If a swelling process is induced by improving the solvent quality, these constraints are released and the microgel relaxes faster to its equilibrium state. Again we emphasize that the allotted relaxation time at the interface for the collapsed state is long as compared to the typical time for swelling and collapsing in the simulation but not enough to achieve full equilibration. This "explosion" in relaxation time scales for interfacially collapsed states is in accordance with the experimental findings in literature.[50,52,63] Since the bead interactions are not affected by the interface, some parts of the polymer chains move back into the bulk as the attraction decreases which is probably due to the simplified assumption that the bead–bead interactions is the same in the interface and in the bulk. In the experiments typically a more complex relationship is encountered.[50]

**3.2.2 Temperature cycling.** We now go one step further and study a periodic sequence of swelling and subsequent collapsing processes in a cycling way. In particular, this procedure allows investigation whether the swollen state arising by swelling from an initial collapsed state is hysteretic upon further periodic decrease and increase of solvent quality (or temperature). Simulation data for such a cycling process are given in Fig. 4a. These data show an almost hysteresis-free behavior after one cycle. This gives evidence that the hysteretic behavior is mainly attributed to the collapsed initial state (b′). Once this adsorbed, collapsed microgel is swollen, the resulting interfacial state can almost reversibly be collapsed and swollen again without showing any further hysteresis in radius of gyration.

The hysteretic behavior is reflected in the two length scales characterizing the microgel particle, namely the lateral radius of gyration $R_{\text{lat}}$ and the core radius $R_c$ as documented in Fig. 4a. Indeed our analysis of the morphology by the hull parameter $\Delta(r)$ (Fig. S2, ESI†) reveals a clear distinction between core and corona for the different states in the cycling process and documents that our simulation scheme reproduces the fried-egg structure of a microgel at the interface.[1,2,47–49] The core region is much more compressed due to the interfacial attraction to the beads. Therefore the effect of kinetic arrest in the core is much more amplified when the particle is brought to the interface as compared to the bulk situation. This gives a clue to understand the underlying reason for the hysteretic behavior at the interface.

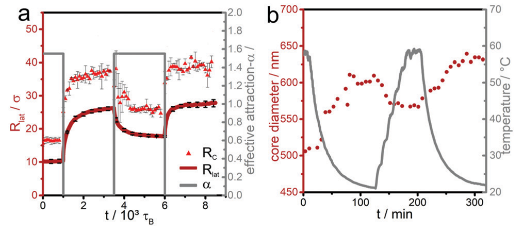

Fig. 4 Temperature cycling of a microgel at an interface. Cycling process of swelling and collapsing for a microgel particle initially collapsed at the interface. (a) Simulation data and (b) experimental data. A hysteresis within the first temperature cycle can be clearly observed for both simulation and experiment. The simulation data are obtained for a crosslinking density of 4.5% and the experimental data for a crosslinking density of 5%. The corresponding effective attraction parameter $\alpha$ and the solvent temperature are also shown as a function of time in (a) and (b) to illustrate the cyclic nature of the process. Two different length scales are shown in the simulation data in (a) which give the same qualitative trend, namely the core size $R_c$ and the lateral radius of gyration $R_{\text{lat}}$.

We compare the hysteresis observed in simulation with experimental data, obtained for an interfacial assembly of microgels on the air/water interface of a Langmuir trough exposed to changes in the temperature of the water subphase. The diameter of the microgel cores are quantified by image analysis of scanning electron microscopy images after transfer to a solid substrate. Interestingly, the experimental data shows a similar hysteretic behavior, evidenced by a change in core diameter between the initial adsorption in collapsed state and the first temperature cycling as seen in Fig. 4b. However, in the experiments the change of solvent quality (temperature) is not stepwise but smoothened due to experimental constraints (compare the gray line in Fig. 4b to the sharp jump of the effective attraction $\alpha$ shown along with the simulation data in

Fig. 4a). Simulations with a multiple stepwise change in effective attraction $\alpha$ have also been performed and are compared with the sudden stepwise change for a crosslinking density of 2.3%, see Fig. S1 ESI.† In this comparison, no significant difference in hysteresis was found for the two different forms of change.

### 3.3 Impact of the degree of crosslinking

**3.3.1 Impact of the degree of crosslinking on the hysteresis.** We now investigate the hysteretic behavior as a function of the degree of crosslinking. In Fig. 5 the interfacial volume phase transition upon temperature cycling is compared for three different crosslinking densities in simulation and experiment. The relative amount of hysteresis is quantified as $1 - \mathscr{R}$, where $\mathscr{R}$ is the ratio between the two microgel radii before and after the first cycling process. For the simulations, the ratio $\mathscr{R}$ is taken as $R_{\text{lat}}$ ($t$ = 1000$\tau_{\text{B}}$)/$R_{\text{lat}}$ ($t$ = 6000$\tau_{\text{B}}$), see Fig. 5a, and for the experiments we take for $\mathscr{R}$ the ratio of the two radii at times 210 min and 0 min, see Fig. 5b. In the absence of hysteresis, the two radii coincide such that $\mathscr{R}$ is one and the amount of hysteresis vanishes.

Both experimental and simulation data show that the relative amount of hysteresis decreases with increasing crosslinking density (Fig. 5c and d). We rationalize this behavior based on an intuitive argument stemming from the kinetics of the initially trapped state. For a more connected polymer network the microgel is more resistant against the stretching effect of the interface and therefore it is stretched out less. This explains why the hysteresis is smaller for higher crosslinking density. Conversely, if the degree of crosslinking is small, long dangling chains can be much more entangled and therefore contribute much more to the amount of hysteresis. Indeed in the extreme case of a single linear chain, additional simulation and experimental data indicate that the relative amount of hysteresis is even higher than the values found for the lowest crosslinking density of one percent; for simulation data see again Fig. 5c. The number of beads in the simulation of the linear chain is identical to that contained in the microgel particle, namely 5500 beads.

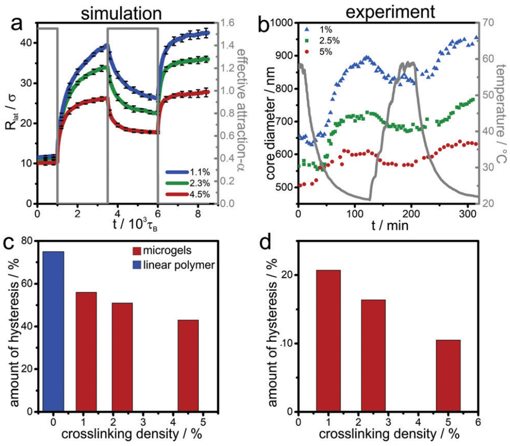

Fig. 5 Temperature cycling for different crosslinking densities. Cycling process of swelling and collapsing for microgel particles with different crosslinking densities initially collapsed at the interface: (a) simulation data and (b) experimental data. Hysteresis within one cycle can be clearly observed for both simulation and experiment. On the simulation side the lateral radius of gyration $R_{\text{lat}}$ is used for comparison. The corresponding effective attraction parameter $\alpha$ and the solvent temperature are also shown as a function of time in (a) and (b) to illustrate the cyclic nature of the process. The relative amount of hysteresis as a function of the crosslinking density: (c) simulation, (d) experimental data. Simulation data for the special case of a linear polymer are added as well for comparison (blue).

**3.3.2 Comparison of a microgel and a linear chain in terms of the surface pressure.** We now consider the surface pressure of an interfacial microgel layer as a function of temperature, which can be measured in experiments. Care has be taken in the interpretation of the effect of microgels on the surface pressure, since the air/water surface tension also changes with temperature. As the latter shows a monotonic decrease, we attribute any deviation from such a linear behavior to the microgel layer and therefore subtract the change in surface pressure of water from the plotted data. Therefore, we refrain here from a full quantitative comparison between experiment and simulation but only consider qualitative trends.

In the experimental system, the decrease in surface tension in the presence of microgels (or, the increase in surface pressure) relates to the surface density of PNiPAm chains adsorbed to the air/water interface. In simulations, the corresponding quantity is the surface density of adsorbed beads, which is directly accessible. Fig. 6a and c compares the evolution of the adsorbed microgel fraction determined in simulation with the surface pressure measured in experiment as a function of the effective attraction $\alpha$ or the temperature, respectively. The data are obtained by starting with an interfacially adsorbed microgel with high effective attractions $\alpha$ resp. high temperature $T$ (solid points). This initially collapsed microgel is then slowly swollen at the interface by a decrease the attraction (resp. temperature), as shown by blue points/blue line. The swelling increases the area occupied by the microgel (see above), and thus decreases the surface tension – or increases the surface pressure in experiment (Fig. 6c). Concomitantly, the swelling causes more beads to adsorb to the interface as the system passes through the volume phase transition (Fig. 6a and b).

Notably, the maximal number of adsorbed beads occurs closely at $\alpha \approx 0.6$ where the bulk collapse transition happens[23,25] and is thus correlated to the bulk volume transition. Interestingly, in the simulation data, a slight decrease of the adsorbed beads is absorbed when the attraction vanishes. This is due to the fact that parts of the chains go back into the bulk due to entropic reasons. The swollen microgels are subsequently collapsed (or heated) again. The red data points/red line in Fig. 6a–c show the associated evolution of the adsorbed fraction of microgel beads (simulations) and surface pressure (experiments), respectively. In both experiment and simulation, a hysteresis is observed, in agreement with the data shown before.

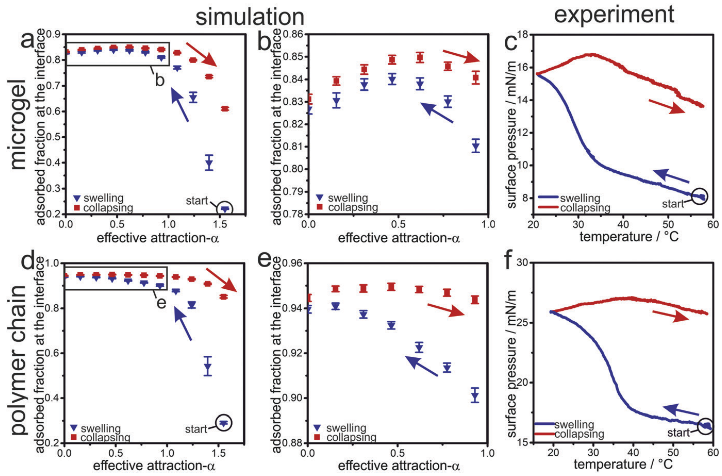

Fig. 6 Surface pressure cycle for different crosslinking densities. Evolution of surface pressure during the volume phase transition at interfaces, for a microgel and a linear polymer chain. (a) Simulation data for a microgel (2.3% crosslinking density). (b) A zoom-in for the microgel simulation data for effective attractions $\alpha$ between 0 and 1. (c) Experimental data for a PNiPAm microgel (2.5% crosslinking density). (d) Simulation data for a linear polymer chain. (e) A zoom-in for the linear polymer chain for effective attractions $\alpha$ between 0 and 1. (f) Experimental data for a linear PNiPAm polymer chain. A hysteretic behaviour of the volume phase transition is observed for both microgel and linear polymer chain in simulation and experiment.

The fraction of adsorbed beads and the surface pressure increases for this increase in $\alpha$ or temperature, compared to the initial values at low temperature culminating in a maximum at a temperature which roughly coincides with the bulk volume transition. We interpret this maximum as a joint effect of the interfacial attraction to the beads and the effective attraction between the beads. When the bulk volume transition temperature is reached from below, the bulk attraction wins and drags beads from the interface into the bulk. We remark that upon cooling a similar maximum is found in the simulations but not in the experiments; the reason for this slight discrepancy remains unclear.

Finally, as a reference, we also show data for a linear polymer chain in Fig. 6d–f. The linear chain shows similar trends in the surface pressure and the fraction of the adsorbed monomers as the microgel, but there is no maximum in the adsorbed bead fraction during the swelling process. Thus the curves coincide nicely.

## 4 Conclusions

We used monomer-resolved computer simulations and air/water-interfacial experiments to investigate the volume phase transition of PNiPAm microgels in bulk and adsorbed to an interface. Our results underline that the presence of an interface significantly changes the volume phase transition. Particularly, we found a significant hysteretic behavior for microgels undergoing the phase transition at the interface. A microgel adsorbed in the collapsed state to the interface does not return to its initial configuration when subjected to a temperature cycle. Instead, it relaxes into a more stretched configuration. An initially swollen microgel, however, undergoes reversible transitions between collapsed and swollen states upon temperature cycling. We therefore attribute the hysteresis effect of the collapsed microgel at the interface to a kinetically trapped initial state which can be released by swelling the microgel. Essentially the same results can also be observed for an oil–water interface.[50,52] We find that the hysteresis is more pronounced for weaker degree of crosslinking and is even observed for linear PNiPAm chains.

Our results demonstrate that it is possible to model complex polymer-interface phenomena *via* a comparably simple model that balances internal and interfacial attractions. This modelling approach may therefore also be transferred to other stimuli-responsive polymer systems, curved interfaces, or more crowded systems formed by multiple, overlapping interfacial microgels.

## Conflicts of interest

There are no conflicts to declare.

## Acknowledgements

N. V., H. L. and L. M. C. J. acknowledge funding from the Deutsche Forschungsgemeinschaft (DFG) under grant numbers VO 1824/8-1 and LO 418/22-1, respectively. N. V. also acknowledges support by the Interdisciplinary Center for Functional Particle Systems (FPS). J. K. thanks Jens Grauer for helpful discussions.

## Notes and references

1 K. Geisel, L. Isa and W. Richtering, *Langmuir*, 2012, **28**, 15770–15776.

2 M. Rey, M. A. Fernandez-Rodriguez, M. Karg, L. Isa and N. Vogel, *Acc. Chem. Res.*, 2020, **53**, 414–424, DOI: 10.1021/acs.accounts.9b00528.

3 R. Pelton, *Adv. Colloid Interface Sci.*, 2000, **85**, 1–33, DOI: 10.1016/S0001-8686(99)00023-8.

4 M. Karg, A. Pich, T. Hellweg, T. Hoare, L. A. Lyon, J. J. Crassous, D. Suzuki, R. A. Gumerov, S. Schneider, I. I. Potemkin and W. Richtering, *Langmuir*, 2019, **35**, 6231–6255.

5 R. Keidel, A. Ghavami, D. M. Lugo, G. Lotze, O. Virtanen, P. Beumers, J. S. Pedersen, A. Bardow, R. G. Winkler and W. Richtering, *Sci. Adv.*, 2018, **4**, eaao7086, DOI: 10.1126/sciadv.aao7086.

6 Z. Li and T. Ngai, *Nanoscale*, 2013, **5**, 1399–1410.

7 T. Ngai, S. H. Behrens and H. Auweter, *Chem. Commun.*, 2005, 331–333, DOI: 10.1039/B412330A.

8 V. Schmitt and V. Ravaine, *Curr. Opin. Colloid Interface Sci.*, 2013, **18**, 532–541.

9 M. A. Fernandez-Rodriguez, A. Martín-Molina and J. Maldonado-Valderrama, *Adv. Colloid Interface Sci.*, 2021, **288**, 102350, DOI: 10.1016/j.cis.2020.102350.

10 M.-C. Tatry, P. Galanopoulo, L. Waldmann, V. Lapeyre, P. Garrigue, V. Schmitt and V. Ravaine, *J. Colloid Interface Sci.*, 2021, **589**, 96–109.

11 D. Klinger and K. Landfester, *Polymer*, 2012, **53**, 5209–5231.

12 F. Wang, Z. Zheng, Y. Peng, Y. Han and Z. Wang, *Science*, 2012, **338**, 87–90.

13 A. M. Alsayed, M. F. Islam, J. Zhang, P. J. Collings and A. G. Yodh, *Science*, 2005, **309**, 1207–1210.

14 Y. Peng, F. Wang, Z. Wang, A. M. Alsayed, Z. Zhang, A. G. Yodh and Y. Han, *Nat. Mater.*, 2015, **14**, 101–108.

15 F. Grillo, M. A. Fernandez-Rodriguez, M. N. Antonopoulou, D. Gerber and L. Isa, *Nature*, 2020, **582**, 219–224.

16 S. Ciarella, M. Rey, J. Harrer, N. Holstein, M. Ickler, H. Löwen, N. Vogel and L. M. C. Janssen, 2020, arXiv preprint arXiv:2008.13695.

17 K. Volk, F. Deißenbeck, S. Mandal, H. Löwen and M. Karg, *Phys. Chem. Chem. Phys.*, 2019, **21**, 19153–19162.

18 L. T. Lee, B. Jean and A. Menelle, *Langmuir*, 1999, **15**, 3267–3272.

19 H. Senff and W. Richtering, *J. Chem. Phys.*, 1999, **111**, 1705–1711.

20 K. Shiraga, H. Naito, T. Suzuki, N. Kondo and Y. Ogawa, *J. Phys. Chem. B*, 2015, **119**, 5576–5587.

21 G. M. Conley, S. Nöjd, M. Braibanti, P. Schurtenberger and F. Scheffold, *Colloids Surf., A*, 2016, **499**, 18–23.

22 K. Kratz, T. Hellweg and W. Eimer, *Polymer*, 2001, **42**, 6631–6639.

23 L. Rovigatti, N. Gnan and E. Zaccarelli, *J. Phys.: Condens. Matter*, 2017, **30**, 044001.

24 F. Camerin, N. Gnan, L. Rovigatti and E. Zaccarelli, *Sci. Rep.*, 2018, **8**, 14426–14438, DOI: 10.1038/s41598-018-32642-5.

25 N. Gnan, L. Rovigatti, M. Bergman and E. Zaccarelli, *Macromolecules*, 2017, **50**, 8777–8786.

26 G. Del Monte, A. Ninarello, F. Camerin, L. Rovigatti, N. Gnan and E. Zaccarelli, *Soft Matter*, 2019, **15**, 8113–8128.

27 A. J. Moreno and F. L. Verso, *Soft Matter*, 2018, **14**, 7083–7096.

28 T. J. Weyer and A. R. Denton, *Soft Matter*, 2018, **14**, 4530–4540.

29 M. Quesada-Pérez, J. Ramos, J. Forcada and A. Martn-Molina, *J. Chem. Phys.*, 2012, **136**, 244903.

30 M. Brugnoni, A. Scotti, A. A. Rudov, A. P. Gelissen, T. Caumanns, A. Radulescu, T. Eckert, A. Pich, I. I. Potemkin and W. Richtering, *Macromolecules*, 2018, **51**, 2662–2671.

31 A. Scotti, A. R. Denton, M. Brugnoni, J. E. Houston, R. Schweins, I. I. Potemkin and W. Richtering, *Macromolecules*, 2019, **52**, 3995–4007.

32 S. Nikolov, A. Fernandez-Nieves and A. Alexeev, *Appl. Math. Mech.*, 2018, **39**, 47–62.

33 A. R. Denton and Q. Tang, *J. Chem. Phys.*, 2016, **145**, 164901.

34 M. M. Hedrick, J. K. Chung and A. R. Denton, *J. Chem. Phys.*, 2015, **142**, 034904.

35 G. Giupponi, D. M. A. Buzza and D. B. Adolf, *Macromolecules*, 2007, **40**, 5959–5965.

36 Y. Hertle, M. Zeiser, C. Hasenöhrl, P. Busch and T. Hellweg, *Colloid Polym. Sci.*, 2010, **288**, 1047–1059.

37 C. G. Lopez and W. Richtering, *Soft Matter*, 2017, **13**, 8271–8280.

38 D. Zhi, Y. Huang, X. Han, H. Liu and Y. Hu, *Chem. Eng. Sci.*, 2010, **65**, 3223–3230.

39 W. Toh, T. Y. Ng, J. Hu and Z. Liu, *Int. J. Solids Struct.*, 2014, **51**, 4440–4451.

40 U. Baul and J. Dzubiella, 2020, arXiv preprint arXiv:2011.03398.

41 Y. C. Lin, B. Rotenberg and J. Dzubiella, *Phys. Rev. E*, 2020, **102**, 42602.

42 A. Moncho-Jordá and J. Dzubiella, *Phys. Chem. Chem. Phys.*, 2016, **18**, 5372–5385.

43 G. Giupponi and D. Buzza, *J. Chem. Phys.*, 2004, **120**, 10290–10298.

44 Surface Tension of Water from Dortmund Data Bank, http://www.ddbst.com/en/EED/PCP/SFT{_}C174.php.

45 E. S. A. Goerlitzer, R. Mohammadi, S. Nechayev, K. Volk, M. Rey, P. Banzer, M. Karg and N. Vogel, *Adv. Mater.*, 2020, **32**, 2070173, DOI: 10.1002/adma.202070173.

46 B. M. Rey, R. Elnathan, R. Ditcovski, K. Geisel, M. Zanini, M. A. Fernandez-Rodriguez, V. V. Naik, A. Frutiger, W. Richtering, T. Ellenbogen, N. H. Voelcker and L. Isa, *Nano Lett.*, 2016, **16**, 157–163, DOI: 10.1021/acs.nanolett.5b03414.

47 R. W. Style, L. Isa and E. R. Dufresne, *Soft Matter*, 2015, **11**, 7412–7419.

48 H. Mehrabian, J. Harting and J. H. Snoeijer, *Soft Matter*, 2016, **12**, 1062–1073.

49 K. Zielińska, H. Sun, R. A. Campbell, A. Zarbakhsh and M. Resmini, *Nanoscale*, 2016, **8**, 4951–4960.

50 J. Harrer, M. Rey, S. Ciarella, H. Löwen, L. M. Janssen and N. Vogel, *Langmuir*, 2019, **35**, 10512–10521.

51 S. Bochenek, A. Scotti, W. Ogieglo, M. Á. Fernández-Rodríguez, M. F. Schulte, R. A. Gumerov, N. V. Bushuev, I. I. Potemkin, M. Wessling, L. Isa and W. Richtering, *Langmuir*, 2019, **35**, 16780–16792.

52 S. Bochenek, A. Scotti and W. Richtering, *Soft Matter*, 2021, **17**, 976–988, DOI: 10.1039/D0SM01774D.

53 Z. Li, W. Richtering and T. Ngai, *Soft Matter*, 2014, **10**, 6182–6191.

54 F. Camerin, N. Gnan, J. Ruiz-Franco, A. Ninarello, L. Rovigatti and E. Zaccarelli, *Phys. Rev. X*, 2020, **10**, 031012.

55 F. Camerin, M. A. Fernandez-Rodrguez, L. Rovigatti, M.-N. Antonopoulou, N. Gnan, A. Ninarello, L. Isa and E. Zaccarelli, *ACS Nano*, 2019, **13**, 4548–4559.

56 M. J. Bergman, N. Gnan, M. Obiols-Rabasa, J.-M. Meijer, L. Rovigatti, E. Zaccarelli and P. Schurtenberger, *Nat. Commun.*, 2018, **9**, 5039–5050, DOI: 10.1038/s41467-018-07332-5.

57 L. Rovigatti, N. Gnan, A. Ninarello and E. Zaccarelli, *Macromolecules*, 2019, **52**, 4895–4906.

58 T. Soddemann, B. Dünweg and K. Kremer, *Eur. Phys. J. E: Soft Matter Biol. Phys.*, 2001, **6**, 409–419.

59 J. A. Anderson, J. Glaser and S. C. Glotzer, *Comput. Mater. Sci.*, 2020, **173**, 109363.

60 A. Stukowski, *Modell. Simul. Mater. Sci. Eng.*, 2009, **18**, 015012.

61 M. Rey, X. Hou, J. S. J. Tang and N. Vogel, *Soft Matter*, 2017, **13**, 8717–8727.

62 K. Geisel, L. Isa and W. Richtering, *Langmuir*, 2012, **28**, 15770–15776.

63 M. F. Schulte, A. Scotti, M. Brugnoni, S. Bochenek, A. Mourran and W. Richtering, *Langmuir*, 2019, **35**, 14769–14781.

Cite this: DOI: 00.0000/xxxxxxxxxx

# Interface-induced hysteretic volume phase transition of microgels: simulation and experiment

Jannis Kolker,*[a] Johannes Harrer,‡[b] Simone Ciarella,[c] Marcel Rey,[b] Maret Ickler,[b] Liesbeth M. C. Janssen,[c] Nicolas Vogel,[b] and Hartmut Löwen[a]

Received Date
Accepted Date

DOI: 00.0000/xxxxxxxxxx

Supporting Information

## 1 Materials and Methods

### 1.1 Bead and bond potentials

The bead-bead interaction is modeled by a Weeks-Chandler-Andersen[1] potential

$$V_{\mathrm{WCA}}(r) = \begin{cases} 4\varepsilon\left[\left(\frac{\sigma}{r}\right)^{12} - \left(\frac{\sigma}{r}\right)^{6}\right] + \varepsilon & \text{if} \quad r \leq 2^{\frac{1}{6}}\sigma \\ 0 & \text{otherwise} \end{cases} \tag{1}$$

where $r$ is the radial distance between two beads, $\sigma$ represents the bead diameter and $\varepsilon$ is the strength of repulsion. The bead-connecting covalent bonds are described by a finite-extensible-nonlinear-elastic (FENE) [2,3] potential

$$V_{\mathrm{FENE}}(r) = \begin{cases} -\tilde{k}_{\mathrm{F}}\tilde{R}_0^2 \ln\left(1 - \left(\frac{r}{\tilde{R}_0}\right)^2\right) & \text{if} \quad r < \tilde{R}_0 \\ 0 & \text{otherwise} \end{cases} \tag{2}$$

with $\tilde{k}_{\mathrm{F}} = 15\varepsilon/\sigma^2$ an effective spring constant and $\tilde{R}_0 = 1.5\sigma$ the maximal bond expansion.

### 1.2 Attractive interfacial energies in simulation and experiment

In the experiment, a surface tension difference $\gamma_{\mathrm{a/w}} - \gamma_{\mathrm{a/w/PNiPAm}}$ of the air/water surface tension $\gamma_{\mathrm{a/w}}$ and a surface tension of an adsorbed PNiPAm microgel $\gamma_{\mathrm{a/w/PNiPAm}}$ was measured for an interfacial layer of microgels. The surface tension difference was found to be approximately $30\frac{\mathrm{mJ}}{\mathrm{m}^2}$ at a temperature of $T^* = 293\mathrm{K}$. The interface attraction energy $\varepsilon_{\mathrm{ext}}$ for a single monomer can be calculated via

$$\varepsilon_{\mathrm{ext}} = \left(\gamma_{\mathrm{a/w}} - \gamma_{\mathrm{a/w/PNiPAm}}\right)\pi R_{\mathrm{mono}}^2, \tag{3}$$

with $R_{\mathrm{mono}} \approx 0.5\,\mathrm{nm}$ as a typical monomer radius. Consequently, this leads to an effective interface attraction energy of $5.5\,\mathrm{k_B T^*}$, as chosen in the simulation. In principle, $\varepsilon_{\mathrm{ext}}$ should be temperature-dependent via the temperature-dependence surface tension of water but we have neglected this dependence as the surface tension only varies about less than ±5% within the temperature regime considered.

### 1.3 Comparison of a sudden and an multiple stepwise change of the effective attraction $\alpha$

In order to mimick more the experimental situation of stepwise cooling and heating, we have also changed the effective attraction $\alpha$ in a multiple stepwise manner slower than a stepwise manner. For the crosslinking density of 2.3%, corresponding data are shown in Figure 1. While qualitative differences exist, the amount of stretching for the swollen state and the subsequent collapsed state is approximately the same. Hence, no major differences in the net hysteresis are found for different cooling and heating speeds.

---

[a] *Institut fur Theoretische Physik II, Heinrich-Heine-Universität Düsseldorf, Universitätsstrasse 1, D-40225 Düsseldorf, Germany.*
[b] *Institute of Particle Technology, Friedrich-Alexander University Erlangen-Nürnberg, Cauerstrasse 4, 91058 Erlangen, Germany.*
[c] *Theory of Polymers and Soft Matter, Department of Applied Physics, Eindhoven University of Technology, P.O. Box 513, 5600MB Eindhoven, The Netherlands.*

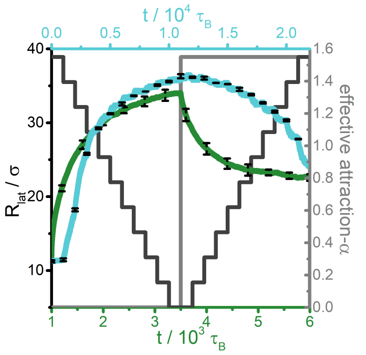

Fig. 1 Simulation data for a temperature cycling of a microgel at an interface for a multiple stepwise (black line) and a sudden (grey line) change in the effective attraction $\alpha$. The sudden change (green line) and the multiple stepwise change (blue line) are reaching the same amount of stretching for the swollen state and for the subsequent collapsed state. The data are obtained for a crosslinking density of 2.3%

### 1.4 Core-corona structure

We characterize the internal core-corona structure of the microgel by a geometric analysis of the bead configurations. The main idea is as follows: we consider all bead positions projected to the $xy$-plane which have a distance less than a prescribed $r$ from the (stationary) microgel center $\vec{R}_0$, i.e. all bead positions which fulfill $(x_i(t) - X_0(t))^2 + (y_i(t) - Y_0(t))^2 < r$. In the corona region we expect that the set of bead positions exhibits a relatively rough boundary while in the core region the boundary is fairly smooth.

To quantify this further we consider the convex hull around the set of bead positions which provides a contour length $L_{convex}(r)$. We also define a *concave* hull around the same bead positions and compare its contour length $L_{concave}(r)$ to $L_{convex}(r)$. Clearly, $L_{concave}(r) \geq L_{convex}(r)$. In contrast to the convex contour, the precise definition of the concave hull is not unique. In detail, for the calculation of the concave hull we employed the algorithm in Ref. [4] with the so-called $k$-nearest-neighbour approach where we used $k = 20$.

The relative difference in the two contour lengths defines a parameter $\Delta(r)$

$$\Delta(r) = \frac{L_{\mathrm{concave}}(r) - L_{\mathrm{convex}}(r)}{L_{\mathrm{concave}}(r)} \tag{4}$$

The spatial dependence of $\Delta(r)$ contains valuable information about the core size $R_{\mathrm{c}}$ and the corona size $R_{\mathrm{co}}$. Inside the core $\Delta$ is small while it increases for increasing $r$ until it saturates with a value $\Delta_\infty$ of the order of one, concomitant with a "rugged" concave hull. We can therefore extract the core and corona size approximatively by studying the behavior of $\Delta(r)$ near its inflection point at $r = r^*$ defined by the condition $d^2\Delta(r)/dr^2|_{r=r^*} = 0$. Considering the tangent $\tilde{t}(r)$ through the inflection point given by the linear relation $\tilde{t}(r) = \Delta(r^*) + d\Delta(r)/dr|_{r=r^*} \times (r - r^*)$, we define the core size $R_{\mathrm{c}}$ by the intersection of the tangent with the $r$-axis, i.e. by the condition $\tilde{t}(R_{\mathrm{c}}) = 0$. The corona size is defined by the distance where the tangent reaches the saturation value $\Delta_\infty$, i.e. by the relation $\tilde{t}(R_{\mathrm{co}}) = \Delta_\infty$.

Concrete data for a typical microgel snapshot along with the profiles for $\Delta(r)$ are presented in figure 2i)-iii) corresponding to three different situations: i) initially collapsed state of a microgel particle brought to the interface from the bulk, ii) swollen microgel particle at the interface after the first temperature change, iii) collapsed state after one full cycle. The associated concave and convex hulls for the inner and outer part are indicated in different colors. Moreover, in figure 2iv)-vi) the corresponding profiles $\Delta(r)$ are presented together with the tangent $\tilde{t}(r)$ (full red line) and the determination of the core size $R_{\mathrm{c}}$ and the corona size $R_{\mathrm{co}}$.

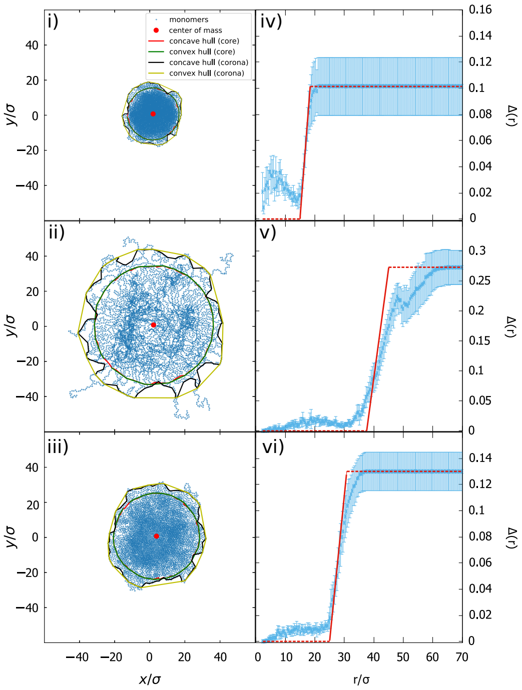

Fig. 2 i)-iii) Typical bead configurations for a crosslinking density of 4.5% at the interface (top view) for the initial collapsed state i), the swollen state ii) and the collapsed state after one cycle iii). Different hulls for the core and corona are indicated in different colors (see legend). The corresponding $\Delta(r)$-profiles are shown in iv), v) and vi) with error bars. The tangent on the $\Delta(r)$-profile is shown as a full red line, the intersection point with the dashed lines indicates the core and corona size.

## Notes and references

1 J. D. Weeks, D. Chandler and H. C. Andersen, *The Journal of Chemical Physics*, 1971, **54**, 5237–5247.

2 N. Gnan, L. Rovigatti, M. Bergman and E. Zaccarelli, *Macromolecules*, 2017, **50**, 8777–8786.

3 F. Camerin, M. A. Fernandez-Rodríguez, L. Rovigatti, M.-N. Antonopoulou, N. Gnan, A. Ninarello, L. Isa and E. Zaccarelli, *ACS nano*, 2019, **13**, 4548–4559.

4 A. Moreira and M. Y. Santos, *GRAPP 2007 - 2nd International*

*Conference on Computer Graphics Theory and Applications, Proceedings*, 2007, **GM**, 61–68.

# P2 Elastic Deformations of Spherical Core-Shell Systems Under an Equatorial Load

Reproduced from

J. Kolker, L. Fischer, Andreas M. Menzel and H. Löwen,
*Elastic Deformations of Spherical Core-Shell Systems Under an Equatorial Load,*
Journal of Elasticity, 2022,

Digital Object Identifier (DOI): `https://doi.org/10.1007/s10659-022-09897-1`

## Statement of contribution

I drafted parts of the main text, performed most of the calculations and prepared all figures. LF thoroughly checked all calculations and discussed the calculations as well as the underlying theory with me. All authors discussed the results and edited the manuscript.

## Copyright and license notice

Journal of Elasticity
https://doi.org/10.1007/s10659-022-09897-1

# Elastic Deformations of Spherical Core-Shell Systems Under an Equatorial Load

**Jannis Kolker**[1] · **Lukas Fischer**[2] · **Andreas M. Menzel**[2] · **Hartmut Löwen**[1]

Received: 7 January 2022 / Accepted: 4 May 2022

## Abstract

Macroscopic elastic core-shell systems can be generated as toy models to be deformed and haptically studied by hand. On the mesoscale, colloidal core-shell particles and microgels are fabricated and investigated by different types of microscopy. We analyse, using linear elasticity theory, the response of spherical core-shell systems under the influence of a line density of force that is oriented radially and acts along the equator of the outer surface. Interestingly, deformational coupling of the shell to the core can determine the resulting overall appearance in response to the forces. We address various combinations of radii, stiffness, and Poisson ratio of core and shell and illustrate the resulting deformations. Macroscopically, the situation could be realized by wrapping a cord around the equator of a macroscopic model system and pulling it tight. On the mesoscale, colloidal microgel particles symmetrically confined to the interface between two immiscible fluids are pulled radially outward by surface tension.

**Keywords** Linear elasticity theory · Core-shell system · Deformation under external load · Continuum theory

**Mathematics Subject Classification** 74B10 · 74A10 · 74A30

## 1 Introduction

Solid sphere-like core-shell systems containing an inner part, the core, of elastic properties different from a surrounding outer part, the shell, are encountered in various contexts on different length scales. On large macroscopic scales, many stars, planets and moons can be approximated by a core and a shell of different elasticity [1]. Jelly sweets covered by a solid layer represent a popular example of not only mechanical or haptic but also culinary experience. Conversely, on the mesoscopic colloidal scale and even down to the nanoscale,

---

✉ J. Kolker

✉ L. Fischer

[1] Institut für Theoretische Physik II, Heinrich-Heine-Universität Düsseldorf, Universitätsstraße 1, 40225 Düsseldorf, Germany

[2] Institut für Physik, Otto-von-Guericke-Universität Magdeburg, Universitätsplatz 2, 39106 Magdeburg, Germany

there are numerous soft matter systems involving core-shell particles. These can be prepared in various ways [2, 3] as spherical colloidal particles with a polymer coating [4–6], as micelles [7] or as polymer networks with different crosslinking degrees in the inner and outer part [8–10]. Their controlled fabrication is not only pivotal for applications (such as microreactors [11, 12], targeted drug delivery [13, 14] or smart elastic materials [15, 16]). They also serve as model systems to tailor effective repulsive square-shoulder potentials [17–27] and to understand fundamental questions of statistical mechanics such as freezing and glass formation [4, 28–30].

Our focus in this work is laid on the coupled elastic deformation of inner and outer part, that is core and shell, respectively. We address spherical elastic systems when exposed to a radially oriented force line density along the equatorial circumference of the shell. This setup is motivated by the elasticity problem underlying colloidal core-shell microgel particles that are adsorbed to the interface between two immiscible fluids. At their common contact line, the two fluids pull on the shell of the microgel particle approximately in a radially outward direction in a symmetric setup [31–33]. In many of such interfacial situations, the wetting properties of the surface of a material are crucial for adsorption. A core-shell system provides an appropriate opportunity to adjust by a shell these surface wetting properties to the current need. At the same time, the elastic properties of the core under the influence of an interface are explored. Moreover, the particles may be density matched or functionalized, for example integrating magnetic behaviour, by the selected core material [34–36]. On macroscopic toy model systems, the force densities can be applied by hand, while on even larger, global scales atmospheric effects may lead to equatorially located line-like force densities on planets. An example is the thin area of low atmospheric pressure located around the equator of the earth in the inter-tropical convergence zone. In view of these different systems and situations, the imposed equatorial line force density can either be oriented radially inward (compressive) or radially outward (tensile). In the mathematical treatment this difference is represented by an inversion of the sign of the load.

In this paper, we study the underlying elasticity problem. We present a general continuum theory to compute and predict the shape change of an elastic core-shell system when loaded by an equatorial ring of line force density. Importantly not only the shell deforms, but also the inner core, and the two deformations are coupled to each other by the overall architecture. Through this coupling, the core can influence or even determine the type of deformation of the shell, although the load is applied from outside to the shell, not to the core. We analyse the resulting change of shape in detail, as a function of the relative size of core and shell, different mechanical stiffness of core and shell, as well as their compressibility. In particular, we include the possibility of an elastic *auxetic* response [37–42]. The latter is characterized by a negative Poisson ratio, i.e. when stretched along one axis the system expands along the perpendicular axes. Materials exhibiting corresponding elastic properties have been identified, constructed and analysed [43–46]. In particular it is interesting to consider core and shell materials with different Poisson ratios, as their competition can result in qualitatively different modes of deformation. Our study links to previously investigated geometries, particularly spherical one-component systems [47] or hollow capsules [48] as special cases. Moreover, our additional predictions can be verified by experiments on different scales.

## 2 Theory and Geometry

Within linear elasticity theory, small deformations of elastic materials are described. The position $\mathbf{r}$ of a material element can be mapped to its position $\mathbf{r}'$ in the deformed state by adding the displacement vector $\mathbf{u}$. The displacement field $\mathbf{u}(\mathbf{r})$ in the bulk satisfies the homogeneous Navier-Cauchy equations [49]

$$(1-2\nu)\nabla^2\mathbf{u}(\mathbf{r}) + \nabla(\nabla\cdot\mathbf{u}(\mathbf{r})) = \mathbf{0} \tag{1}$$

with $-1 < \nu \leq 1/2$ denoting the Poisson ratio of the elastic substance in three-dimensional situations [50]. Materials with $\nu = 1/2$ are incompressible, while those with negative Poisson ratio are referred to as *auxetic* materials [50]. The latter, when stretched along a certain axis, expand along the lateral directions (instead of undergoing lateral contraction). We ignore any force acting on the bulk, for example gravity. Consequently, in the bulk, the right-hand side of Eq. (1) is set equal to zero.

Furthermore, linear elasticity theory for homogeneous isotropic materials dictates the stress-strain relation [50]

$$\frac{E}{1+\nu}\left(\underline{\boldsymbol{\varepsilon}}(\mathbf{r}) + \frac{\nu}{1-2\nu}\mathrm{Tr}\left(\underline{\boldsymbol{\varepsilon}}(\mathbf{r})\right)\underline{\mathbf{I}}\right) = \underline{\boldsymbol{\sigma}}(\mathbf{r}). \tag{2}$$

Equation (2) describes the relationship between the strain tensor $\underline{\boldsymbol{\varepsilon}}(\mathbf{r}) = \left(\nabla\mathbf{u}(\mathbf{r}) + (\nabla\mathbf{u}(\mathbf{r}))^{\mathrm{T}}\right)/2$ as the symmetrized gradient of the displacement field $\mathbf{u}(\mathbf{r})$ and the symmetric Cauchy stress tensor $\underline{\boldsymbol{\sigma}}$ (we mark second-rank tensors and matrices by an underscore). $E$ is the Young modulus of the elastic material and $\underline{\mathbf{I}}$ is the unit matrix. The Young modulus $E$ and the Poisson ratio $\nu$ are sufficient to quantify the properties of a homogeneous isotropic elastic material.

The boundary conditions at the surface of the elastic shell are

$$\underline{\boldsymbol{\sigma}}(\mathbf{r})\cdot\mathbf{n} = \frac{\lambda}{R_{\mathrm{s}}}\delta\left(\theta - \frac{\pi}{2}\right)\mathbf{n}. \tag{3}$$

Here, $\mathbf{n}$ describes the outward normal unit vector of the surface and $\delta\left(\theta - \frac{\pi}{2}\right)/R_{\mathrm{s}}$, with $\delta$ the Dirac delta function, sets the location of the line at which the loading force line density of amplitude $\lambda$ is acting on the core-shell system. We use spherical coordinates so that $\theta = \frac{\pi}{2}$ specifies the equator.

Since we are describing a core-shell material, different elastic properties and radii are attributed to the core and to the shell, see Fig. 1. The core (green) is assigned the radius $R_{\mathrm{c}}$, the Young modulus $E_{\mathrm{c}}$, and the Poisson ratio $\nu_{\mathrm{c}}$. The shell (red) is defined by the outer radius $R_{\mathrm{s}}$, the Young modulus $E_{\mathrm{s}}$, and the Poisson ratio $\nu_{\mathrm{s}}$. According to Eq. (3), $\lambda > 0$ marks the amplitude of a line density of force pointing radially outward along the equator of the outer surface of the shell.

The system is characterized by the following five dimensionless parameters. First, the ratio $\lambda/E_{\mathrm{s}}R_{\mathrm{s}}$ of the loading force line density on the surface to the Young modulus of the shell describes the relative strength of the load magnitude and is proportional to the amplitude of deformation. The second parameter is the ratio of Young moduli $E_{\mathrm{c}}/E_{\mathrm{s}}$ of the core to the shell and in addition, the two dimensionless Poisson ratios $\nu_{\mathrm{c}}$ and $\nu_{\mathrm{s}}$ of core and shell, respectively, enter the elasticity theory. The fifth parameter is the size ratio $R_{\mathrm{c}}/R_{\mathrm{s}}$ of the core to the shell.

In spherical coordinates, the position vector $\mathbf{r}$ transforms from the unloaded configuration to the loaded configuration as $\mathbf{r}' = \mathbf{r} + u_r\mathbf{e}_r + u_\theta\mathbf{e}_\theta$, with $u_r$ the radial and $u_\theta$ the polar component of the displacement field. $\mathbf{e}_r$ and $\mathbf{e}_\theta$ denote the radial and polar unit vector, respectively. Due to the special axial symmetry of the problem, the azimuthal component of the displacement field, $u_\phi$, is zero. Concerning the homogeneous Navier-Cauchy equations

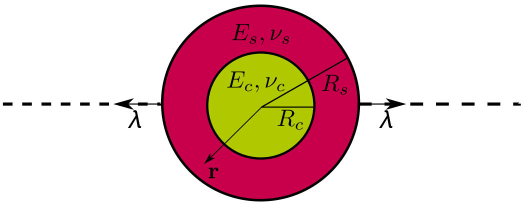

**Fig. 1** Schematic visualisation of the core-shell system, here still in its initial spherical shape for illustration. The core (green) is assigned the radius $R_\mathrm{C}$, the Young modulus $E_\mathrm{C}$, and the Poisson ratio $\nu_\mathrm{C}$. The shell (red) is described by the outer radius $R_\mathrm{S}$, the Young modulus $E_\mathrm{S}$, and the Poisson ratio $\nu_\mathrm{S}$. The system is loaded by exposition to a ring of force line density around the equator of the outer sphere of magnitude $\lambda$.

Eq. (1) and the stress-strain relation Eq. (2) recast in spherical coordinates, where in our case the azimuthal dependence vanishes, see the Supporting Information (SI).

For both core and shell we solve Eq. (1) by separation into a series expansion of the polar dependence in terms of Legendre polynomials $P_n(\cos\theta)$ and associated $r$-dependent prefactors ($r = |\mathbf{r}|$) [51]. We distinguish by superscripts c and s the solutions for core and shell, respectively. More precisely, the solutions [47, 52, 53] of the Navier-Cauchy equations (1) split into a radial component $u_r^{(c)}(\mathbf{r})$ and a polar component $u_\theta^{(c)}(\mathbf{r})$ for the core and take the form

$$u_r^{(c)}(\mathbf{r}) = \sum_{n=0}^{\infty} \left( a_n^{(c)}(n+1)(-2+n+4\nu_c)r^{n+1} + b_n^{(c)} n r^{n-1} \right) P_n(\cos\theta), \tag{4}$$

$$u_\theta^{\mathrm{c}}(\mathbf{r}) = \sum_{n=1}^{\infty} \left( a_n^{(c)}(5+n-4\nu_c)r^{n+1} + b_n^{(c)} r^{n-1} \right) \frac{d}{d\theta} P_n(\cos\theta). \tag{5}$$

The solutions for the shell additionally contain terms inverse in the radial distance from the origin

$$\begin{aligned} u_r^{(s)}(\mathbf{r}) = \sum_{n=0}^{\infty} \Big( & a_n^{(s)}(n+1)(-2+n+4\nu_s)r^{n+1} + b_n^{(s)} n r^{n-1} \\ & + n(3+n-4\nu_s)c_n^{(s)} r^{-n} - (n+1)d_n^{(s)} r^{-(n+2)} \Big) P_n(\cos\theta), \end{aligned} \tag{6}$$

$$\begin{aligned} u_\theta^{(s)}(\mathbf{r}) = \sum_{n=1}^{\infty} \Big( & a_n^{(s)}(5+n-4\nu_s)r^{n+1} + b_n^{(s)} r^{n-1} \\ & -(-4+n+4\nu_s)c_n^{(s)} r^{-n} + d_n^{(s)} r^{-(n+2)} \Big) \frac{d}{d\theta} P_n(\cos\theta). \end{aligned} \tag{7}$$

As boundary conditions, we use that the traction vectors at the interface of core and shell (at radius $R_c$) must be equal

$$\underline{\boldsymbol{\sigma}}^{(c)}(R_c \mathbf{e}_r) \cdot \mathbf{n} = \underline{\boldsymbol{\sigma}}^{(s)}(R_c \mathbf{e}_r) \cdot \mathbf{n}. \tag{8}$$

Requiring strict elastic no-slip coupling, also the deformations at the interface must be equal

$$\mathbf{u}^{(c)}(R_c \mathbf{e}_r) = \mathbf{u}^{(s)}(R_c \mathbf{e}_r). \tag{9}$$

Since the Legendre polynomials form a complete orthogonal set, the Dirac delta function in Eq. (3) can be expanded in Legendre polynomials

$$\delta\left(\theta-\frac{\pi}{2}\right)=\sum_{n=0}^{\infty}\frac{2n+1}{2}P_n\left(\cos\left(\frac{\pi}{2}\right)\right)P_n\left(\cos\theta\right). \tag{10}$$

Due to the assumed mirror symmetry with respect to the equatorial plane, all odd series expansion components in the core and shell solution in Eqs. (4)-(7) vanish. Therefore we can write for the radial displacement

$$u_r^{(i)}\left(\mathbf{r}\right)=u_{r,0}^{(i)}\left(r\right)+u_{r,2}^{(i)}\left(r\right)P_2\left(\cos(\theta)\right)+\cdots \tag{11}$$

with $i=c$ for the core and $i=s$ for the shell, respectively. Here, the first component $u_{r,0}^{(i)}(r)$ describes the overall volume change. We note that this term will vanish for $\nu_i\rightarrow 1/2$ and remains as the only component for $\nu_i\rightarrow -1$. The second component gives the first correction to a spherical shape. A positive prefactor $u_{r,2}^{(i)}(r)$ describes a relative prolate deformation while $u_{r,2}^{(i)}(r)<0$ implies a relative oblate deformation. It is in fact the latter case of an oblate deformation which we expect when the core-shell particle is pulled outwards at the equator $(\lambda>0)$.

The solutions for the displacements of the core and the shell diverge in response to the Dirac delta function at the equator on the surface of the shell, see the boundary condition Eq. (3). Yet, each mode of deformation is only excited to a finite degree by the Dirac delta function, see Eq. (10). Therefore, the second components $u_{r,2}^{(c)}(r)$ and $u_{r,2}^{(s)}(r)$ for the core and the shell remain finite and $u_{r,2}^{(s)}(r)$ is even finite at the surface of the shell. We shall use them as parameters to characterise the relative oblate or prolate deformation of the core and the shell shape.

For convenience, we evaluate these second components at the core and shell radii and normalize them with the corresponding unloaded radii of the core and the shell, respectively. Hence, we use subsequently $u_{r,2}^{(c)}/R_c\equiv u_{r,2}^{(c)}(R_c)/R_c$ and $u_{r,2}^{(s)}/R_s\equiv u_{r,2}^{(s)}(R_s)/R_s$ as dimensionless measures for the shape of the core and the shell.

## 3 Results and Discussion

### 3.1 General Solution and Limiting Behaviour

We first present the solutions for the displacements under the prescribed boundary conditions by providing the core coefficients of the expansions (4) and (5)

$$a_n^{(c)}=\frac{\lambda}{E_{\mathrm{s}}R_{\mathrm{s}}}\frac{2n+1}{2}P_n\left(0\right)\left(\frac{R_{\mathrm{c}}}{R_{\mathrm{s}}}\right)^{-2}R_{\mathrm{s}}^{-n}\left[\left(\frac{E_{\mathrm{c}}}{E_{\mathrm{s}}}\right)\tilde{c}_{01,n}+\tilde{c}_{02,n}\right]\frac{1}{D}, \tag{12}$$

$$b_n^{(c)}=-\frac{\lambda}{E_{\mathrm{s}}R_{\mathrm{s}}}\frac{2n+1}{2}P_n\left(0\right)R_{\mathrm{s}}^{-(n-2)}\left[\left(\frac{E_{\mathrm{c}}}{E_{\mathrm{s}}}\right)\tilde{c}_{03,n}+\tilde{c}_{04,n}\right]\frac{1}{D}, \tag{13}$$

and the shell coefficients of the expansions (6) and (7)

$$a_n^{(s)}=\frac{\lambda}{E_{\mathrm{s}}R_{\mathrm{s}}}\frac{2n+1}{2}P_n\left(0\right)R_{\mathrm{s}}^{-n}$$

$$\times \left[ \left( \frac{E_{\rm c}}{E_{\rm s}} \right)^2 \tilde{c}_{05,n} + \left( \frac{E_{\rm c}}{E_{\rm s}} \right) \tilde{c}_{06,n} + \tilde{c}_{07,n} \right] \frac{1}{D}, \tag{14}$$

$$b_n^{(s)} = -\frac{\lambda}{E_{\rm s} R_{\rm s}} \frac{2n+1}{2} P_n(0)\, R_{\rm s}^{-(n-2)}$$

$$\times \left[ \left( \frac{E_{\rm c}}{E_{\rm s}} \right)^2 \tilde{c}_{08,n} + \left( \frac{E_{\rm c}}{E_{\rm s}} \right) \tilde{c}_{09,n} + \tilde{c}_{10,n} \right] \frac{1}{D}, \tag{15}$$

$$c_n^{(s)} = \frac{\lambda}{E_{\rm s} R_{\rm s}} \frac{2n+1}{2} P_n(0) \left( \frac{R_{\rm c}}{R_{\rm s}} \right)^{n-1} R_{\rm c}^n R_{\rm s}$$

$$\times \left[ \left( \frac{E_{\rm c}}{E_{\rm s}} \right)^2 \tilde{c}_{11,n} + \left( \frac{E_{\rm c}}{E_{\rm s}} \right) \tilde{c}_{12,n} + \tilde{c}_{13,n} \right] \frac{1}{D}, \tag{16}$$

$$d_n^{(s)} = -\frac{\lambda}{E_{\rm s} R_{\rm s}} \frac{2n+1}{2} P_n(0) \left( \frac{R_{\rm c}}{R_{\rm s}} \right)^{n-1} R_{\rm c}^{n+2} R_{\rm s}$$

$$\times \left[ \left( \frac{E_{\rm c}}{E_{\rm s}} \right)^2 \tilde{c}_{14,n} + \left( \frac{E_{\rm c}}{E_{\rm s}} \right) \tilde{c}_{15,n} + \tilde{c}_{16,n} \right] \frac{1}{D}, \tag{17}$$

with

$$D = \left( \frac{E_{\rm c}}{E_{\rm s}} \right)^2 \tilde{c}_{17,n} + \frac{E_{\rm c}}{E_{\rm s}} \tilde{c}_{18,n} + \tilde{c}_{19,n}. \tag{18}$$

The constants $\tilde{c}_{01,n}$ to $\tilde{c}_{19,n}$ are listed in the SI. In the absence of a core, i.e. $R_{\rm c} \to 0$, or in the absence of the shell, i.e. $R_{\rm c} \to R_{\rm s}$, we recover the previous solution for a one-component system as given in Ref. [47]. Also for the special case of $E_{\rm c} = E_{\rm s}$ and $\upsilon_{\rm c} = \upsilon_{\rm s}$ of identical core and shell elasticities, our solution reduces to that of a one-component system.

### 3.2 Relative Deformation of the Shell and the Core

In the following, the degrees of deformation of the core and the shell are investigated for volume conserving conditions ($\nu_c = \nu_s = 1/2$) for both tensile ($\lambda > 0$) and compressive ($\lambda < 0$) situations. Figure 2 shows the relative deformation $u_{r,2}^{(i)}/R_i$ for a tensile (left column) and a compressive (right column) line force density. The relative deformation is plotted for the shell ($i = s$) in a) and b) and for the core ($i = c$) in c) and d) as a function of the ratios of Young moduli $E_c/E_s$. Data are provided for several size ratios $R_c/R_s$ ranging from 0.3 to 1.

The first observation is that the coefficient $u_{r,2}^{(i)}/R_i$ is negative for the tensile case and positive for a compressive situation, corresponding to a relative oblate and prolate deformation. This is a simple consequence of the force load pulling or pushing the equator to the outward or inward direction, respectively.

Second, the absolute magnitude of deformation decreases in both cases with increasing $E_c/E_s$ which is the expected trend if the core is getting harder than the shell (at fixed shell elasticity). For $E_c/E_s \to 0$ we obtain the special case of a hollow sphere. In this limit, the relative deformation of the core and the shell reaches a finite saturation (note the logarithmic scale in Fig. 2). In the opposite limit $E_c/E_s \to \infty$ the core gets rigid, which implies that the displacement of the shell stays finite but the displacement of the core tends to zero. We find a common finite slope of $\pm 1$ for the curves associated with the core for $E_c/E_s \to \infty$ in Fig. 2.

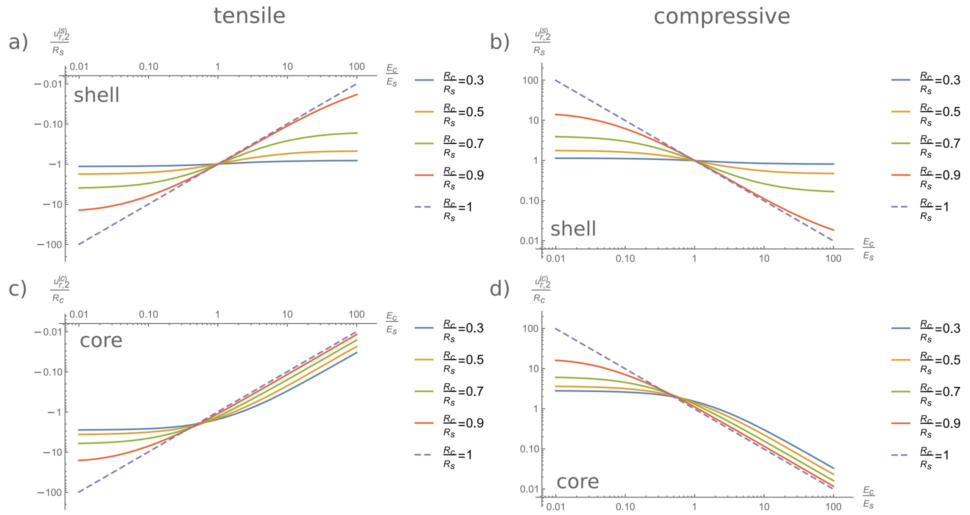

**Fig. 2** Relative deformation $u^{(i)}_{r,2}/R_i$ as a function of the ratio of Young moduli $E_c/E_s$ at different size ratios $R_c/R_s$. Two cases are considered, namely **a**,**c**) tensile (oriented radially outward, $\lambda/(E_s R_s) = 1$) and **b**,**d**) compressive (oriented radially inward, $\lambda/(E_s R_s) = -1$) line force densities. For both cases the relative deformation of the shell ($i = s$) in **a**) and **b**) and the core ($i = c$) in **c**) and **d**) is shown on a double logarithmic scale. Further parameters are $\nu_c = \nu_s = 1/2$. The blue dashed line corresponds to the limit of a one-component system (for $R_c/R_s = 1$).

Moreover, in Fig. 2a all curves intersect in the same point at $E_c = E_s$. At this point the two materials are identical and the size ratio becomes irrelevant for the deformation at the shell surface. The curves of Fig. 2b do not exhibit a common intersection point due to our normalization of the relative deformation with $R_c$ and the fact that the radial deformation is in general not homogeneous along the radius. For increasing $R_c/R_s$, the influence of the core grows and the curves exhibit more sensitivity as a function of $E_c$ for fixed $E_s$.

To complement the picture, Fig. 3 shows the same quantity as in Fig. 2 for the tensile case, namely the relative oblate deformation $u^{(i)}_{r,2}/R_i$, but now as a function of the size ratio $R_c/R_s$ for a) the shell ($i = s$) and b) the core ($i = c$). Curves for several ratios of Young moduli $E_c/E_s$ are displayed. For $E_c = E_s$ (dashed red curves), the resulting effective one-component system features a shell displacement that does not depend on the size ratio of core to shell. Conversely, the plotted core displacement does depend on the size ratio for $E_c = E_s$ because it is normalized by the size of the core. The deformation scaled by $R_c$ in the limit of small core size $R_c \to 0$ (see Fig. 3b) reaches different limits for different ratios of Young moduli although the core becomes vanishingly small. Furthermore, the limit of a hollow sphere system $E_c/E_s \to 0$, is also shown in Fig. 3a) and b).

### 3.3 Deformational Behaviour for Different Poisson Ratios of Core and Shell

We now study the different deformation behaviour for the core and the shell with respect to their Poisson ratios. In particular we explore the elastic response for an auxetic core combined with a regular elastic shell, and vice versa. Such combinations can, at least, be realized in macroscopic elastic model systems, when appropriate materials are chosen. Thus their behaviour is investigated systematically for varying compressibility and auxetic properties. Figure 4 shows the deformational behaviour of the core and the shell as a function of their (in general different) Poisson ratios $\nu_c$ and $\nu_s$. For simplicity we here consider the same

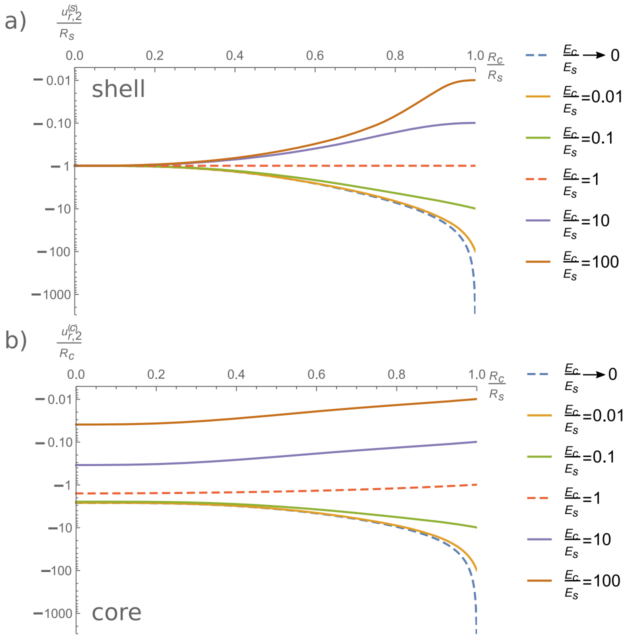

**Fig. 3** Relative oblate deformation $u^{(i)}_{r,2}/R_i$ as a function of the size ratio $R_c/R_s$ for different ratios of Young moduli $E_c/E_s$ for a) the shell ($i = s$) and b) the core ($i = c$) on semi-logarithmic scale. Further parameters are $\nu_c = \nu_s = 1/2$ and $\lambda/(E_s R_s) = 1$. The red ($E_c/E_s = 1$) and blue ($E_c/E_s \to 0$) dashed curves correspond to one-component and hollow sphere systems, respectively.

stiffness of the core and the shell, $E_c = E_s$. Moreover we fix the core size to $R_c = 0.5R_s$ and the load amplitude to $\lambda/(E_s R_s) = 0.1$.

We distinguish between two different states of the displacement: I) the shell is more oblate than the core and II) the core is more oblate than the shell. In order to do so, we use the absolute value of the (here always negative) second coefficient of relative deformation of the shell $\left|u^{(s)}_{r,2}/R_s\right|$ and the core $\left|u^{(c)}_{r,2}/R_c\right|$. For state I) (reddish and greenish in Fig. 4) we have $\left|u^{(s)}_{r,2}/R_s\right| > \left|u^{(c)}_{r,2}/R_c\right|$, while for state II) (greyish in Fig. 4) we have $\left|u^{(s)}_{r,2}/R_s\right| < \left|u^{(c)}_{r,2}/R_c\right|$. See also the two schematic sketches on the top right-hand side of Fig. 4. The transition from I) to II), given by the same relative degree of oblate deformation $\left|u^{(s)}_{r,2}/R_s\right| = \left|u^{(c)}_{r,2}/R_c\right|$, is shown in Fig. 4 by the yellow line separating the two regions. There is a non-monotonic behaviour of this line as a function of $\nu_c$ for an auxetic shell ($\nu_s \approx -0.6$) and a nearly incompressible core.

The different colour codes on the right hand side in Fig. 4 represent the magnitude of the relative oblate deformation of the shell for state I) and of the core for state II). For nine selected points indicated in the $\nu_c\nu_s$-plane we illustrate the corresponding shapes of the core and the shell as given by the components $u^{(c)}_{r,0}$, $u^{(c)}_{r,2}$, $u^{(s)}_{r,0}$ and $u^{(s)}_{r,2}$, respectively, describing the change in volume and relative oblate deformation.

At the origin in the state diagram, where $\nu_c = \nu_s = 0$, the relative oblate deformation of the core and the shell are equal so that the yellow line passes through the origin in Fig. 4. Strictly speaking, this point [and all others on the diagonal from (a) to (d)] describes a one-component system, because there the elastic properties of the core and the shell are identical. We note that in general the yellow line of $\left|u^{(s)}_{r,2}/R_s\right| = \left|u^{(c)}_{r,2}/R_c\right|$ does not coincide with the diagonal of $\nu_c = \nu_s$ in Fig. 4, although we find a one-component material in the latter case. One aspect that contributes to this result is the inhomogeneous stress and strain distribution in the system, resulting from the force density that is concentrated at the equator. Further remarks on these stress and strain distributions are given in Sect. 3.4.

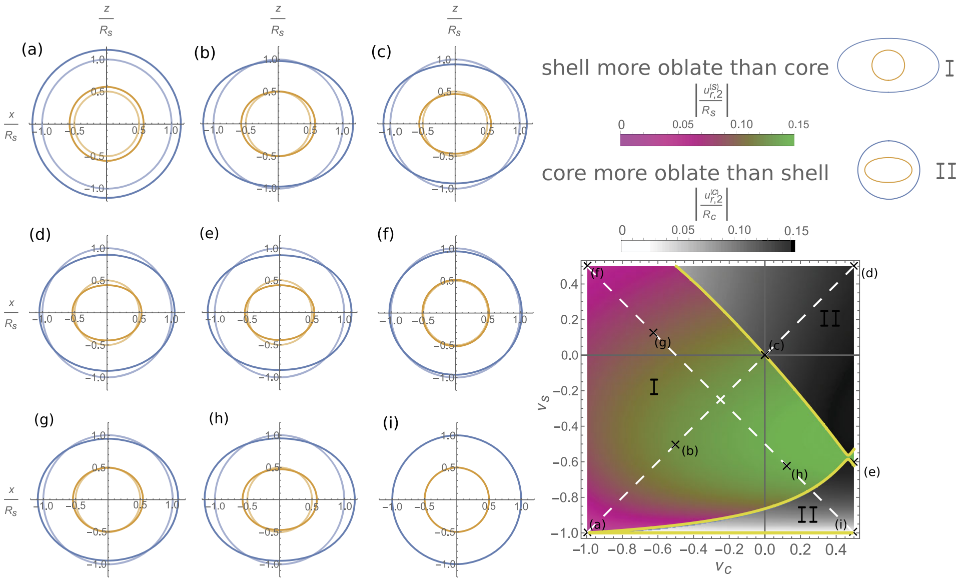

**Fig. 4** Bottom right: State diagram exhibiting two situations I) and II) in the plane spanned by the two Poisson ratios of the core $\nu_c$ and the shell $\nu_s$ at fixed $E_c = E_s$, $R_c = 0.5R_s$ and $\lambda/(E_s R_s) = 0.1$. In I), corresponding to the reddish and greenish region, the relative oblate deformation of the shell is larger in magnitude than that of the core, see schematic representation on the top right. Here we plot in region I of the state diagram $\left|u_{r,2}^{(s)}/R_s\right|$ as colour-coded on the top right. Conversely, in II), corresponding to the greyish region in the state diagram, the relative oblate deformation of the core is larger in magnitude than that of the shell. Here we plot in region II of the state diagram $\left|u_{r,2}^{(c)}/R_c\right|$ as colour-coded on the top right. The two states I) and II) are separated by yellow lines, which represent the same relative degree of oblate deformation. Effectively, a one-component system is given by the (white dashed) diagonal from (**a**) to (**d**). Furthermore, for nine parameter combinations indicated for various points (**a**)-(**i**) in the state diagram, the corresponding elliptical shapes of core and shell are shown on the left with the light curves as a reference to the undeformed system.

Clearly, for the parameter combinations on the yellow line separating regions I) and II), the relative oblate deformations of core and shell are equal, as seen in Fig. 4 (a), (c), and (i) $\left(\left|u_{r,2}^{(s)}/R_s\right| = \left|u_{r,2}^{(c)}/R_c\right|\right)$. In the special cases of (a) and (i) we recover spherical shapes of core and shell, even if the volume has changed $\left(\left|u_{r,2}^{(c)}/R_c\right| = \left|u_{r,2}^{(s)}/R_s\right| = 0\right)$. We observe that $\left|u_{r,2}^{(c)}/R_c\right|$ and $\left|u_{r,2}^{(s)}/R_s\right|$ in the state diagram are continuous when varying the Poisson ratios, even in the vicinity of (e). For $\nu_s = -1$, we found that the shell determines the considered modes $u_{r,2}^{(c)}$ and $u_{r,2}^{(s)}$, forcing them to vanish. In conclusion, different Poisson ratios can largely tune the behaviour of the core-shell structure under external loading.

### 3.4 Internal Stress Field

We now provide explicit data for the internal stress field. For quasi volume conserving conditions ($\nu_c = \nu_s = 0.4999$), a size ratio of $R_c/R_s = 0.5$, and an amplitude of $\lambda/(E_s R_s) = 0.1$ of the force line density, loaded configurations of the core-shell system for three different ratios of Young moduli $E_c/E_s$ are shown in Fig. 5.

The loaded configurations are colour coded for the components of the (symmetric) stress tensor, defined by $\underline{\sigma}^{(\mathrm{i})} = \sigma_{rr}^{(\mathrm{i})}\mathbf{e}_r \otimes \mathbf{e}_r + \sigma_{r\theta}^{(\mathrm{i})}(\mathbf{e}_\theta \otimes \mathbf{e}_r + \mathbf{e}_r \otimes \mathbf{e}_\theta) + \sigma_{\theta\theta}^{(\mathrm{i})}\mathbf{e}_\theta \otimes \mathbf{e}_\theta$, for the core

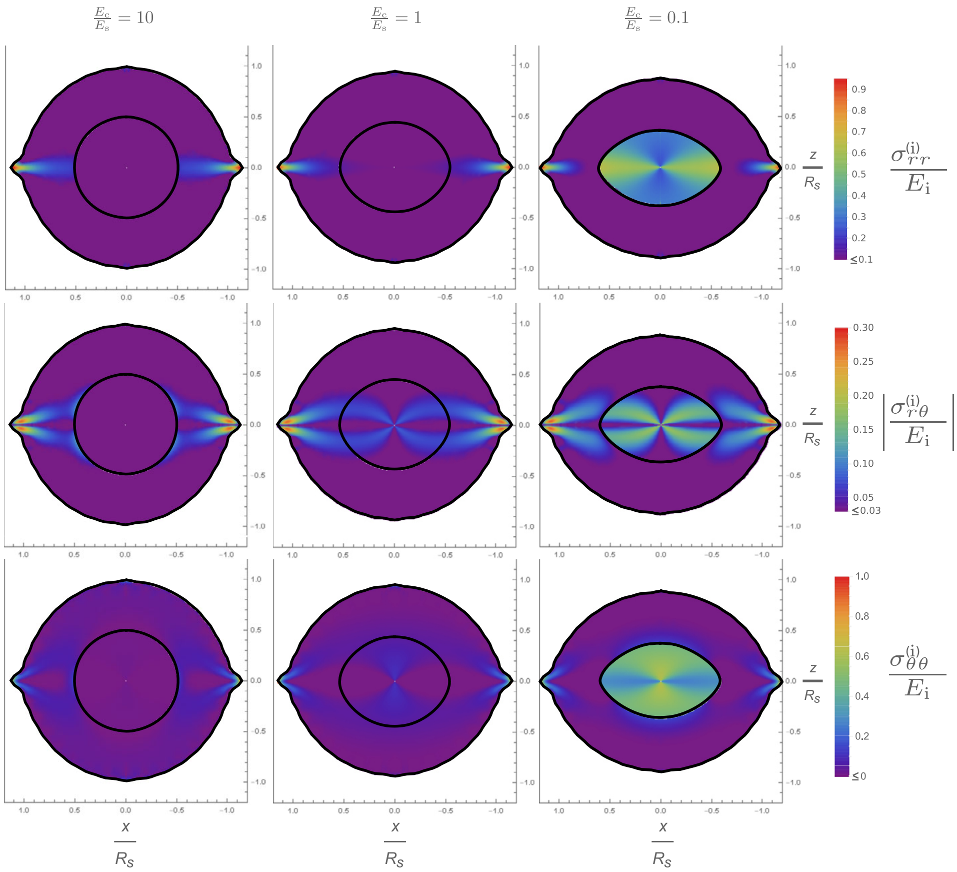

**Fig. 5** Loaded configurations of the core-shell system at fixed $\nu_c = \nu_s = 0.4999$, $R_c = 0.5R_s$, and $\lambda/(E_s R_s) = 0.1$. The colour code reflects the three scaled components of the symmetric stress tensor $\sigma^{(i)}_{rr}/E_i$, $|\sigma^{(i)}_{r\theta}|/E_i$ and $\sigma^{(i)}_{\theta\theta}/E_i$ for the core $(i = c)$ and the shell $(i = s)$. Three different ratios of Young moduli $E_c/E_s$ each are shown for the three components. The core and shell boundaries are indicated by black lines. To achieve a better resolution, only the absolute value of $\sigma^{(\mathrm{i})}_{r\theta}/E_\mathrm{i}$ is shown. By symmetry, this tensor component changes sign in the different quadrants of the $xz$-plane.

$(i = c)$ and the shell $(i = s)$. The components of the stress tensor are scaled by the respective $E_i$ in the core $(i = c)$ and in the shell $(i = s)$. Results for the deformations and associated components of stress are calculated from Eqs. (2) and (4)-(7), where the infinite series are truncated at $n = 32$.

For all configurations, all components of the stress tensor are of the greatest extent around the equatorial line of loading along the shell surface. Clearly, the system there experiences a displacement in positive radial (outward) direction. Due to the quasi-incompressibility of both shell and core, a strong degree of inverted displacement results at the poles.

For $E_c \ll E_s$, the soft core deforms more easily than the surrounding harder shell and experiences a higher amount of scaled stress. The scaled stress of the quasi-incompressible shell is transferred from the equator towards the inside by the bulk elasticity of the shell (see the right column in Fig. 5). Conversely, for $E_c \gg E_s$, there is hardly any influence of the deformation of the shell on the core for the scaled stresses (see the left column in Fig. 5).

For comparison, the center column in Fig. 5 shows a loaded one-component system $E_c = E_s$ and the corresponding scaled components of stress.

## 4 Conclusions

We have analysed in detail the deformational response of an elastic core-shell system to a radially oriented force line density acting along the outside equatorial line. Natural extensions of our considerations include the following.

First, the axially symmetric situation that we addressed could be generalized to systems exposed to line densities that are modulated along the circumference. Moreover, the effect of surface force densities applied in patches or distributed over the whole surface area could be analysed, instead of pure force line densities. In a further step, the imposed distortions may not only be imposed from outside, but could additionally result from internal active or actuation centers. Obvious candidates for corresponding actuatable cores are given by magnetic gels [54, 55]. For these types of systems, magnetically induced deformations have already been analysed by linear elasticity theory in the case of one-component elastic spheres [56–58].

The considered geometry of loading can effectively be realised in experiments on the mesoscale by exposing core-shell microgel particles to the interface between two immiscible fluids acting on the elastic system [32, 33]. There, interfacial tension radially pulls on the equatorial circumference along the common contact line in a symmetric setup. Yet, our description can be applied to any system on any scale that can be characterized by continuum elasticity theory. For example, macroscopic elastic core-shell spheres could be generated as toy models using soft transparent elastic shells on an elastic core. The line of loading force could then simply be imposed by tying a cord around the equator of these macroscopic core-shell spheres and tightening it. In this setup, the direction of the force is inverted as well. However, this in our evaluation simply means that all directions of displacement are inverted. Such macroscopic approaches may support the involvement of auxetic components [37–42]. Depending on the materials at hand, this strategy may facilitate the experimental confirmation of our results, possibly by direct visual inspection.

**Supplementary Information** The online version contains supplementary material available at https://doi.org/10.1007/s10659-022-09897-1.

**Acknowledgements** L.F. and A.M.M. thank the Deutsche Forschungsgemeinschaft (DFG) for support through the SPP 1681 on magnetic hybrid materials, grant no. ME 3571/2-3, and for support through the Heisenberg Grant ME 3571/4-1 (A.M.M.). H.L. acknowledges funding from the Deutsche Forschungsgemeinschaft (DFG) under grant number LO 418/22-1.

**Funding Note** Open Access funding enabled and organized by Projekt DEAL.

## References

1. Jacobs, J.: The Earth's Core. Int. Geophys. **20**, 213–237 (1975)
2. Caruso, F.: Adv. Mater. **13**, 11–22 (2001)
3. Schärtl, W.: Nanoscale **2**, 829–843 (2010)
4. Pusey, P.N.: In: Hansen, J.P., Levesque, D., Zinn-Justin, J. (eds.) Liquids, Freezing and the Glass Transition. North-Holland, Amsterdam (1991)
5. Lekkerkerker, H.N., Tuinier, R.: In: Colloids and the Depletion Interaction, pp. 57–108. Springer, Dordrecht (2011)
6. Royall, C.P., Poon, W.C., Weeks, E.R.: Soft Matter **9**, 17–27 (2013)
7. Förster, S., Abetz, V., Müller, A.H.: In: Polyelectrolytes with Defined Molecular Architecture II. Advances in Polymer Science, vol. 166, pp. 173–210. Springer, Berlin (2004)
8. Rey, M., Fernandez-Rodriguez, M.A., Karg, M., Isa, L., Vogel, N.: Acc. Chem. Res. **53**, 414–424 (2020)
9. Rey, M., Hou, X., Tang, J.S.J., Vogel, N.: Soft Matter **13**, 8717–8727 (2017)
10. Plamper, F.A., Richtering, W.: Acc. Chem. Res. **50**, 131–140 (2017)
11. Yang, Z., Yang, L., Zhang, Z., Wu, N., Xie, J., Cao, W.: Colloids Surf. A, Physicochem. Eng. Asp. **312**, 113–117 (2008)
12. Liu, N., Zhao, S., Yang, Z., Liu, B.: ACS Appl. Mater. Interfaces **11**, 47008–47014 (2019)
13. Kataoka, K., Harada, A., Nagasaki, Y.: Adv. Drug Deliv. Rev. **47**, 113–131 (2001)
14. Bonacucina, G., Cespi, M., Misici-Falzi, M., Palmieri, G.F.: J. Pharm. Sci. **98**, 1–42 (2009)
15. Motornov, M., Roiter, Y., Tokarev, I., Minko, S.: Prog. Polym. Sci. **35**, 174–211 (2010)
16. Förster, S., Plantenberg, T.: Angew. Chem., Int. Ed. **41**, 688–714 (2002)
17. Heyes, D., Aston, P.: J. Chem. Phys. **97**, 5738–5748 (1992)
18. Bolhuis, P., Frenkel, D.: J. Phys. Condens. Matter **9**, 381–387 (1997)
19. Denton, A., Löwen, H.: J. Phys. Condens. Matter **9**, L1 (1997)
20. Jagla, E.: Phys. Rev. E **58**, 1478–1486 (1998)
21. Malescio, G., Pellicane, G.: Nat. Mater. **2**, 97–100 (2003)
22. Pauschenwein, G.J., Kahl, G.: J. Chem. Phys. **129**, 174107 (2008)
23. Yuste, S.B., Santos, A., López de Haro, M.: Mol. Phys. **109**, 987–995 (2011)
24. Norizoe, Y., Kawakatsu, T.: J. Chem. Phys. **137**, 024904 (2012)
25. Pattabhiraman, H., Gantapara, A.P., Dijkstra, M.: J. Chem. Phys. **143**, 164905 (2015)
26. Gabriëlse, A., Löwen, H., Smallenburg, F.: Materials **10**, 1280 (2017)
27. Somerville, W.R., Law, A.D., Rey, M., Vogel, N., Archer, A.J., Buzza, D.M.A.: Soft Matter **16**, 3564–3573 (2020)
28. Ivlev, A., Morfill, G., Löwen, H., Royall, C.P.: Complex Plasmas and Colloidal Dispersions: Particle-resolved Studies of Classical Liquids and Solids, vol. 5. World Scientific, Singapore (2012)
29. Gasser, U.: J. Phys. Condens. Matter **21**, 203101 (2009)
30. Karg, M., Pich, A., Hellweg, T., Hoare, T., Lyon, L.A., Crassous, J., Suzuki, D., Gumerov, R.A., Schneider, S., Potemkin, I.I., Richtering, W.: Langmuir **35**, 6231–6255 (2019)
31. Bresme, F., Oettel, M.: J. Phys. Condens. Matter **19**, 413101 (2007)
32. Harrer, J., Rey, M., Ciarella, S., Löwen, H., Janssen, L.M.C., Vogel, N.: Langmuir **35**, 10512–10521 (2019)
33. Kolker, J., Harrer, J., Ciarella, S., Rey, M., Ickler, M., Janssen, L.M.C., Vogel, N., Löwen, H.: Soft Matter **17**, 5581–5589 (2021)
34. Rauh, A., Rey, M., Barbera, L., Zanini, M., Karg, M., Isa, L.: Soft Matter **13**, 158–169 (2017)
35. Vasudevan, S.A., Rauh, A., Kroger, M., Karg, M., Isa, L.: Langmuir **34**, 15370–15382 (2018)
36. Huang, S., Gawlitza, K., von Klitzing, R., Gilson, L., Nowak, J., Odenbach, S., Steffen, W., Auernhammer, G.K.: Langmuir **32**, 712–722 (2016)
37. Huang, C., Chen, L.: Adv. Mater. **28**, 8079–8096 (2016)
38. Ren, X., Das, R., Tran, P., Ngo, T.D., Xie, Y.M.: Smart Mater. Struct. **27**, 023001 (2018)
39. Scarpa, F., Bullough, W., Lumley, P.: Proc. Inst. Mech. Eng., Part C, J. Mech. Eng. Sci. **218**, 241–244 (2004)
40. Lakes, R.: Science **235**, 1038–1041 (1987)
41. Chan, N., Evans, K.: J. Mater. Sci. **32**, 5945–5953 (1997)
42. Caddock, B., Evans, K.: J. Phys. D, Appl. Phys. **22**, 1877–1882 (1989)
43. Babaee, S., Shim, J., Weaver, J.C., Chen, E.R., Patel, N., Bertoldi, K.: Adv. Mater. **25**, 5044–5049 (2013)
44. Jiang, Y., Li, Y.: Sci. Rep. **8**, 2397 (2018)
45. Kim, Y., Yuk, H., Zhao, R., Chester, S.A., Zhao, X.: Nature **558**, 274–279 (2018)
46. Evans, K.E.: Endeavour **15**, 170–174 (1991)
47. Style, R.W., Isa, L., Dufresne, E.R.: Soft Matter **11**, 7412–7419 (2015)
48. Hegemann, J., Boltz, H.-H., Kierfeld, J.: Soft Matter **14**, 5665–5685 (2018)

49. Cauchy, A.L.B.: Exercices de mathématiques. De Bure Frères, vol. 3. (1828)
50. Landau, L., Lifshitz, E.: Theory of Elasticity, 3rd edn. Butterworth-Heinemann, Oxford (1986)
51. Love, A.E.H.: A Treatise on the Mathematical Theory of Elasticity. Cambridge University Press, Cambridge (1927)
52. Duan, H.L., Wang, J., Huang, Z.P., Karihaloo, B.L.: Proc. R. Soc. A, Math. Phys. Eng. Sci. **461**, 3335–3353 (2005)
53. Yi, X., Duan, H.L., Karihaloo, B.L., Wang, J.: Arch. Mech. **59**, 259–281 (2007)
54. Weeber, R., Hermes, M., Schmidt, A.M., Holm, C.: J. Phys. Condens. Matter **30**, 063002 (2018)
55. Odenbach, S.: Arch. Appl. Mech. **86**, 269–279 (2016)
56. Fischer, L., Menzel, A.M.: J. Chem. Phys. **151**, 114906 (2019)
57. Fischer, L., Menzel, A.M.: Phys. Rev. Res. **2**, 023383 (2020)
58. Fischer, L., Menzel, A.M.: Smart Mater. Struct. **30**, 014003 (2021)

# Supporting Information: Elastic deformations of spherical core-shell systems under an equatorial load

Jannis Kolker,[*,†] Lukas Fischer,[*,‡] Andreas M. Menzel,[‡] and Hartmut Löwen[†]

†*Institut für Theoretische Physik II: Weiche Materie, Heinrich-Heine-Universität Düsseldorf, D-40225 Düsseldorf, Germany*

‡*Institut für Physik, Otto-von-Guericke-Universität Magdeburg, Universitätsplatz 2, D-39106 Magdeburg, Germany*

E-mail: jannis.kolker@hhu.de; lukas.fischer@ovgu.de

In this supporting information, the Navier-Cauchy equations and stress-strain relations Eqs. (1) and (2) in the main text, respectively, are presented in spherical coordinates for the problem under investigation. The further dependences of the coefficients $a_n^{(c)}$, $b_n^{(c)}$, $a_n^{(s)}$, $b_n^{(s)}$, $c_n^{(s)}$, $d_n^{(s)}$ on the dimensionless parameters $\frac{\lambda}{E_\mathrm{s}R_\mathrm{s}}$, $\frac{E_\mathrm{c}}{E_\mathrm{s}}$, $\frac{R_\mathrm{c}}{R_\mathrm{s}}$, $\nu_\mathrm{c}$, $\nu_\mathrm{s}$ and on the index $n$ are listed in a two-step order. First, the dependence of the coefficients on the amplitude of the deformation $\frac{\lambda}{E_\mathrm{s}R_\mathrm{s}}$, the ratio of the Young moduli $\frac{E_\mathrm{c}}{E_\mathrm{s}}$ and the ratio of the radii $\frac{R_\mathrm{c}}{R_\mathrm{s}}$ is shown and in the second step the dependence on the index $n$ as well as on the Poisson ratios for core $\nu_\mathrm{c}$ and shell $\nu_\mathrm{s}$ is emphasised. At last the asymptotic behaviour for $n \to \infty$ is analysed for the Legendre polynomials and the general rescaled solutions for the radial component of the displacement field for the core and the shell.

## Navier-Cauchy equations and stress-strain relations in spherical coordinates

Due to the special axial symmetry of the problem, the azimuthal component $u_\phi$ of the displacement field $\mathbf{u}(\mathbf{r})$ is zero and any $\phi$-dependence vanishes. Therefore, the displacement field can be written as $\mathbf{u}(\mathbf{r}) = u_r(r,\theta)\mathbf{e}_r + u_\theta(r,\theta)\mathbf{e}_\theta$, where $\mathbf{e}_r$ and $\mathbf{e}_\theta$ denote the radial and polar unit vectors, respectively. Then the homogeneous Navier-Cauchy equations, Eq. (1) in the main text, in spherical coordinates for the problem under investigation become

$$\begin{aligned} &2(1-\nu)\left(\frac{\partial}{\partial r}\left(\frac{1}{r^2}\frac{\partial}{\partial r}\left(r^2 u_r(r,\theta)\right)\right) + \frac{1}{\sin\theta}\frac{\partial}{\partial r}\left(\frac{1}{r}\frac{\partial}{\partial \theta}\left(\sin\theta u_\theta(r,\theta)\right)\right)\right) \\ &\quad -(1-2\nu)\left(\frac{1}{r^2\sin\theta}\frac{\partial}{\partial\theta}\left(\sin\theta\left(\frac{\partial}{\partial r}\left(r u_\theta(r,\theta)\right) - \frac{\partial}{\partial\theta}u_r(r,\theta)\right)\right)\right) = 0 \qquad (1) \end{aligned}$$

for the radial direction and

$$\begin{aligned}2(1-\nu)\left(\frac{1}{r^3}\frac{\partial}{\partial\theta}\frac{\partial}{\partial r}\left(r^2 u_r\left(r,\theta\right)\right)+\frac{1}{r^2}\frac{\partial}{\partial\theta}\left(\frac{1}{\sin\theta}\frac{\partial}{\partial\theta}\left(\sin\theta u_\theta\left(r,\theta\right)\right)\right)\right)&\\ -(1-2\nu)\left(-\frac{1}{r}\frac{\partial}{\partial r}\left(\frac{\partial}{\partial r}\left(r u_\theta\left(r,\theta\right)\right)-\frac{\partial}{\partial\theta}u_r\left(r,\theta\right)\right)\right)=0&\qquad(2)\end{aligned}$$

for the polar direction. The nontrivial components of the stress-strain relation, Eq. (2) in the main text, in spherical coordinates for the underlying problem read

$$\sigma_{rr}(r,\theta)=\frac{E}{1+\nu}\left(\varepsilon_{rr}(r,\theta)+\frac{\nu}{1-2\nu}\left(\varepsilon_{rr}(r,\theta)+\varepsilon_{\theta\theta}(r,\theta)\right)\right), \qquad (3)$$

$$\sigma_{r\theta}(r,\theta)=\frac{E}{1+\nu}\varepsilon_{r\theta}(r,\theta), \qquad (4)$$

$$\sigma_{\theta\theta}(r,\theta)=\frac{E}{1+\nu}\left(\varepsilon_{\theta\theta}(r,\theta)+\frac{\nu}{1-2\nu}\left(\varepsilon_{rr}(r,\theta)+\varepsilon_{\theta\theta}(r,\theta)\right)\right). \qquad (5)$$

Here, in spherical coordinates, we inserted for the symmetric Cauchy stress tensor $\underline{\boldsymbol{\sigma}}\left(\mathbf{r}\right)=\sigma_{rr}(r,\theta)\mathbf{e}_r\otimes\mathbf{e}_r+\sigma_{r\theta}(r,\theta)\left(\mathbf{e}_\theta\otimes\mathbf{e}_r+\mathbf{e}_r\otimes\mathbf{e}_\theta\right)+\sigma_{\theta\theta}(r,\theta)\mathbf{e}_\theta\otimes\mathbf{e}_\theta$ and for the strain tensor $\underline{\boldsymbol{\varepsilon}}\left(\mathbf{r}\right)=\varepsilon_{rr}(r,\theta)\mathbf{e}_r\otimes\mathbf{e}_r+\varepsilon_{r\theta}(r,\theta)\left(\mathbf{e}_\theta\otimes\mathbf{e}_r+\mathbf{e}_r\otimes\mathbf{e}_\theta\right)+\varepsilon_{\theta\theta}(r,\theta)\mathbf{e}_\theta\otimes\mathbf{e}_\theta$, where $\otimes$ denotes the dyadic product.

## Dependence of the coefficients $a_n^{(c)}, b_n^{(c)}, a_n^{(s)}, b_n^{(s)}, c_n^{(s)}, d_n^{(s)}$ on the amplitude of deformation $\frac{\lambda}{E_\mathbf{s}R_\mathbf{s}}$, the ratio of Young moduli $\frac{E_\mathbf{c}}{E_\mathbf{s}}$ and the ratio of radii $\frac{R_\mathbf{c}}{R_\mathbf{s}}$

The coefficients $a_n^{(c)}, b_n^{(c)}, a_n^{(s)}, b_n^{(s)}, c_n^{(s)}, d_n^{(s)}$ with $n\geq 0$ are listed and their dependence on the amplitude of deformation $\frac{\lambda}{E_\mathrm{s}R_\mathrm{s}}$, the ratio of Young moduli $\frac{E_\mathrm{c}}{E_\mathrm{s}}$ and the ratio of radii $\frac{R_\mathrm{c}}{R_\mathrm{s}}$ is highlighted. The expressions are found from the solutions of the relative deformation

$\frac{\mathbf{u}^{(c)}(R_\mathrm{c}\mathbf{e}_r)}{R_\mathrm{c}}$ and $\frac{\mathbf{u}^{(s)}(R_\mathrm{s}\mathbf{e}_r)}{R_\mathrm{s}}$, respectively:

$$\frac{a_n^{(c)}}{R_\mathrm{c}} R_\mathrm{c}^{n+1} = \frac{\lambda}{E_\mathrm{s} R_\mathrm{s}} \frac{2n+1}{2} P_n(0) \left(\frac{R_\mathrm{c}}{R_\mathrm{s}}\right)^{(n-2)} \left[\left(\frac{E_\mathrm{c}}{E_\mathrm{s}}\right) \tilde{c}_{01,n} + \tilde{c}_{02,n}\right] \frac{1}{D},$$

$$\frac{b_n^{(c)}}{R_\mathrm{c}} R_\mathrm{c}^{n-1} = -\frac{\lambda}{E_\mathrm{s} R_\mathrm{s}} \frac{2n+1}{2} P_n(0) \left(\frac{R_\mathrm{c}}{R_\mathrm{s}}\right)^{(n-2)} \left[\left(\frac{E_\mathrm{c}}{E_\mathrm{s}}\right) \tilde{c}_{03,n} + \tilde{c}_{04,n}\right] \frac{1}{D},$$

$$\begin{aligned}
\frac{a_n^{(s)}}{R_\mathrm{s}} R_\mathrm{s}^{n+1} &= \frac{\lambda}{E_\mathrm{s} R_\mathrm{s}} \frac{2n+1}{2} P_n(0) \left[\left(\frac{E_\mathrm{c}}{E_\mathrm{s}}\right)^2 \tilde{c}_{05,n} + \left(\frac{E_\mathrm{c}}{E_\mathrm{s}}\right) \tilde{c}_{06,n} + \tilde{c}_{07,n}\right] \frac{1}{D}, \\
\frac{b_n^{(s)}}{R_\mathrm{s}} R_\mathrm{s}^{n-1} &= -\frac{\lambda}{E_\mathrm{s} R_\mathrm{s}} \frac{2n+1}{2} P_n(0) \left[\left(\frac{E_\mathrm{c}}{E_\mathrm{s}}\right)^2 \tilde{c}_{08,n} + \left(\frac{E_\mathrm{c}}{E_\mathrm{s}}\right) \tilde{c}_{09,n} + \tilde{c}_{10,n}\right] \frac{1}{D}, \\
\frac{c_n^{(s)}}{R_\mathrm{s}} R_\mathrm{s}^{-n} &= \frac{\lambda}{E_\mathrm{s} R_\mathrm{s}} \frac{2n+1}{2} P_n(0) \left(\frac{R_\mathrm{c}}{R_\mathrm{s}}\right)^{(2n-1)} \left[\left(\frac{E_\mathrm{c}}{E_\mathrm{s}}\right)^2 \tilde{c}_{11,n} + \left(\frac{E_\mathrm{c}}{E_\mathrm{s}}\right) \tilde{c}_{12,n} + \tilde{c}_{13,n}\right] \frac{1}{D}, \\
\frac{d_n^{(s)}}{R_\mathrm{s}} R_\mathrm{s}^{-(n+2)} &= -\frac{\lambda}{E_\mathrm{s} R_\mathrm{s}} \frac{2n+1}{2} P_n(0) \left(\frac{R_\mathrm{c}}{R_\mathrm{s}}\right)^{(2n+1)} \left[\left(\frac{E_\mathrm{c}}{E_\mathrm{s}}\right)^2 \tilde{c}_{14,n} + \left(\frac{E_\mathrm{c}}{E_\mathrm{s}}\right) \tilde{c}_{15,n} + \tilde{c}_{16,n}\right] \frac{1}{D},
\end{aligned}$$

where

$$D = \left(\frac{E_\mathrm{c}}{E_\mathrm{s}}\right)^2 \tilde{c}_{17,n} + \frac{E_\mathrm{c}}{E_\mathrm{s}} \tilde{c}_{18,n} + \tilde{c}_{19,n}. \tag{6}$$

The constants $\tilde{c}_{01,n}$ to $\tilde{c}_{19,n}$ are given below with their dependence on the ratio of radii $\frac{R_\mathrm{c}}{R_\mathrm{s}}$:

$$\begin{aligned}
\tilde{c}_{01,n} =& c_{01,n} + c_{02,n}\left(\frac{R_\mathrm{c}}{R_\mathrm{s}}\right)^2 + c_{03,n}\left(\frac{R_\mathrm{c}}{R_\mathrm{s}}\right)^{(2n+1)} + c_{04,n}\left(\frac{R_\mathrm{c}}{R_\mathrm{s}}\right)^{(2n+3)}, \\
\tilde{c}_{02,n} =& c_{05,n} + c_{06,n}\left(\frac{R_\mathrm{c}}{R_\mathrm{s}}\right)^2 + c_{07,n}\left(\frac{R_\mathrm{c}}{R_\mathrm{s}}\right)^{(2n+1)} + c_{08,n}\left(\frac{R_\mathrm{c}}{R_\mathrm{s}}\right)^{(2n+3)}, \\
\tilde{c}_{03,n} =& c_{09,n} + c_{10,n}\left(\frac{R_\mathrm{c}}{R_\mathrm{s}}\right)^2 + c_{11,n}\left(\frac{R_\mathrm{c}}{R_\mathrm{c}}\right)^{(2n+1)} + c_{12,n}\left(\frac{R_\mathrm{c}}{R_\mathrm{s}}\right)^{(2n+3)}, \\
\tilde{c}_{04,n} =& c_{13,n} + c_{14,n}\left(\frac{R_\mathrm{c}}{R_\mathrm{s}}\right)^2 + c_{15,n}\left(\frac{R_\mathrm{c}}{R_\mathrm{s}}\right)^{(2n+1)} + c_{16,n}\left(\frac{R_\mathrm{c}}{R_\mathrm{s}}\right)^{(2n+3)}, \\
\tilde{c}_{05,n} =& c_{17,n} + c_{18,n}\left(\frac{R_\mathrm{c}}{R_\mathrm{s}}\right)^{(2n-1)} + c_{19,n}\left(\frac{R_\mathrm{c}}{R_\mathrm{s}}\right)^{(2n+1)}, \\
\tilde{c}_{06,n} =& c_{20,n} + c_{21,n}\left(\frac{R_\mathrm{c}}{R_\mathrm{s}}\right)^{(2n-1)} + c_{22,n}\left(\frac{R_\mathrm{c}}{R_\mathrm{s}}\right)^{(2n+1)}, \\
\tilde{c}_{07,n} =& c_{23,n} + c_{24,n}\left(\frac{R_\mathrm{c}}{R_\mathrm{s}}\right)^{(2n-1)} + c_{25,n}\left(\frac{R_\mathrm{c}}{R_\mathrm{s}}\right)^{(2n+1)}, \\
\tilde{c}_{08,n} =& c_{26,n} + c_{27,n}\left(\frac{R_\mathrm{c}}{R_\mathrm{s}}\right)^{(2n+1)} + c_{28,n}\left(\frac{R_\mathrm{c}}{R_\mathrm{s}}\right)^{(2n+3)}, \\
\tilde{c}_{09,n} =& c_{29,n} + c_{30,n}\left(\frac{R_\mathrm{c}}{R_\mathrm{s}}\right)^{(2n+1)} + c_{31,n}\left(\frac{R_\mathrm{c}}{R_\mathrm{s}}\right)^{(2n+3)}, \\
\tilde{c}_{10,n} =& c_{32,n} + c_{33,n}\left(\frac{R_\mathrm{c}}{R_\mathrm{s}}\right)^{(2n+1)} + c_{34,n}\left(\frac{R_\mathrm{c}}{R_\mathrm{s}}\right)^{(2n+3)},
\end{aligned}$$

$$
\begin{aligned}
\tilde{c}_{11,n} =& c_{35,n} + c_{36,n}\left(\frac{R_\mathrm{c}}{R_\mathrm{s}}\right)^2 + c_{37,n}\left(\frac{R_\mathrm{c}}{R_\mathrm{s}}\right)^{(2n+3)},\\
\tilde{c}_{12,n} =& c_{38,n} + c_{39,n}\left(\frac{R_\mathrm{c}}{R_\mathrm{s}}\right)^2 + c_{40,n}\left(\frac{R_\mathrm{c}}{R_\mathrm{s}}\right)^{(2n+3)},\\
\tilde{c}_{13,n} =& c_{41,n} + c_{42,n}\left(\frac{R_\mathrm{c}}{R_\mathrm{s}}\right)^2 + c_{43,n}\left(\frac{R_\mathrm{c}}{R_\mathrm{s}}\right)^{(2n+3)},\\
\tilde{c}_{14,n} =& c_{44,n} + c_{45,n}\left(\frac{R_\mathrm{c}}{R_\mathrm{s}}\right)^2 + c_{46,n}\left(\frac{R_\mathrm{c}}{R_\mathrm{s}}\right)^{(2n+1)},\\
\tilde{c}_{15,n} =& c_{47,n} + c_{48,n}\left(\frac{R_\mathrm{c}}{R_\mathrm{s}}\right)^2 + c_{49,n}\left(\frac{R_\mathrm{c}}{R_\mathrm{s}}\right)^{(2n+1)},\\
\tilde{c}_{16,n} =& c_{50,n} + c_{51,n}\left(\frac{R_\mathrm{c}}{R_\mathrm{s}}\right)^2 + c_{52,n}\left(\frac{R_\mathrm{c}}{R_\mathrm{s}}\right)^{(2n+1)},\\
\tilde{c}_{17,n} =& c_{53,n} + c_{54,n}\left(\frac{R_\mathrm{c}}{R_\mathrm{s}}\right)^{(2n-1)} + c_{55,n}\left(\frac{R_\mathrm{c}}{R_\mathrm{s}}\right)^{(2n+1)} + c_{56,n}\left(\frac{R_\mathrm{c}}{R_\mathrm{s}}\right)^{(2n+3)} + c_{57,n}\left(\frac{R_\mathrm{c}}{R_\mathrm{s}}\right)^{(4n+2)},\\
\tilde{c}_{18,n} =& c_{58,n} + c_{59,n}\left(\frac{R_\mathrm{c}}{R_\mathrm{s}}\right)^{(2n-1)} + c_{60,n}\left(\frac{R_\mathrm{c}}{R_\mathrm{s}}\right)^{(2n+1)} + c_{61,n}\left(\frac{R_\mathrm{c}}{R_\mathrm{s}}\right)^{(2n+3)} + c_{62,n}\left(\frac{R_\mathrm{c}}{R_\mathrm{s}}\right)^{(4n+2)},\\
\tilde{c}_{19,n} =& c_{63,n} + c_{64,n}\left(\frac{R_\mathrm{c}}{R_\mathrm{s}}\right)^{(2n-1)} + c_{65,n}\left(\frac{R_\mathrm{c}}{R_\mathrm{s}}\right)^{(2n+1)} + c_{66,n}\left(\frac{R_\mathrm{c}}{R_\mathrm{s}}\right)^{(2n+3)} + c_{67,n}\left(\frac{R_\mathrm{c}}{R_\mathrm{s}}\right)^{(4n+2)}.
\end{aligned}
$$

## Dependence of the constants $c_{01,n}$ to $c_{67,n}$ on the index $n$, the Poisson ratio of the core $\nu_\mathrm{c}$ and of the shell $\nu_\mathrm{s}$

The constants $c_{01,n}$ to $c_{67,n}$ only depend on the index $n$, the Poisson ratio of the core $\nu_\mathrm{c}$ and of the shell $\nu_\mathrm{s}$. They are listed below:

$$
\begin{aligned}
c_{01,n} &= 0,\\
c_{02,n} &= -\frac{4(-1+n)^2(3+8n+4n^2)(-1+\nu_\mathrm{s})(-2-3n+2\nu_\mathrm{s}+4n\nu_\mathrm{s})}{(1+\nu_\mathrm{c})(1+\nu_\mathrm{s})^2},\\
c_{03,n} &= -\frac{2(1+2n)^2(-3+n+2n^2)(-1+\nu_\mathrm{s})(-2+n^2+2\nu_\mathrm{s})}{(1+\nu_\mathrm{c})(1+\nu_\mathrm{s})^2},\\
c_{04,n} &= \frac{2n(2+n)(3-n-14n^2+4n^3+8n^4)(-1+\nu_\mathrm{s})}{(1+\nu_\mathrm{c})(1+\nu_\mathrm{s})^2},\\
c_{05,n} &= 0,\\
c_{06,n} &= \frac{4(-1+n)(3+8n+4n^2)(-1+\nu_\mathrm{s})(1+n+n^2-\nu_\mathrm{s}-2n\nu_\mathrm{s})}{(1+\nu_\mathrm{s})^3},
\end{aligned}
$$

$$
\begin{aligned}
c_{07,n} &= \frac{2(1+2n)^2(-3+n+2n^2)(-1+\nu_\mathrm{s})(-2+n^2+2\nu_\mathrm{s})}{(1+\nu_\mathrm{s})^3}, \\
c_{08,n} &= -\frac{2n(2+n)(3-n-14n^2+4n^3+8n^4)(-1+\nu_\mathrm{s})}{(1+\nu_\mathrm{s})^3}, \\
c_{09,n} &= \frac{4(-1+4n^2)(1+n+n^2+\nu_\mathrm{c}+2n\nu_\mathrm{c})(-1+\nu_\mathrm{s})(-1+2n+n^2+2\nu_\mathrm{s})}{(1+\nu_\mathrm{c})(1+\nu_\mathrm{s})^2}, \\
c_{10,n} &= -\frac{4(-1+n)(3+11n+12n^2+4n^3)(-1+\nu_\mathrm{s})(5-\nu_\mathrm{c}-6\nu_\mathrm{s}+2n(-1+\nu_\mathrm{c}+\nu_\mathrm{s})+n^2(-2+4\nu_\mathrm{s}))}{(1+\nu_\mathrm{c})(1+\nu_\mathrm{s})^2}, \\
c_{11,n} &= -\frac{2(3+2n)^2(-1-2n+n^2+2n^3)(-1+\nu_\mathrm{s})(-2+n^2+2\nu_\mathrm{s})}{(1+\nu_\mathrm{c})(1+\nu_\mathrm{s})^2}, \\
c_{12,n} &= 2(2+n)(-1+4n^2)(-1+\nu_\mathrm{s})\left[\frac{5n^3+2n^4+n^2(6-8\nu_\mathrm{s})}{(1+\nu_\mathrm{c})(1+\nu_\mathrm{s})^2}\right. \\
&\quad \left.+\ \frac{-4(1+\nu_\mathrm{c})(-1+2\nu_\mathrm{s})-n(1+8\nu_\mathrm{s}+4\nu_\mathrm{c}(-3+4\nu_\mathrm{s}))}{(1+\nu_\mathrm{c})(1+\nu_\mathrm{s})^2}\right], \\
c_{13,n} &= -\frac{4(-2-n+8n^2+4n^3)(-1+2\nu_\mathrm{c}+n(-3+4\nu_\mathrm{c}))(-1+\nu_\mathrm{s})(-1+2n+n^2+2\nu_\mathrm{s})}{(1+\nu_\mathrm{s})^3}, \\
c_{14,n} &= \frac{4(-1+n)(3+11n+12n^2+4n^3)(-1+\nu_\mathrm{s})(5-4\nu_\mathrm{c}+n^2(-2+4\nu_\mathrm{c})-3\nu_\mathrm{s}+n(6\nu_\mathrm{c}-2(1+\nu_\mathrm{s})))}{(1+\nu_\mathrm{s})^3}, \\
c_{15,n} &= \frac{2(3+2n)^2(-1-2n+n^2+2n^3)(-1+\nu_\mathrm{s})(-2+n^2+2\nu_\mathrm{s})}{(1+\nu_\mathrm{s})^3}, \\
c_{16,n} &= -2(2+n)(-1+4n^2)(-1+\nu_\mathrm{s})\left[\frac{5n^3+2n^4+n^2(6-8\nu_\mathrm{c})}{(1+\nu_\mathrm{s})^3}\right. \\
&\quad \left.+\ \frac{-4(-1+2\nu_\mathrm{c})(1+\nu_\mathrm{s})-n(1-12\nu_\mathrm{s}+8\nu_\mathrm{c}(1+2\nu_\mathrm{s}))}{(1+\nu_\mathrm{s})^3}\right], \\
c_{17,n} &= \frac{4(-1+n)^2(1+n+n^2+\nu_\mathrm{c}+2n\nu_\mathrm{c})(-2-3n+2\nu_\mathrm{s}+4n\nu_\mathrm{s})}{(1+\nu_\mathrm{c})^2(1+\nu_\mathrm{s})}, \\
c_{18,n} &= \frac{2(-1+n)(1+2n)(1+n+n^2+\nu_\mathrm{c}+2n\nu_\mathrm{c})(-2+n^2+2\nu_\mathrm{s})}{(1+\nu_\mathrm{c})^2(1+\nu_\mathrm{s})}, \\
c_{19,n} &= -\frac{2(-1+n)n(2+n)(-1+2n)(1+n+n^2+\nu_\mathrm{c}+2n\nu_\mathrm{c})}{(1+\nu_\mathrm{c})^2(1+\nu_\mathrm{s})}, \\
c_{20,n} &= -4(-1+n)\left[\frac{-3(-1+3\nu_\mathrm{c})(-1+\nu_\mathrm{s})+n^2(-4+\nu_\mathrm{c}(9-16\nu_\mathrm{s})+9\nu_\mathrm{s})}{(1+\nu_\mathrm{c})(1+\nu_\mathrm{s})^2}\right. \\
&\quad \left.+\frac{n(-14+\nu_\mathrm{c}(27-32\nu_\mathrm{s})+15\nu_\mathrm{s})+4n^3(5-6\nu_\mathrm{s}+\nu_\mathrm{c}(-6+8\nu_\mathrm{s}))+2n^4(5-6\nu_\mathrm{s}+\nu_\mathrm{c}(-6+8\nu_\mathrm{s}))}{(1+\nu_\mathrm{c})(1+\nu_\mathrm{s})^2}\right], \\
c_{21,n} &= -\frac{2(-1-n+2n^2)(-1+5\nu_\mathrm{c}+6n(-1+2\nu_\mathrm{c})+n^2(-2+4\nu_\mathrm{c}))(-2+n^2+2\nu_\mathrm{s})}{(1+\nu_\mathrm{c})(1+\nu_\mathrm{s})^2}, \\
c_{22,n} &= \frac{2n(2+n)(1-3n+2n^2)(-1+5\nu_\mathrm{c}+6n(-1+2\nu_\mathrm{c})+n^2(-2+4\nu_\mathrm{c}))}{(1+\nu_\mathrm{c})(1+\nu_\mathrm{s})^2}, \\
c_{23,n} &= \frac{4(-1+n)(2+n)(-1+2\nu_\mathrm{c}+n(-3+4\nu_\mathrm{c}))(1+n+n^2-\nu_\mathrm{s}-2n\nu_\mathrm{s})}{(1+\nu_\mathrm{s})^3}, \\
c_{24,n} &= \frac{2(-2-3n+3n^2+2n^3)(-1+2\nu_\mathrm{c}+n(-3+4\nu_\mathrm{c}))(-2+n^2+2\nu_\mathrm{s})}{(1+\nu_\mathrm{s})^3}, \\
c_{25,n} &= -\frac{2n(2+n)^2(1-3n+2n^2)(-1+2\nu_\mathrm{c}+n(-3+4\nu_\mathrm{c}))}{(1+\nu_\mathrm{s})^3}, \\
c_{26,n} &= \frac{4(-1+n)(1+n+n^2+\nu_\mathrm{c}+2n\nu_\mathrm{c})(-2-3n+2\nu_\mathrm{s}+4n\nu_\mathrm{s})(-1+2n+n^2+2\nu_\mathrm{s})}{(1+\nu_\mathrm{s})(1+\nu_\mathrm{c})^2}, \\
c_{27,n} &= \frac{2(-1+n)(3+5n+2n^2)(1+n+n^2+\nu_\mathrm{c}+2n\nu_\mathrm{c})(-2+n^2+2\nu_\mathrm{s})}{(1+\nu_\mathrm{c})^2(1+\nu_\mathrm{s})}, \\
c_{28,n} &= -\frac{2(-1+n)(2+n)(1+2n)(1+n+n^2+\nu_\mathrm{c}+2n\nu_\mathrm{c})(8+n+n^2-24\nu_\mathrm{s}+16\nu_\mathrm{s}^2)}{(1+\nu_\mathrm{c})^2(1+\nu_\mathrm{s})}, \\
c_{29,n} &= -4(-1+2n+n^2+2\nu_\mathrm{s})\left[\frac{-3(-1+3\nu_\mathrm{c})(-1+\nu_\mathrm{s})+n^2(-4+\nu_\mathrm{c}(9-16\nu_\mathrm{s})+9\nu_\mathrm{s})}{(1+\nu_\mathrm{c})(1+\nu_\mathrm{s})^2}\right. \\
&\quad \left.+\frac{n(-14+\nu_\mathrm{c}(27-32\nu_\mathrm{s})+15\nu_\mathrm{s})+4n^3(5-6\nu_\mathrm{s}+\nu_\mathrm{c}(-6+8\nu_\mathrm{s}))+2n^4(5-6\nu_\mathrm{s}+\nu_\mathrm{c}(-6+8\nu_\mathrm{s}))}{(1+\nu_\mathrm{c})(1+\nu_\mathrm{s})^2}\right],
\end{aligned}
$$

$$c_{30,n} = -\frac{2(-3-2n+3n^2+2n^3)(-1+5\nu_\mathrm{c}+6n(-1+2\nu_\mathrm{c})+n^2(-2+4\nu_\mathrm{c}))(-2+n^2+2\nu_\mathrm{s})}{(1+\nu_\mathrm{c})(1+\nu_\mathrm{s})^2},$$

$$\begin{aligned}c_{31,n} &= 2(2+n)(1+2n)\left[\frac{6n^4(-1+2\nu_\mathrm{c})+n^5(-2+4\nu_\mathrm{c})-12(-1+\nu_\mathrm{s})(-1+\nu_\mathrm{c}+2\nu_\mathrm{c}\nu_\mathrm{s})-n(11+\nu_\mathrm{c}-4\nu_\mathrm{s}-28\nu_\mathrm{c}\nu_\mathrm{s}-8\nu_\mathrm{s}^2+32\nu_\mathrm{c}\nu_\mathrm{s}^2)}{(1+\nu_\mathrm{c})(1+\nu_\mathrm{s})^2}\right.\\ &\left.+\frac{n^3(9-8\nu_\mathrm{s}+\nu_\mathrm{c}(-15+16\nu_\mathrm{s}))+2n^2(3+16\nu_\mathrm{s}-16\nu_\mathrm{s}^2+2\nu_\mathrm{c}(-7-4\nu_\mathrm{s}+8\nu_\mathrm{s}^2))}{(1+\nu_\mathrm{c})(1+\nu_\mathrm{s})^2}\right],\end{aligned}$$

$$c_{32,n} = \frac{4(2+n)(-1+2\nu_\mathrm{c}+n(-3+4\nu_\mathrm{c}))(-1+2n+n^2+2\nu_\mathrm{s})(1+n+n^2-\nu_\mathrm{s}-2n\nu_\mathrm{s})}{(1+\nu_\mathrm{s})^3},$$

$$c_{33,n} = \frac{2(2+n)(-3-2n+3n^2+2n^3)(-1+2\nu_\mathrm{c}+n(-3+4\nu_\mathrm{c}))(-2+n^2+2\nu_\mathrm{s})}{(1+\nu_\mathrm{s})^3},$$

$$c_{34,n} = -\frac{2(2+n)(1+2n)(-1+2\nu_\mathrm{c}+n(-3+4\nu_\mathrm{c}))(4-2n-n^2+2n^3+n^4-4\nu_\mathrm{s}^2)}{(1+\nu_\mathrm{s})^3},$$

$$c_{35,n} = -\frac{2(-1+n)(1+2n)(1+n+n^2+\nu_\mathrm{c}+2n\nu_\mathrm{c})(-1+2n+n^2+2\nu_\mathrm{s})}{(1+\nu_\mathrm{s})(1+\nu_\mathrm{c})^2},$$

$$c_{36,n} = \frac{2(-1+n)^2(3+5n+2n^2)(1+n+n^2+\nu_\mathrm{c}+2n\nu_\mathrm{c})}{(1+\nu_\mathrm{c})^2(1+\nu_\mathrm{s})},$$

$$c_{37,n} = \frac{4(-1+n)(2+n)(1+n+n^2+\nu_\mathrm{c}+2n\nu_\mathrm{c})(-1+2\nu_\mathrm{s}+n(-3+4\nu_\mathrm{s}))}{(1+\nu_\mathrm{c})^2(1+\nu_\mathrm{s})},$$

$$c_{38,n} = \frac{2(-1-n+2n^2)(-1+5\nu_\mathrm{c}+6n(-1+2\nu_\mathrm{c})+n^2(-2+4\nu_\mathrm{c}))(-1+2n+n^2+2\nu_\mathrm{s})}{(1+\nu_\mathrm{c})(1+\nu_\mathrm{s})^2},$$

$$c_{39,n} = -\frac{2(-1+n)^2(3+5n+2n^2)(-1+5\nu_\mathrm{c}+6n(-1+2\nu_\mathrm{c})+n^2(-2+4\nu_\mathrm{c}))}{(1+\nu_\mathrm{c})(1+\nu_\mathrm{s})^2},$$

$$c_{40,n} = -\frac{4(-1+n)(2+n)(-2+\nu_\mathrm{c}+\nu_\mathrm{s}+4\nu_\mathrm{c}\nu_\mathrm{s}+n^3(-6+4\nu_\mathrm{c}+4\nu_\mathrm{s})+8n^2(-1+2\nu_\mathrm{c}\nu_\mathrm{s})+n(-8+\nu_\mathrm{c}+\nu_\mathrm{s}+16\nu_\mathrm{c}\nu_\mathrm{s}))}{(1+\nu_\mathrm{c})(1+\nu_\mathrm{s})^2},$$

$$c_{41,n} = -\frac{2(-2-3n+3n^2+2n^3)(-1+2\nu_\mathrm{c}+n(-3+4\nu_\mathrm{c}))(-1+2n+n^2+2\nu_\mathrm{s})}{(1+\nu_\mathrm{s})^3},$$

$$c_{42,n} = \frac{2(-1+n)^2(2+n)(3+5n+2n^2)(-1+2\nu_\mathrm{c}+n(-3+4\nu_\mathrm{c}))}{(1+\nu_\mathrm{s})^3},$$

$$c_{43,n} = \frac{4(-1+n)(2+n)(-1+2\nu_\mathrm{c}+n(-3+4\nu_\mathrm{c}))(1+n+n^2+\nu_\mathrm{s}+2n\nu_\mathrm{s})}{(1+\nu_\mathrm{s})^3},$$

$$c_{44,n} = \frac{2(-1+n)n(-1+2n)(1+n+n^2+\nu_\mathrm{c}+2n\nu_\mathrm{c})(-1+2n+n^2+2\nu_\mathrm{s})}{(1+\nu_\mathrm{s})(1+\nu_\mathrm{c})^2},$$

$$c_{45,n} = -\frac{2(-1+n)^2(1+2n)(1+n+n^2+\nu_\mathrm{c}+2n\nu_\mathrm{c})(8+n+n^2-24\nu_\mathrm{s}+16\nu_\mathrm{s}^2)}{(1+\nu_\mathrm{c})^2(1+\nu_\mathrm{s})},$$

$$c_{46,n} = -\frac{4(-1+n)(1+n+n^2+\nu_\mathrm{c}+2n\nu_\mathrm{c})(-2+n^2+2\nu_\mathrm{s})(-1+2\nu_\mathrm{s}+n(-3+4\nu_\mathrm{s}))}{(1+\nu_\mathrm{c})^2(1+\nu_\mathrm{s})},$$

$$c_{47,n} = -\frac{2n(1-3n+2n^2)(-1+5\nu_\mathrm{c}+6n(-1+2\nu_\mathrm{c})+n^2(-2+4\nu_\mathrm{c}))(-1+2n+n^2+2\nu_\mathrm{s})}{(1+\nu_\mathrm{c})(1+\nu_\mathrm{s})^2},$$

$$\begin{aligned}c_{48,n} &= 2(-1+n)(1+2n)\left[\frac{6n^4(-1+2\nu_\mathrm{c})+n^5(-2+4\nu_\mathrm{c})-12(-1+\nu_\mathrm{s})(-1+\nu_\mathrm{c}+2\nu_\mathrm{c}\nu_\mathrm{s})-n(11+\nu_\mathrm{c}-4\nu_\mathrm{s}-28\nu_\mathrm{c}\nu_\mathrm{s}-8\nu_\mathrm{s}^2+32\nu_\mathrm{c}\nu_\mathrm{s}^2)}{(1+\nu_\mathrm{c})(1+\nu_\mathrm{s})^2}\right.\\ &\left.+\frac{n^3(9-8\nu_\mathrm{s}+\nu_\mathrm{c}(-15+16\nu_\mathrm{s}))+2n^2(3+16\nu_\mathrm{s}-16\nu_\mathrm{s}^2+2\nu_\mathrm{c}(-7-4\nu_\mathrm{s}+8\nu_\mathrm{s}^2))}{(1+\nu_\mathrm{c})(1+\nu_\mathrm{s})^2}\right],\end{aligned}$$

$$c_{49,n} = \frac{4(-1+n)(-2+n^2+2\nu_\mathrm{s})(-2+\nu_\mathrm{c}+\nu_\mathrm{s}+4\nu_\mathrm{c}\nu_\mathrm{s}+n^3(-6+4\nu_\mathrm{c}+4\nu_\mathrm{s})+8n^2(-1+2\nu_\mathrm{c}\nu_\mathrm{s})+n(-8+\nu_\mathrm{c}+\nu_\mathrm{s}+16\nu_\mathrm{c}\nu_\mathrm{s}))}{(1+\nu_\mathrm{c})(1+\nu_\mathrm{s})^2},$$

$$c_{50,n} = \frac{2n(2-5n+n^2+2n^3)(-1+2\nu_\mathrm{c}+n(-3+4\nu_\mathrm{c}))(-1+2n+n^2+2\nu_\mathrm{s})}{(1+\nu_\mathrm{s})^3},$$

$$c_{51,n} = -\frac{2(-1+n)(1+2n)(-1+2\nu_\mathrm{c}+n(-3+4\nu_\mathrm{c}))(4-2n-n^2+2n^3+n^4-4\nu_\mathrm{s}^2)}{(1+\nu_\mathrm{s})^3},$$

$$c_{52,n} = -\frac{4(-1+n)(-1+2\nu_\mathrm{c}+n(-3+4\nu_\mathrm{c}))(-2+n^2+2\nu_\mathrm{s})(1+n+n^2+\nu_\mathrm{s}+2n\nu_\mathrm{s})}{(1+\nu_\mathrm{s})^3},$$

$$c_{53,n} = -\frac{8(-1+n)^2(1+n+n^2+\nu_\mathrm{c}+2n\nu_\mathrm{c})(1+n+n^2+\nu_\mathrm{s}+2n\nu_\mathrm{s})(-2-3n+2\nu_\mathrm{s}+4n\nu_\mathrm{s})}{(1+\nu_\mathrm{c})^2(1+\nu_\mathrm{s})^2},$$

$$c_{54,n} = \frac{2(-1+n)(1+2n)^2(1+n+n^2+\nu_\mathrm{c}+2n\nu_\mathrm{c})(4-2n-n^2+2n^3+n^4-4\nu_\mathrm{s}^2)}{(1+\nu_\mathrm{c})^2(1+\nu_\mathrm{s})^2},$$

$$c_{55,n} = -\frac{4(-1+n)^2n(-6-n+17n^2+16n^3+4n^4)(1+n+n^2+\nu_\mathrm{c}+2n\nu_\mathrm{c})}{(1+\nu_\mathrm{c})^2(1+\nu_\mathrm{s})^2},$$

$$c_{56,n} = \frac{2(-1+n)^2(2+n)(1+2n)^2(1+n+n^2+\nu_\mathrm{c}+2n\nu_\mathrm{c})(8+n+n^2-24\nu_\mathrm{s}+16\nu_\mathrm{s}^2)}{(1+\nu_\mathrm{c})^2(1+\nu_\mathrm{s})^2},$$

$$c_{57,n} = -\frac{8(-1+n)(2+n)(1+n+n^2+\nu_\mathrm{c}+2n\nu_\mathrm{c})(1+n+n^2-\nu_\mathrm{s}-2n\nu_\mathrm{s})(-1+2\nu_\mathrm{s}+n(-3+4\nu_\mathrm{s}))}{(1+\nu_\mathrm{c})^2(1+\nu_\mathrm{s})^2},$$

$$\begin{aligned} c_{58,n} &= 8(-1+n)(1+n+n^2+\nu_\mathrm{s}+2n\nu_\mathrm{s})\left[\frac{-3(-1+3\nu_\mathrm{c})(-1+\nu_\mathrm{s})+n^2(-4+\nu_\mathrm{c}(9-16\nu_\mathrm{s})+9\nu_\mathrm{s})}{(1+\nu_\mathrm{c})(1+\nu_\mathrm{s})^3}\right.\\ &\left.+\frac{n(-14+\nu_\mathrm{c}(27-32\nu_\mathrm{s})+15\nu_\mathrm{s})+4n^3(5-6\nu_\mathrm{s}+\nu_\mathrm{c}(-6+8\nu_\mathrm{s}))+2n^4(5-6\nu_\mathrm{s}+\nu_\mathrm{c}(-6+8\nu_\mathrm{s}))}{(1+\nu_\mathrm{c})(1+\nu_\mathrm{s})^3}\right], \end{aligned}$$

$$c_{59,n} = -\frac{2(-1+n)(1+2n)^2(-1+5\nu_\mathrm{c}+6n(-1+2\nu_\mathrm{c})+n^2(-2+4\nu_\mathrm{c}))(4-2n-n^2+2n^3+n^4-4\nu_\mathrm{s}^2)}{(1+\nu_\mathrm{c})(1+\nu_\mathrm{s})^3},$$

$$c_{60,n} = \frac{4(-1+n)^2n(-6-n+17n^2+16n^3+4n^4)(-1+5\nu_\mathrm{c}+6n(-1+2\nu_\mathrm{c})+n^2(-2+4\nu_\mathrm{c}))}{(1+\nu_\mathrm{c})(1+\nu_\mathrm{s})^3},$$

$$\begin{aligned} c_{61,n} &= -2(1+2n)^2(-2+n+n^2)\left[\frac{6n^4(-1+2\nu_\mathrm{c})+n^5(-2+4\nu_\mathrm{c})-12(-1+\nu_\mathrm{s})(-1+\nu_\mathrm{c}+2\nu_\mathrm{c}\nu_\mathrm{s})}{(1+\nu_\mathrm{c})(1+\nu_\mathrm{s})^3}\right.\\ &\left.+\frac{-n(11+\nu_\mathrm{c}-4\nu_\mathrm{s}-28\nu_\mathrm{c}\nu_\mathrm{s}-8\nu_\mathrm{s}^2+32\nu_\mathrm{c}\nu_\mathrm{s}^2)+n^3(9-8\nu_\mathrm{s}+\nu_\mathrm{c}(-15+16\nu_\mathrm{s}))+2n^2(3+16\nu_\mathrm{s}-16\nu_\mathrm{s}^2+2\nu_\mathrm{c}(-7-4\nu_\mathrm{s}+8\nu_\mathrm{s}^2))}{(1+\nu_\mathrm{c})(1+\nu_\mathrm{s})^3}\right], \end{aligned}$$

$$\begin{aligned} c_{62,n} &= 8(-1+n)(2+n)(1+n+n^2-\nu_\mathrm{s}-2n\nu_\mathrm{s})\left[\frac{-2+\nu_\mathrm{c}+\nu_\mathrm{s}+4\nu_\mathrm{c}\nu_\mathrm{s}+n^3(-6+4\nu_\mathrm{c}+4\nu_\mathrm{s})+8n^2(-1+2\nu_\mathrm{c}\nu_\mathrm{s})}{(1+\nu_\mathrm{c})(1+\nu_\mathrm{s})^3}\right.\\ &\left.+\frac{n(-8+\nu_\mathrm{c}+\nu_\mathrm{s}+16\nu_\mathrm{c}\nu_\mathrm{s})}{(1+\nu_\mathrm{c})(1+\nu_\mathrm{s})^3}\right], \end{aligned}$$

$$c_{63,n} = -\frac{8(-1+n)(2+n)(-1+2\nu_\mathrm{c}+n(-3+4\nu_\mathrm{c}))(1+n+n^2-\nu_\mathrm{s}-2n\nu_\mathrm{s})(1+n+n^2+\nu_\mathrm{s}+2n\nu_\mathrm{s})}{(1+\nu_\mathrm{s})^4},$$

$$c_{64,n} = \frac{2(1+2n)^2(-2+n+n^2)(-1+2\nu_\mathrm{c}+n(-3+4\nu_\mathrm{c}))(4-2n-n^2+2n^3+n^4-4\nu_\mathrm{s}^2)}{(1+\nu_\mathrm{s})^4},$$

$$c_{65,n} = -\frac{4n(-2+n+n^2)^2(-3+n+8n^2+4n^3)(-1+2\nu_\mathrm{c}+n(-3+4\nu_\mathrm{c}))}{(1+\nu_\mathrm{s})^4},$$

$$c_{66,n} = \frac{2(-1+n)(2+n)(1+2n)^2(-1+2\nu_\mathrm{c}+n(-3+4\nu_\mathrm{c}))(4-2n-n^2+2n^3+n^4-4\nu_\mathrm{s}^2)}{(1+\nu_\mathrm{s})^4},$$

$$c_{67,n} = -\frac{8(-1+n)(2+n)(-1+2\nu_\mathrm{c}+n(-3+4\nu_\mathrm{c}))(1+n+n^2-\nu_\mathrm{s}-2n\nu_\mathrm{s})(1+n+n^2+\nu_\mathrm{s}+2n\nu_\mathrm{s})}{(1+\nu_\mathrm{s})^4}.$$

## Asymptotic behaviour of the Legendre polynomials $P_n$ and the general rescaled solutions for the radial component of the displacement field for the core $u_r^{(\mathrm{c})}/R_c$ and for the shell $u_r^{(\mathrm{s})}/R_s$

For the Legendre polynomials $P_n(\cos\theta)$ with $\theta = \pi/2$, the dependence on the index $n$ is as follows[1]

$$P_n(0) = \begin{cases} \frac{(-1)^m}{2^{2m}} \frac{(2m)!}{(m!)^2} & \text{for} \quad n = 2m, \\ 0 & \text{for} \quad n = 2m+1. \end{cases} \tag{7}$$

Let $a_m = \frac{1}{2^{2m}} \frac{(2m)!}{(m!)^2}$. To calculate the asymptotic behaviour of this coefficient for $m \to \infty$, Stirling's formula can be used:

$$N! = \sqrt{2\pi N} \left(\frac{N}{e}\right)^N \left(1 + \mathcal{O}\left(\frac{1}{N}\right)\right), \tag{8}$$

where $e$ denotes Euler's number. Applying this formula to $a_m$ leads (for large $m$) to:

$$\begin{aligned} a_m &\approx \frac{1}{2^{2m}} \frac{\sqrt{2\pi 2m}}{2\pi m} \left(\frac{2m}{e}\right)^{2m} \left(\frac{e}{m}\right)^{2m} \\ &= \frac{2^{2m}}{2^{2m}} \frac{\sqrt{2\pi 2m}}{2\pi m} \\ &= \frac{1}{\sqrt{\pi m}}. \end{aligned} \tag{9}$$

Thus, the following asymptotic behaviour for $P_n(0)$ results:

$$P_n(0) \approx \begin{cases} \sqrt{\frac{2}{\pi n}} & \text{for} \quad n \,\text{even}, \\ 0 & \text{for} \quad n \,\text{odd}. \end{cases} \tag{10}$$

Furthermore, the dependence on the index $n$ for the angles $\theta = 0, \pi$ gives[1]

$$P_n\,(1) = 1, \tag{11}$$

$$P_n\,(-1) = \begin{cases} 1 & \text{for } \; n \,\text{even}, \\ -1 & \text{for } \; n \,\text{odd}. \end{cases} \tag{12}$$

The case of $n$ being odd is, due to the assumed mirror symmetry, irrelevant for the investigated problem, therefore $P_n(\cos 0) = P_n(\cos \pi) = 1$ holds true.

The general rescaled solution for the radial component of the displacement field for the core $u_r^{(\mathrm{c})}/R_c$ is obtained at the core radius $R_c$ as follows

$$\frac{u_r^{(\mathrm{c})}(R_c\mathbf{e}_r)}{R_c} = \sum_{n=0}^{\infty} G_{r,n}^{(\mathrm{c})}\left(\frac{\lambda}{E_s R_s}, \frac{E_c}{E_s}, \frac{R_c}{R_s}, \nu_c, \nu_s\right) \frac{2n+1}{2} P_n\,(0)\, P_n\,(\cos\theta) \tag{13}$$

where $G_{r,n}^{(\mathrm{c})}\,(\lambda/(E_s R_s), E_c/E_s, R_c/R_s, \nu_c, \nu_s)$ is the corresponding kernel function of the core and the remaining factors in the sum result from the expansion of the Dirac delta function in Legendre polynomials. In terms of the coefficients $a_n^{(c)}$ and $b_n^{(c)}$, (13) can also be written as

$$\begin{aligned} \frac{u_r^{(\mathrm{c})}\,(R_c\mathbf{e}_r)}{R_c} &= \sum_{n=0}^{\infty}\left(\frac{a_n^{(c)}}{R_c} R_c^{n+1}(n+1)(-2+n+4\nu_c) + \frac{b_n^{(c)}}{R_c} R_c^{n-1} n\right) P_n\,(\cos\theta) \\ &= \sum_{n=0}^{\infty} \frac{2n+1}{2} P_n(0) P_n\,(\cos\theta) \left(\frac{R_c}{R_s}\right)^{(n-2)} \frac{\lambda}{E_s R_s} \\ &\quad \times \frac{1}{D}\left(\underbrace{\left[\left(\frac{E_c}{E_s}\right)\tilde{c}_{01,n} + \tilde{c}_{02,n}\right](n+1)(-2+n+4\nu_c)}_{I} - \underbrace{\left[\left(\frac{E_c}{E_s}\right)\tilde{c}_{03,n} + \tilde{c}_{04,n}\right] n}_{II}\right). \end{aligned} \tag{14}$$

Comparing the solution for $u_r^{(\mathrm{c})}/R_c$ here with that in (13), it can be concluded that the kernel function of the core $G_{r,n}^{(\mathrm{c})}$ is the product of the factors $(R_c/R_s)^{(n-2)}$, $\lambda/(E_s R_s)$, $1/D$

(see Eq. (6)) and the sum of 14I + 14II. By multiplying the sum 14I + 14II by $1/D$, an order in index $n$ of $\mathcal{O}(1)$ can be proved in the asymptotic behaviour of the limit $n \to \infty$ for $R_c/R_s < 1$. Therefore, the factor $(R_c/R_s)^{(n-2)}$ is the dominant factor in the asymptotic behaviour for the limit $n \to \infty$ of the kernel function of the core $G_{r,n}^{(\mathrm{c})}$. Combined with the $n$-dependence of the Legendre polynomials $P_n(\cos\theta)$ the general rescaled radial solution of the core $u_r^{(\mathrm{c})}/R_c$ at the core radius $R_c$ gives a convergent series at the poles and at the equator, due to the $(R_c/R_s)^n$-dependence ($R_c/R_s < 1$, exponential decrease).

The general rescaled solution for the radial component of the displacement field for the shell $u_r^{(\mathrm{s})}/R_s$ is obtained at the outer shell radius $R_s$ as

$$\frac{u_r^{(\mathrm{s})}(R_s\mathbf{e}_r)}{R_s} = \sum_{n=0}^{\infty} G_{r,n}^{(\mathrm{s})}\left(\frac{\lambda}{E_sR_s}, \frac{E_c}{E_s}, \frac{R_c}{R_s}, \nu_c, \nu_s\right) \frac{2n+1}{2} P_n(0)\, P_n(\cos\theta) \tag{15}$$

where $G_{r,n}^{(\mathrm{s})}\left(\lambda/(E_sR_s), E_c/E_s, R_c/R_s, \nu_c, \nu_s\right)$ is the corresponding kernel function of the shell and the remaining factors are the same as for the core solution. In terms of the coefficients

$a_n^{(s)}$, $b_n^{(s)}$, $c_n^{(c)}$ and $d_n^{(c)}$, (15) can also be written as

$$
\begin{aligned}
\frac{u_r^{(\mathrm{s})}\left(R_s\mathbf{e}_r\right)}{R_s} &= \sum_{n=0}^{\infty}\left(\frac{a_n^{(s)}}{R_s}R_s^{n+1}(n+1)(-2+n+4\nu_s)+\frac{b_n^{(s)}}{R_s}R_s^{n-1}n\right.\\
&\qquad \left.+\frac{c_n^{(s)}}{R_s}R_s^{-n}n(3+n-4\nu_s)-\frac{d_n^{(s)}}{R_s}R_2^{-(n+2)}(n+1)\right)P_n\left(\cos\theta\right)\\
&= \sum_{n=0}^{\infty}\frac{2n+1}{2}P_n(0)P_n\left(\cos\theta\right)\frac{\lambda}{E_sR_s}\\
&\qquad \times\frac{1}{D}\left(\underbrace{\left[\left(\frac{E_c}{E_s}\right)^2\tilde{c}_{05,n}+\left(\frac{E_c}{E_s}\right)\tilde{c}_{06,n}+\tilde{c}_{07,n}\right](n+1)(-2+n+4\nu_s)}_{I}\right.\\
&\qquad \underbrace{-\left[\left(\frac{E_c}{E_s}\right)^2\tilde{c}_{08,n}+\left(\frac{E_c}{E_s}\right)\tilde{c}_{09,n}+\tilde{c}_{10,n}\right]n}_{II}\\
&\qquad \underbrace{+\left(\frac{R_c}{R_s}\right)^{(2n-1)}\left[\left(\frac{E_c}{E_s}\right)^2\tilde{c}_{11,n}+\left(\frac{E_c}{E_s}\right)\tilde{c}_{12,n}+\tilde{c}_{13,n}\right]n(3+n-4\nu_s)}_{III}\\
&\qquad \left.\underbrace{+\left(\frac{R_c}{R_s}\right)^{(2n+1)}\left[\left(\frac{E_c}{E_s}\right)^2\tilde{c}_{14,n}+\left(\frac{E_c}{E_s}\right)\tilde{c}_{15,n}+\tilde{c}_{16,n}\right](n+1)}_{IV}\right)
\end{aligned}
\tag{16}
$$

By comparing the solution for $u_r^{(\mathrm{s})}/R_s$ with that in (15), it can be concluded that the kernel function of the shell $G_{r,n}^{(\mathrm{s})}$ is the product of the factors $\lambda/(E_sR_s)$, $1/D$ and the sum of 16I + 16II + 16III + 16IV. By multiplying the sum 16I + 16II by $1/D$, an order in index $n$ of $\mathcal{O}(1/n)$ can be proved in the asymptotic behaviour of the limit $n \to \infty$ for $R_c/R_s < 1$. Multiplying the sum 16III + 16IV by $1/D$ leads to a dominant factor of $(R_c/R_s)^{2n}$ under the same conditions. Therefore, the asymptotic behaviour for $n \to \infty$ is proportional to $1/n$ for the kernel function of the shell $G_{r,n}^{(\mathrm{s})}$. Combined with the $n$-dependence of the Legendre polynomials $P_n\left(\cos\theta\right)$ the general rescaled radial solution for the shell $u_r^{(\mathrm{s})}/R_s$ at the outer shell radius $R_s$ results in a divergent series at the equator ($\theta = \pi/2$), due to the $1/n$-dependence of $G^{(\mathrm{s})}_{r,n}$ (harmonic series) and a convergent series at the poles ($\theta = 0, \pi$), due to the property of the Legendre polynomials at the poles (alternating series and a monotonic decrease to zero of the absolute value of the summands).

## References

(1) Arfken, G., Weber H.; *Mathematical Methods for Physicists*; Elsevier Academic Press, United Kingdom, 2005.

# Chapter 3

# Scientific Appendix Chapters

In the following, Scientific Appendix Chapters 3.1–3.2 that form the basis of this dissertation are attached. For each appendix Chapter, I present a summary of my contributions.

## 3.1 Microgels trapped between two interfaces

### Statement of contribution

Hartmut Löwen, and I developed the theory/idea. I performed the numerical evaluations and prepared the data and figures. HL and I wrote the manuscript.

### 3.1.1 Materials and Methods

In the following, we model both a single or a pair of microgel particles ($N_m = 1, 2$) which are confined in a slit-geometry between two parallel planar water-oil interfaces at a distance $d$. An additional lateral confinement in a cylindrical cell of radius $R_c$ is employed to mimick a finite areal number density of microgel particles which is given by $N_m/\pi R_c^2$. For two microgels, $N_m = 2$, the microgels are assumed to be adsorbed separatedly on either one of the two water-oil interfaces. We then change the distance $d$ of the interfaces slowly and compute the corresponding osmotic pressure exerted on the two interfaces as a function of $d$ also extrcating typical snapshots of the microgel monomer configurations.

The modelling of the microgels is done as in Refs. [46, 70, 71, 77] at a monomer-resolved level with implicit solvent. A microgel explicitly consists of two types of beads, the monomers and the crosslinkers. The internal structure of a microgel is defined by these two components. Both monomers and crosslinkers are covalently bonded to other monomers or crosslinkers. Monomers are twofold bounded and crosslinkers fourfold. In all other properties, monomers and crosslinkers are identical and are therefore referenced as beads in the following. The covalent bonds between the different beads are modelled by a finite-extensible-nonlinear-elastic (FENE) potential. This potential is defined by a characteristic energy strength $\varepsilon$, a maximum bond length $\tilde{R}_0 = 1.5\sigma$ and an effective spring constant $\tilde{k}_f = 15\varepsilon/\sigma^2$, see SI (3.1.3). The repulsive bead-bead interaction is described by a Week-Chandler-Anderson (WCA) potential, also with the characteristic strength of repulsion $\varepsilon$ and the repulsive length $\sigma$, see SI (3.1.3). Since the strength and length of repulsion for the WCA potential and the FENE potential are the same, $\varepsilon$ is chosen as the energy unit for the simulation and $\sigma$ as the length unit.

The thermoresponsivity of the microgel is described by an additional attractive bead-bead pair potential [44, 46] given by

$$V_\alpha(r) = \begin{cases} -\alpha\varepsilon & \text{if} \quad r \leq 2^{\frac{1}{6}}\sigma \\ \frac{1}{2}\alpha\varepsilon\left[\cos\left(\gamma\left(\frac{r}{\sigma}\right)^2 + \beta\right) - 1\right] & \text{if} \quad 2^{\frac{1}{6}}\sigma < r \leq R_0\sigma \\ 0 & \text{otherwise} \end{cases} \tag{3.1}$$

with $\gamma = \pi\left(2.25 - 2^{\frac{1}{3}}\right)^{-1}$ and $\beta = 2\pi - 2.25\gamma$ [104]. The resulting effective attraction is controlled by the parameter $\alpha$, mimicking the solvent quality in an implicit way. The value $\alpha = 1$ describes a high attraction relative to the bead repulsion. Therefore, this value is used to describe poor solvent conditions and further to describe the fully collapsed state of the microgel. The fully swollen state of the microgel is described by the value $\alpha = 0$ (no attraction) as this describes good solvent conditions. The two extreme cases for the effective attraction strength $\alpha$ are set to $\alpha = 0$ for the fully swollen state and to $\alpha = 1$ for the fully collapsed state in the simulation. To map these values to a temperature regime, since the solvent quality in the experiment is determined by the temperature, $\alpha = 0$ can be assigned to the low temperature regime (below the volume phase transition) and $\alpha = 1$ to the high temperature regime. For a detailed mapping between the (experimental) temperature and the effective attraction strength $\alpha$ see Ref. [46]. Further, the internal architecture of a microgel can be described as in Ref. [71] with a crosslinker density of 4.5%. In our simulation we represent each microgel with a total number of $N = 5500$ beads.

Modelling the two interfaces, we follow Refs. [70,71], and add an external potential defined by an planar interface normal to the $z$-direction. The external potential for each bead is described by an effective Lennard-Jones part and a steep linear part. The former represents the water phase and the latter the oil phase. For the purpose of describing the interface, a typical range for the effective bead-interface interaction $\sigma_{\text{ext}}$ is introduced. Furthermore, at the matching point between the two parts $z_a > 0$, the potential-value and the derivative (force) of both potential parts are continuous. Explicitly, if the interface position is at $z = 0$ and the oil bulk phase is in the negative domain of the $z$-coordinate, the external interface potential is given by

$$V_{\text{ext}}(z) = \begin{cases} V_{\text{LJ}}(z) & z \geq z_a \\ V_{\text{LJ}}(z_a) + (z_a - z)\left.\frac{dV_{\text{LJ}}(z)}{dz}\right|_{z=z_a} & z < z_a \end{cases} \tag{3.2}$$

where $V_{\text{LJ}}(z)$ denotes the Lennard-Jones potential

$$V_{\text{LJ}}(z) = 4\varepsilon_{\text{ext}}\left[\left(\frac{\sigma_{\text{ext}}}{z}\right)^{12} - \left(\frac{\sigma_{\text{ext}}}{z}\right)^{6}\right], \tag{3.3}$$

with $\varepsilon_{\text{ext}}$ as attractive energy strength.

Obviously, the energetically favoured position for the beads is at the minimum of the interface potential at $z_{\text{min}} = 2^{\frac{1}{6}}\sigma_{\text{ext}}$. This corresponds physically to the effect of surface tension reduction by reducing the bare interface, through bead adsorption. In our modelling, $z_{min}$ is always larger than the matching point $z_a$. The assumed large difference in chemical potential between the oil and water phases is modelled by the steep increase in the potential for $z < z_a$. For $\varepsilon_{\text{ext}}$ we have set $\varepsilon_{\text{ext}} = 5.5\varepsilon$ to guarantee a strong adsorption towards the interface [71]. Further, $\sigma_{\text{ext}}$ is chosen as $\sigma_{\text{ext}} = 0.5\sigma$ to form a relatively peaked interface, as assumed in experiment. The matching point $z_a$ is slightly varied in our simulation and takes values between $1.110\sigma_{\text{ext}}$ and $1.115\sigma_{\text{ext}}$ to adjust the degree of softness of the interface potential. This leads to different fractions of the adsorbed beads in the water, respectively oil phase.

Whether a bead $i$ is in the water or oil phase is defined via its coordinate $z_i$. For $(z_i < z_{\text{min}})$, the bead is assumed to be in the oil phase, otherwise the bead $i$ is assumed to be in the water phase. Therefore, we define

$$p = \frac{1}{N} \sum_{i=1}^{N} \Theta\left(z_{\min} - z_i\right) \tag{3.4}$$

as the fraction of adsorbed beads in the oil phase, where $\Theta\left(z\right)$ denotes the unit step function. The total interfacial potential is given by the superposition of the two individual potentials at the corresponding shifted positions as $V_{\text{ext}}\left(z - \tilde{d}\right) + V_{\text{ext}}\left(-\left(z + \tilde{d}\right)\right)$ with $\tilde{d} = d/2$ as half of the interface distance, where we now assume that $z = 0$ corresponds to the middle of the slit.

Typically, in the experiments, microgel particles are densely packed across the interface with a structure resembling a hexagonal lattice. Hence each particle is laterally confined by its neighbours. We model this confinement by an approximate cylindrical confinement, the orientation of this effective cylindrical Wigner-Seitz cell is normal to the two interfaces and its radius should scale with the bulk radius of gyration $R_g$ of a single microgel. Therefore we again employ a radial softened potential for the beads describing their confinement in the Wigner-Seitz cell given by

$$V_{\text{c}}\left(r\right) = \begin{cases} 4\varepsilon_c \left[\left(\frac{R_g}{R_c - r}\right)^{12} - \left(\frac{R_g}{R_c - r}\right)^{6}\right] - \left(R_c - r - R_g\right) \left.\frac{\partial V(r)}{\partial r}\right|_{R_c - r = R_g} & \text{if}\, R_c - r \leq R_g \\ 0 & \text{otherwise} \end{cases} \tag{3.5}$$

Here $r$ is the radial distance between the cylinder and a bead, $R_c = 2R_g$ with $R_g = 20\sigma$ is the bulk radius of gyration [71] and the typical range of the effective bead-cell interaction. $\varepsilon_c = 5\varepsilon$ is the typical strength of repulsion.

As in Ref. [71], the bead motion is simulated by Brownian dynamics, implying an implicit solvent. The short time self-diffusion coefficient $D_0$ defines the Brownian time scale $\tau_{\text{B}} = D_0/\sigma^2$, which describes the time unit in our simulation. Using a finite time step of $\Delta t = 0.00009\tau_{\text{B}}$, the equations of motion are integrated by an Euler forward scheme. All of the Brownian dynamics simulations are performed with the HOOMD-Blue package [110] and are visualized by OVITO [112]. It is important to note that the solvent bath temperature $T^*$, which is responsible for the Brownian fluctuations, and the implicit temperature influence of the effective attraction strength $\alpha$ are different. The solvent bath temperature is fixed at $k_{\text{B}}T^* = \varepsilon$ and the effective attraction strength $\alpha$ is changed. This is justified because the temperature changes are small compared to the absolute room temperature. Further, for simplicity, the interaction of the beads in the interface and in the bulk is the same.

The simulation protocol is as follows: First, for $\alpha = 0$, $N_m = 1$ or $N_m = 2$ microgels are equilibrated in the fully swollen state in the cylinder mimicking the Wigner-Seitz cell but in the absence of the two interfaces. Note that the effective repulsive length of the cylinder $R_c = 2R_g$ is larger than the radius of gyration in the bulk and therefore there is no significant structural change of the microgel compared to the bulk. For $N_m = 2$ the two microgels have a distance along the cylinder axis which is large enough such that they are not interacting with each other. Then the external potential $V_{\text{ext}}\left(z - \tilde{d}\right) + V_{\text{ext}}\left(-\left(z + \tilde{d}\right)\right)$ is turned on at a large distance $d$ comprising the microgels and avoiding any interfacial contact with monomers. Then the interface distance is gradually decreased in small steps of $\Delta d = 4\sigma$. For each new distance $d$, the system is equilibrated again for a typical time $300\tau_{\text{B}}$ and then statistics is taken within a time window of $600\tau_{\text{B}}$. For $\alpha = 1$, we start from a swollen configuration obtained at $\alpha = 0$ and first increased $\alpha$ stepwise with a small increment. Then the resulting configuration is exposed to a shrinking interface distance. Here we have used $\Delta d = 2\sigma$.

The osmotic pressure $\Pi$ exerted by the microgels on the interfaces is the mean force between all beads $i$ divided by the area of the Wigner-Seitz cell $\pi R_c^2$

$$\Pi = \frac{1}{\pi R_c^2}\left(-\sum_{i=1}^{N}\left\langle \left.\frac{dV_{\text{ext}}}{dz}\right|_{z=z_i-\tilde{d}}\right\rangle\right), \tag{3.6}$$

where $\langle \ldots \rangle$ denotes the time average.

While for $N_m = 1$ the mean center of the microgel is in the middle of the slit due to symmetry, for $N_m = 2$ the mean distance between the two microgel centers $\Delta_z$ is another nontrivial variable which we calculated by averaging the $z$-coordinates of all beads of a single microgel as

$$\Delta_z = \frac{2}{N}\left|\left\langle \sum_{i=1}^{N} z_i \right\rangle\right| \tag{3.7}$$

exploiting the bead symmetry in $z$.

### 3.1.2 Results and Discussion

Figure 3.1 shows the osmotic disjoining pressure $\Pi$ acting on the interfaces as a function of the interfacial distance $d$ for one (purple symbols) and two adsorbed microgels (yellow symbols), both in the fully collapsed state (Figure 3.1a)) and in the fully swollen state (Figure 3.1b)). The data are plotted for different fractions of the adsorbed beads $p$ in the oil phase obtained at the initial distance $16\sigma$ for the fully collapsed state and $d = 34\sigma$ for the fully swollen state. Corresponding typical snapshots are also presented.

For the fully collapsed state (Figure 3.1a)), a single confined microgel induces an *attraction* between the two interfaces which becomes significant at small distances. The attraction between the interfaces and the single microgel acts as a linking agent which tends to bring the interfaces closer together. Interestingly, in contrast, two confined microgels induce a *repulsion* which becomes more pronounced for decreasing interface separations $d$. Here the bead density is intermediate such that interbead repulsions dominate and the squeezed microgel pair exerts repulsive forces to the interface. For extremely narrow slits the repulsion strength weakens if the number of beads adsorbed in the oil phase is large. The latter effect can be attributed to the increased bead-bead attractions at high local densities which mediate a reduced osmotic pressure.

In the fully swollen state ($\alpha = 0$), there is pure repulsion between the beads which always leads to an interfacial repulsion, as documented by a positive osmotic pressure $\Pi$ in Figure 3.1b). Clearly the repulsion increases with decreasing distance $d$. As expected, an ”escape” of beads into the oil phase (as documented by larger fractions $p$), results in a reduction of the repulsion.

The mean distance between the microgel pair $\Delta_z$ is shown in Figure 3.2 as a function of the interface separation $d$ for the fully collapsed (red symbols) and fully swollen state (blue symbols). As the value $d/3$ serves as a simple approximation of the mean distance $\Delta_z$ between the microgel pair for the distance $d$, this function is plotted and compared with the data. For all distances $d$ the mean distance $\Delta_z$ is larger than $d/3$, reflecting the effect of the strong adsorption of the microgels to the exposed interfaces and the repulsive interaction between two microgels. The mean distance $\Delta_z$ for the fully collapsed state ($\alpha = 1$) is larger than those for the fully swollen state ($\alpha = 0$) for all distances $d$ and fractions $p$. This results from the additional attraction to the interface induced by the attractive adsorbed beads.

Finally the dependence on the fraction $p$ is more pronounced in the collapsed state as compared to that in the swollen state.

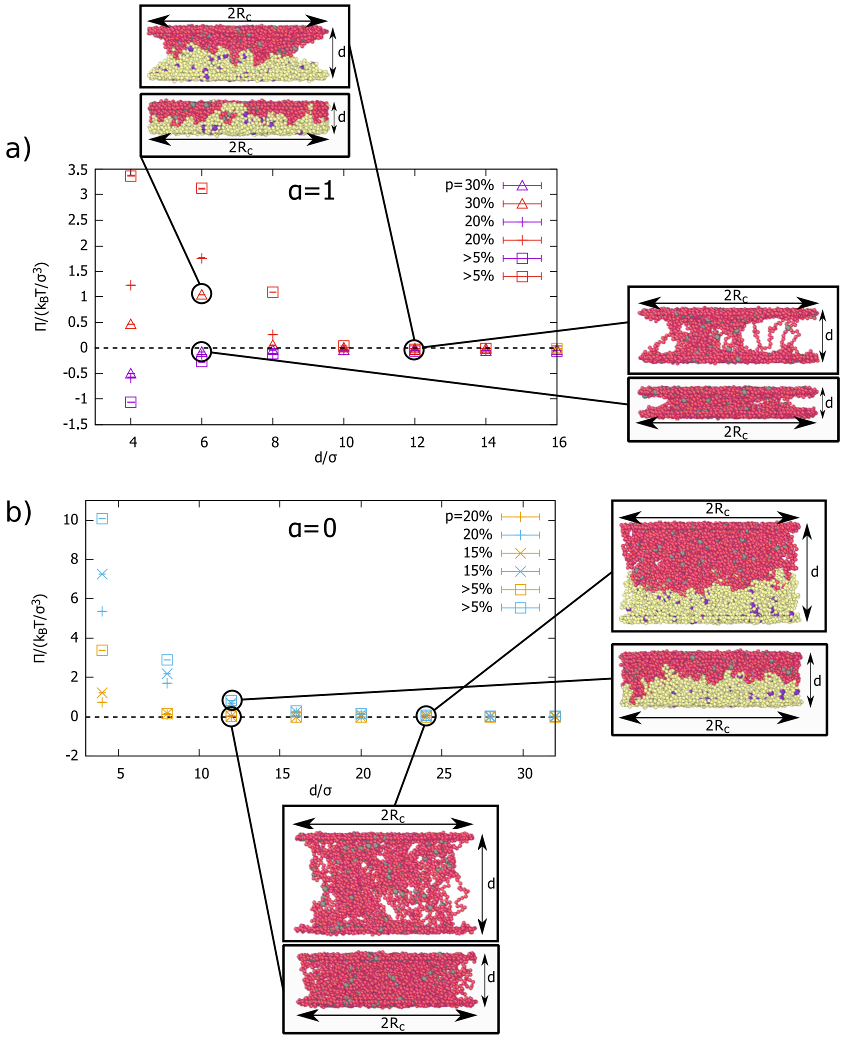

Figure 3.1: Osmotic pressure $\Pi$ in units of $k_\mathrm{B}T/\sigma^3$ of one ($N_m = 1$, purple or yellow symbols) and two adsorbed microgels ($N_m = 2$, red or blue symbols) in the fully collapsed state ($\alpha = 1$) a) and in the fully swollen state ($\alpha = 0$) b) as a function of the distance $d$ between the two interfaces. The data are plotted for different fractions $p$ of the adsorbed beads in the oil phase (different symbols) taken at an initial interface distance of $d = 16\sigma$ for the fully collapsed state and $d = 34\sigma$ for the fully swollen state. Four typical snapshots (side views) are shown for the fractions of $p = 30\%$ for the fully collapsed state a) and four typical snapshots are shown for fractions of $p = 20\%$ for the fully swollen state b). In the snapshots, the red/yellow beads are monomers and the grey/purple beads are the crosslinkers within the microgel.

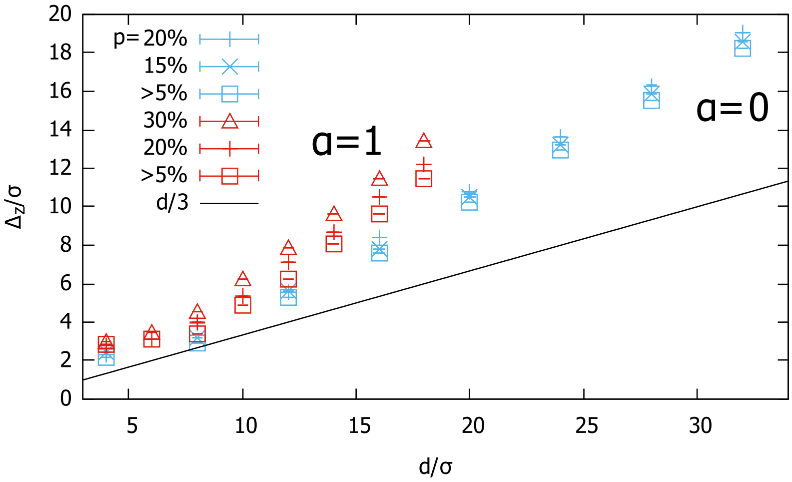

Figure 3.2: Mean distance $\Delta_z$ between the two microgel centers ($N_m = 2$) in the collapsed ($\alpha = 1$, red) and swollen state ($\alpha = 0$, blue) as a function of the distance $d$ (errorbars included) and for different fractions $p$ of the adsorbed beads in the oil phase (different symbols) as in Figure 3.1. For comparison the function $d/3$ is plotted, since this represents a simple approximation of the distance between the two centers of the microgels.

### 3.1.3 Supporting Information

For a modelling of the repulsive bead-bead interaction a Weeks-Chandler-Andersen [100] potential is used

$$V_{\mathrm{WCA}}\left(r\right) = \begin{cases} 4\varepsilon\left[\left(\frac{\sigma}{r}\right)^{12} - \left(\frac{\sigma}{r}\right)^{6}\right] + \varepsilon & \text{if} \qquad r \leq 2^{\frac{1}{6}}\sigma \\ 0 & \text{otherwise} \end{cases} \tag{3.8}$$

with $r$ as the radial distance between two beads, $\sigma$ as the bead diameter and $\epsilon$ as the strength of repulsion. The modelling of the bead-connecting covalent bonds a finite-extensible-nonlinear-elastic (FENE) [46, 77] potential is used.

$$V_{\mathrm{FENE}}\left(r\right) = \begin{cases} -\tilde{k}_{\mathrm{F}}\tilde{R}_0^2 \ln\left(1 - \left(\frac{r}{\tilde{R}_0}\right)^2\right) & \text{if} \qquad r < \tilde{R}_0 \\ 0 & \text{otherwise} \end{cases} \tag{3.9}$$

where $\tilde{k}_{\mathrm{F}} = 15\varepsilon/\sigma^2$ is an effective spring constant and $\tilde{R}_0 = 1.5\sigma$ the maximal bond expansion.

## 3.2 Hairy particles at interfaces

### Statement of contribution

Hartmut Löwen, and I developed the theory/idea. I performed the numerical evaluations and prepared the data and figures. HL and I wrote the manuscript.

### 3.2.1 Materials and Methods

In the following, we model both a single and a pair of hairy particles ($N_h = 1, 2$) adsorbed at a planar oil-water interface. Through the adsorption, the hairy particles form a corona of radius $R_{\mathrm{co}}$ in the interface around their finite hard cores of radius $R_{\mathrm{c}}$. For a single hairy particle ($N_h = 1$) we vary the distance $z$ between the center of the core and the interface and calculate the effective interaction potential between the particle and the interface. For a pair of hairy particles ($N_h = 2$) we change the lateral distance $r$ between the two particles centres at fixed distance $z$ for both particles, and calculate the effective interaction potential between the two particles as a function of $r$. In Figure 3.3, a schematic illustration of the simulation set-up for two hairy particles is shown. Furthermore we extract typical simulation snapshots for one and two hairy particles.

In our model, a hairy particle consists of a spherical core with anchor points on the surface and linear polymer strands that are covalently bound to these anchor points. The polymer chains themselves consist of covalently bound beads. Inside each linear polymer chain a bead has two neighbouring beads, while the first bead has only one neighbour and is linked to its anchor point on the core surface. The bead-bead and anchor point-bead interactions are modelled by a repulsive Week-Chandler-Anderson (WCA) potential involving a typical bead diameter $\sigma$ as a length scale and a typical repulsion energy scale $\epsilon$, see SI (3.2.3). The covalent bonds between the beads and anchor points are described by a finite-extensible-nonlinear-elastic (FENE) potential with the same characteristic energy scale $\varepsilon$, a maximum bond length $R_0 = 1.5\sigma$ and an effective spring constant $k_f = 15\varepsilon/\sigma^2$, see SI (3.2.3). The core-bead interaction is described via a repulsive WCA potential involving the core-bead distance, see SI (3.2.3).

The fixed positions of $N_a$ anchor points on the surface of the core are generated by a Fibonacci lattice as described in Ref. [113, 114] and are labelled by an integer $j$, ($j = 1, \dots, N_a$). Their solid angles are given in spherical coordinates by

$$\theta_j = 2\pi j \frac{2}{1+\sqrt{5}} \tag{3.10}$$

$$\phi_j = \arccos\left(1 - 2\frac{j+0.5}{N_a}\right). \tag{3.11}$$

We choose $N_a = 100$ as the total number of anchor points and the bead number per chain to 50, so that the total number of beads of a single hairy particle is $N = 5000$.

The interface is modelled as an external potential [71] $V_{\mathrm{ext}}(z)$ for the beads. It is given as a superposition of two attractive WCA potentials which possess mirrored and shifted arguments as shown in Figure 3.4. In detail, the external potential is

$$V_{\mathrm{ext}}(z) = \varepsilon_{\mathrm{w}} f\left(-\left(z - z_{\mathrm{min}}\right)\right) + \varepsilon_{\mathrm{o}} f\left(z + z_{\mathrm{min}}\right) \tag{3.12}$$

with a dimensionless function

$$f\left(z\right)=\begin{cases}4\left[\left(\frac{\sigma_{\text{ext}}}{z}\right)^{12}-\left(\frac{\sigma_{\text{ext}}}{z}\right)^{6}\right]+1 & z\geq z_{\text{min}}\\ 0 & z<z_{\text{min}},\end{cases} \tag{3.13}$$

where $\sigma_{\text{ext}}$ denotes a typical range of the effective bead-interface interaction, $z_{\text{min}} = 2^{\frac{1}{6}}\sigma_{\text{ext}}$ is the minimum of $f(z)$, $\varepsilon_{\text{o}}$ resp. $\varepsilon_{\text{w}}$ is the chemical potential of the beads in bulk oil resp. water. At $z = 0$ the external potential exhibits a sharp minimum reflecting the bare surface tension reduction at the interface through bead adsorption. For our calculations we choose $\varepsilon_{\text{o}} = 2\varepsilon_{\text{w}} = 11\varepsilon$ and $\sigma_{\text{ext}} = 0.5\sigma$.

The interaction between the core and the interface is obtained from a thermodynamic consideration that involves the gain of the surface free energy in the presence of the core. At a given core distance $z$ to the interface, the core cuts out a circular area of the bare oil-water interface. This corresponds to a free energy gain of $\gamma\pi\left(R_{\text{c}}^{2}-z^{2}\right)$, where $\gamma$ is the surface tension of the free oil-water interface. By scaling we obtain $\gamma = \varepsilon_{\text{w}}/(\sigma^{2}\pi/4)$. Therefore the core-interface interaction potential is given by

$$V_{\text{int}}^{(1)}(z)=\begin{cases}-\gamma\pi\left(R_{c}^{2}-z^{2}\right) & z\leq R_{c}\\ 0 & z>R_{c}\end{cases} \tag{3.14}$$

and the core interface force $F_{\text{int}}^{(1)}$ is

$$F_{\text{int}}^{(1)}(z)=-\frac{\partial V_{\text{int}}^{(1)}(z)}{\partial z}=\begin{cases}-2\gamma\pi z & z\leq R_{c}\\ 0 & z>R_{c}.\end{cases} \tag{3.15}$$

As in Ref. [71], the bead motion is simulated by Brownian dynamics governed by a short-time bead self-diffusion coefficient $D_0$, which defines the Brownian time scale $\tau_B = D_0/\sigma^2$. With a finite time step of $\Delta t = 0.00005\tau_B$, the equations of motion are integrated using a forward Euler method. All of the Brownian dynamics simulations are performed with the Hoomd-Blue package [110] and visualized by OVITO [112]. The solvent bath temperature $T^*$ is set to $T^* = \varepsilon/k_{\text{B}}$.

The simulation protocol is as follows: First, within a time interval of $500\tau_{\text{B}}$, the beads of the hairy particles are equilibrated in the absence of the interface potential (bulk); for two particles $N_h = 2$ this is done with a fixed large lateral distance of $r = 100\sigma$ between the centres. In the second step, the interface potential is switched on instantaneously, at a fixed core distance $z = R_{\text{c}}$. In this configuration, the beads of the hairy particles $N_h = 1, 2$ are also equilibrated for $500\tau_{\text{B}}$. The distance $z$ is slowly reduced to 0 to determine the equilibrium distance $z^*$ where the $z$-component of the effective mean force is vanishing. Different equilibrium distances $z^*$ correspond to different contact angles of the hairy particle in the

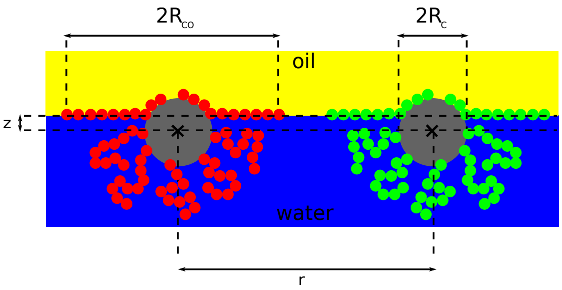

Figure 3.3: Schematic illustration of the simulation set-up for two hairy particles, with the distance $z$ of the two particles to the oil-water interface, the lateral distance $r$ between the two particles, the radius of the corona $R_{\text{co}}$ formed by the interface and the core radius $R_{\text{c}}$.

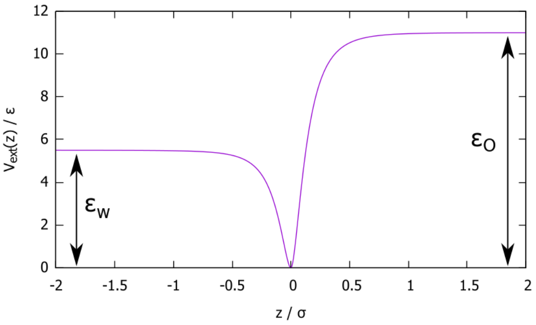

Figure 3.4: Interface potential $V_{\text{ext}}(z)$ in units of $\varepsilon$ for the choice of the characteristic parameters $\varepsilon_{\text{o}} = 2\varepsilon_{\text{w}} = 11\varepsilon$ and $\sigma_{\text{ext}} = 0.5\sigma$.

interface. Then at fixed equilibrium distance $z^*$ the lateral distance $r$ is reduced stepwise with a step-size $\Delta r = 4\sigma$ and an equilibration time of $250k_BT$. Statistics is taken within a time interval of $500\tau_B$. For comparison the same protocol is applied in the corresponding bulk situation.

For a single hairy particle at a distance $z$ to the interface, the total mean force $F_{\text{eff}}^{(1)}(z)$ exerted by the interface on the core involves a canonical average over the bead positions on top of the direct core-interface interaction, see SI. The effective core-interface potential is obtained by integration, $V_{\text{eff}}^{(1)}(z) = \int_z^\infty dz' F_{\text{eff}}^{(1)}(z')$. The equilibrium distance $z^*$ is determined by the condition $F_{\text{eff}}^{(1)}(z^*) = 0$. Two hairy particles, at the same core interface distance $z^*$ and at a lateral distance $r$, interact with a lateral effective interaction potential $V_{\text{eff}}^{(2)}(r) = \int_r^\infty dr' F_{\text{eff}}^{(2)}(r')$, with the total mean force $F_{\text{eff}}^{(2)}(r)$. The latter involves again a canonical bead average, see SI.

The effective interaction potential $V_{\text{eff}}^{(2)}(r)$ is fitted with two potentials. The first is a general Jagla-potential [83]

$$U_{\mathrm{J}}(r) = \begin{cases} \infty & r < R_{\mathrm{c,eff}} \\ U_0 \frac{g + \left( \left( \frac{r/R_{\mathrm{c,eff}} - 1}{R_{\mathrm{co}}/R_{\mathrm{c,eff}} - 1} \right) (g - g^{-1}) - g \right)^{-1}}{g - g^{-1}} & R_{\mathrm{c,eff}} \leq r \leq R_{\mathrm{co}} \\ 0 & r > R_{\mathrm{co}} \end{cases} \tag{3.16}$$

where $R_{\mathrm{c,eff}}$ is an effective core radius and $R_{\mathrm{co}}$ is the corona radius. The two fit-parameters are the softness $g$ which controls the penetrability of the interaction and the amplitude $U_0$. The second potential is known from the star polymers [84–86] and has the following form,

$$U_{\mathrm{S}}(r) = \begin{cases} \frac{5}{18} f^{\frac{3}{2}} \left[ -\ln\left( \frac{r}{R_{\mathrm{co}}} \right) - \left( 1 + \frac{\sqrt{f}}{2} \right)^{-1} \right] & r \leq R_{\mathrm{co}} \\ \frac{5}{18} f^{\frac{3}{2}} \left( 1 + \frac{\sqrt{f}}{2} \right)^{-1} \frac{R_{\mathrm{co}}}{r} \exp\left[ -\frac{\sqrt{f}(r - R_{\mathrm{co}})}{2R_{\mathrm{co}}} \right] & r > R_{\mathrm{co}} \end{cases} \tag{3.17}$$

where $f$ is the number of arms. For this potential $R_{\mathrm{co}}$ and $f$ are fit parameters.

### 3.2.2 Results and Discussion

Figure 3.5 shows the effective core-interface potential $V_{\mathrm{eff}}^{(1)}(z)$ as a function of the distance $z$. A quadratic function $az^2 + bz + c$ is fitted to the data set with the fit parameters $a = 4210 k_B T/R_{\mathrm{c}}^2 \pm 50 k_B T/R_{\mathrm{c}}^2$, $b = -5320 k_B T/R_{\mathrm{c}} \pm 70 k_B T/R_{\mathrm{c}}$ and $c = 650 k_B T \pm 20 k_B T$. The minimum of the fit is at $z = 0.6 R_{\mathrm{c}}$, suggesting an equilibrium distance close to $z^* = 0.5 R_{\mathrm{c}}$. For the equilibrium distance $z^*$, the following effective potential $V_{\mathrm{eff}}^{(2)}(r)$ results from a variation of the lateral distance $r$.

Figure 3.6 shows the lateral effective interaction potential $V_{\mathrm{eff}}^{(2)}(r)$ as a function of the lateral distance $r$. The interaction is purely repulsive as the polymer strands try to avoid each other, hence the system drives the cores of the hairy particles apart (from each other). To fit the Jagla potential, an effective core radius $R_{\mathrm{c,eff}} = 34\sigma$ is assumed. This corresponds to the radius of gyration of a hairy particle with collapsed shell/corona in the bulk configuration. In this way, a configuration/packing can be estimated for which the neglect of the many-body interaction is no longer sufficient.

For the data set in figure 3.6, three regimes can be estimated for the lateral effective interaction potential $V_{\mathrm{eff}}^{(2)}(r)$, a compressed regime $(46\sigma - 58\sigma)$ where the corona is close to the collapsed reference state, a more diluted regime $(60\sigma - 70\sigma)$ where the coronae begin to overlap, and a fuzzy regime $(74\sigma - 86\sigma)$ where the two coronae slightly touch. Furthermore, only the first two regimes are considered for the fit with the Jagla potential, because the Jagla potential predicts a cusp at the corona radius and since the corona consists of a discrete number of polymer strands, such

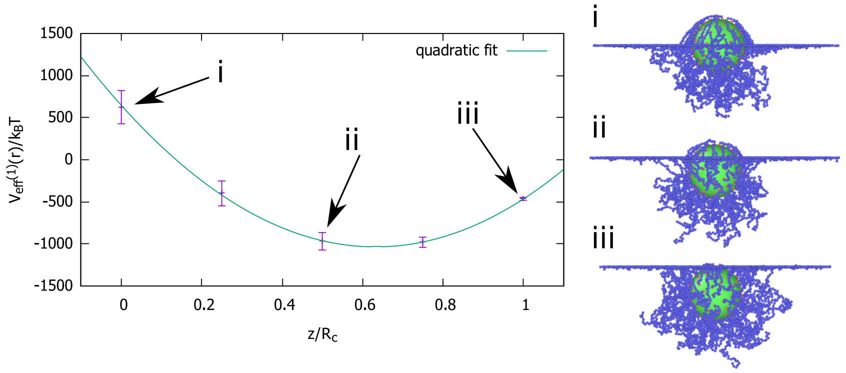

Figure 3.5: Effective interaction potential $V_{\text{eff}}^{(1)}(z)$ in units of $k_BT$ as a function of the distance between the centre of the core and the interface $z$. A quadratic function $az^2+bz+c$ is fitted to this data points, with the fit-parameters $a = 4210k_BT/R_\text{c}^2 \pm 50k_BT/R_\text{c}^2$, $b = -5320k_BT/R_\text{c} \pm 70k_BT/R_\text{c}$ and $c = 650k_BT \pm 20k_BT$

a cusp-like shape cannot be achieved. Therefore, the fuzzy region must be excluded from the fit and a pre-selection of the data points to which the Jagla potential is to be fitted must be made. For the data points from $46\sigma$ to $58\sigma$ (compressed regime), three fit parameters, the corona radius $R_\text{co}$, the amplitude $U_0$ and the softness $g$, are calculated, $R_\text{co} = 72\sigma \pm 2\sigma$, $U_0 = 2200k_BT \pm 100k_BT$ and $g = 0.72 \pm 0.06$ ('Jagla 1', green line). By taking into account the calculated fit parameter of the corona radius of about $72\sigma$, $R_\text{co}$ is used as input parameter in the following. For the compressed regime ($46\sigma - 58\sigma$), the two input parameters $R_\text{c,eff} = 34\sigma$ and $R_\text{co} = 70\sigma$ give the values $U_0 = 1990k_BT \pm 60k_BT$ and $g = 0.83 \pm 0.02$ ('Jagla 2', blue line), see figure 3.6. The more diluted range ($60\sigma - 70\sigma$) is served by the input parameters $R_\text{c,eff} = 34\sigma$ and $R_\text{co} = 76\sigma$. There the fitting yields the values $U_0 = 1200k_BT \pm 200k_BT$ and $g = 0.9 \pm 0.1$ ('Jagla 3', orange line), see figure 3.6. No Jagla fit is given for the fuzzy regime, as this leads to an unphysical estimate of the potential.

The star polymer potential on the other hand assumes a Yukawa-like decrease with the decay length of the outermost blob size in the fuzzy regime. Moreover, this potential assumes a point core, so the only fitting parameters are the corona radius $R_\text{co}$ and the number of chains $f$. Taking all three regimes together, the fitting yields the parameters $R_\text{co} = 68.2\sigma \pm 0.4\sigma$ and $f = 400 \pm 10$ ('star polymer', yellow line). The corona radius is in the same range as the corona radius of the Jagla fit, while the number of arms $f$ is in the same order of magnitude as the input number $N_a$. The difference in the number of arms, respectively anchor-points $N_a$, can be explained by the finite extension of the core, which is different from the star polymer potential assumption.

The corona radii resulting from the different fitting functions, $72\sigma$ for the Jagla

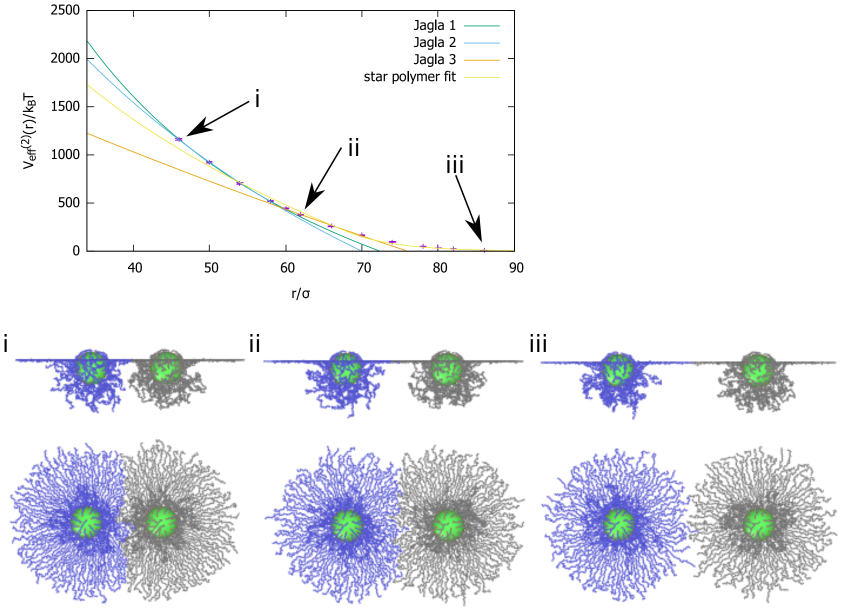

Figure 3.6: Effective interaction potential $V_{\text{eff}}^{(2)}(r)$ in units of $k_BT$ as a function of the distance between the centres of the cores $r$ with different fits of the two potentials $U_J(r)$ and $U_S(r)$. For the three different fits of the Jagla potential the an effective core radius is set to $R_{\text{c}} = 34\sigma$ and the corona radius to $R_{\text{co}} = 70\sigma$ for the fit labelled as 'Jagla 2' and to $R_{\text{co}} = 76\sigma$ for the fit labelled as 'Jagla 3'. The fit-parameters and ranges of the data set are, 'Jagla 1' (green): $(46\sigma - 58\sigma), R_{\text{co}} = 72\sigma \pm 2\sigma, U_0 = 2200k_BT \pm 100k_BT$ and $g = 0.72 \pm 0.06$, 'Jagla 2' (blue): $(46\sigma - 58\sigma), U_0 = 1990k_BT \pm 60k_BT$ and $g = 0.83 \pm 0.02$, 'Jagla 3' (orange): $(60\sigma - 70\sigma), U_0 = 1200k_BT \pm 200k_BT$ and $g = 0.95 \pm 0.1$. The fit-parameters from the star polymer potential (yellow) are $R_{\text{co}} = 68.2 \pm 0.4$ and $f = 400 \pm 10$

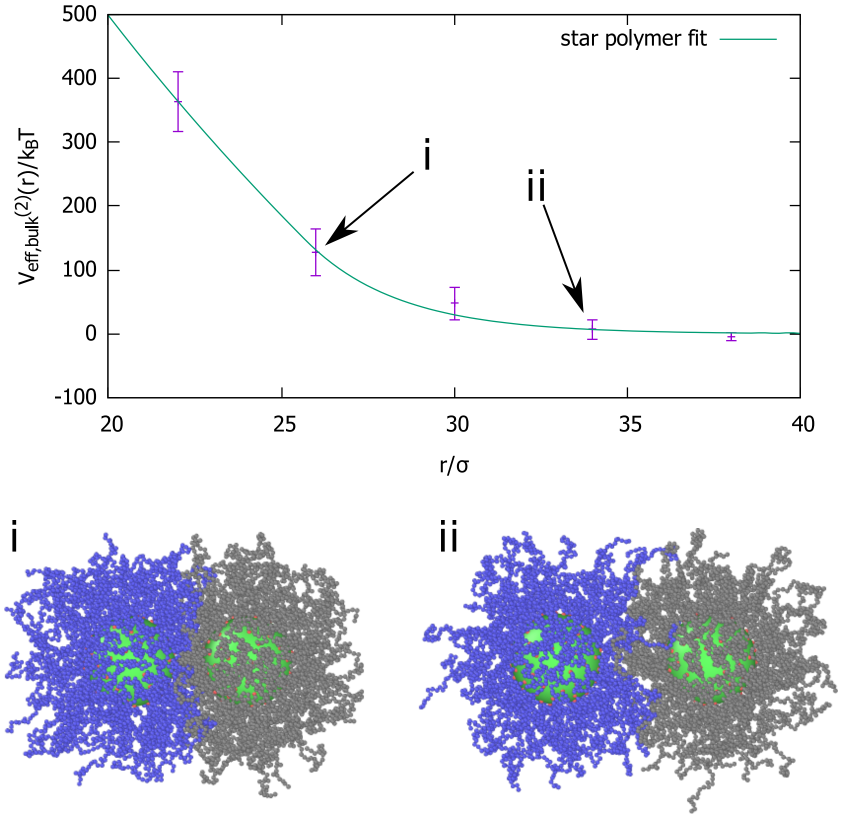

Figure 3.7: Effective interaction potential in bulk $V^{(2)}_{\text{eff,bulk}}(r)$ in units of $k_BT$ as a function of the distance between the centres of the cores $r$. The function $U_S(r)$ is fitted to the data, with the fit-parameters $R_{\text{co}} = 25.7\sigma \pm 0.8\sigma$ and $f = 290 \pm 40$.

potential $U_J(r)$ and $68\sigma$ for the star polymer potential $U_S(r)$, give a ratio of the pure core radius and the corona of 1 : 3.5. As a further comparison, the bulk interactions are also considered for different lateral distances $r$ of two hairy particles. Figure 3.7 shows the data for this case. In addition, a fit of the star polymer potential $U_S(r)$ with the fit parameters $R_{\mathrm{co}} = 25.7\sigma \pm 0.8\sigma$ and $f = 290 \pm 40$ is given.

### 3.2.3 Supporting Information

A repulsive Weeks-Chandler-Andersen [100] potential serves as a model for the bead-bead and bead-anchor point interaction

$$V_{\mathrm{WCA}}\left(r\right) = \begin{cases} 4\varepsilon\left[\left(\frac{\sigma}{r}\right)^{12} - \left(\frac{\sigma}{r}\right)^{6}\right] + \varepsilon & \text{if} \qquad r \leq 2^{\frac{1}{6}}\sigma \\ 0 & \text{otherwise} \end{cases} \tag{3.18}$$

where $\sigma$ is the bead diameter and $\epsilon$ is the strength of repulsion.

The finite-extensible-nonlinear-elastic (FENE) [46, 77] potential for the covalent bonds is given by

$$V_{\mathrm{FENE}}\left(r\right) = \begin{cases} -\tilde{k}_{\mathrm{F}}\tilde{R}_0^2 \ln\left(1 - \left(\frac{r}{\tilde{R}_0}\right)^2\right) & \text{if} \qquad r < \tilde{R}_0 \\ 0 & \text{otherwise} \end{cases} \tag{3.19}$$

where $\tilde{k}_{\mathrm{F}} = 15\varepsilon/\sigma^2$ is an effective spring constant and $\tilde{R}_0 = 1.5\sigma$ the maximal bond expansion.

Radially outwards, the core-bead interaction is modelled by a repulsive WCA potential

$$V_{\mathrm{c}}\left(r\right) = \begin{cases} 4\varepsilon_c\left[\left(\frac{\sigma}{R_c - r}\right)^{12} - \left(\frac{\sigma}{R_c - r}\right)^{6}\right] + \varepsilon_c & \text{if} \qquad R_c - r \leq 2^{\frac{1}{6}}\sigma \\ 0 & \text{otherwise} \end{cases} \tag{3.20}$$

where the core radius is $R_{\mathrm{c}} = 10\sigma$ and the energy scale $\varepsilon_{\mathrm{c}} = 50\varepsilon$.

The total effective core-interface interaction force is $F^{(1)}_{\mathrm{eff}}(z) = F^{(1)}_{\mathrm{int}}(z) + F^{(1)}_{\mathrm{bead}}(z)$ with

$$F^{(1)}_{\mathrm{bead}}(z) = \sum_{i=1}^{N} \left\langle \frac{dV_{\mathrm{ext}}(z_i)}{dz_i} \right\rangle \tag{3.21}$$

where the index $i$ labels the beads, $z_i$ is the distance of the $i$th bead to the interface and $\langle \dots \rangle$ denotes a canonical or time average. The sign in Eq. (3.21) is reversed by Newton's third law as applied to the interface and the hairy particle.

Finally, the effective interaction force between two hairy particles is given by

$$\mathbf{F}_{\text{eff}}^{(2)}(r) = -\sum_{i=1}^{2N} \left\langle \frac{\partial V_c\left(\left|\mathbf{R}_c^{(1)} - \mathbf{r}_i\right|\right)}{\partial \mathbf{r}_i} \right\rangle \tag{3.22}$$

where the sum runs over all $2N$ beads at positions $\mathbf{r}_i$ and $\mathbf{R}_c^{(1)} = (0, 0, z^*)$ is the position of one hairy particle core. The average is taken under the condition that the second hairy particle core is fixed at $\mathbf{R}_c^{(2)} = (0, r, z^*)$.

# Chapter 4

# Concluding Remarks

Soft core-shell materials, such as polymer-grafted cores (hairy particles) or microgels, offer a wide range of applications and fundamental effects at fluid interfaces. One aspect of this thesis was to investigate the elastic deformations of a coarse-grained core-shell system with a coupled architecture at a fluid interface in general. For this purpose, the response of the elastic material to an interfacial loading effect was investigated for different degrees of stiffness and sizes of the core and shell. Furthermore, for different degrees of auxetic behaviour, the deformation of the system was classified. In addition, the stress field gives a detailed insight into the deformation behaviour of the core-shell system and reveals the inhomogeneity of the stress level within the system. The deformation of a core-shell particle in an (equatorial) interface confinement is therefore a fundamental quantity and can be tuned by different elastic properties.

Another aspect of this thesis was the investigation of polymeric structured matter at fluid interfaces. Due to the strong influence of the interface, new formations such as a corona are formed at the interface. Specifically for a polymer-grafted core, the effective core-interface interaction was investigated, resulting in an equilibrium distance of the polymer-grafted core (hairy particle) to the interface. The pair interaction at the interface induced by the coronae was also investigated (under good solvent conditions) and found to be purely repulsive. A similar investigation for the situation for the polymer grafted cores in the bulk also revealed a repulsive interaction. In addition, the pair interaction was compared with established pair interactions such as the Jagla or star polymer pair interaction to determine effective quantities such as the effective corona and core radius or the degree of softness of the Jagla approach.

In addition, polymeric materials are very sensitive to the solvent conditions in which the materials are dissolved. The phenomena that occur for different solvent conditions in combination with an interface range from core hysteresis during volume phase transition of a microgel adsorbed at a fluid interface (single-body system) to different induced osmotic pressures within a slit-like configuration of two interfaces with different packing fractions of the adsorbed microgels (many-body system).

For core-hysteresis (induced by the fluid interface), two different solvent states were considered for adsorption at the interface, an adsorption in poor (collapsed state) and in good solvent condition (swollen state). After adsorption, a change of conditions was made from poor to good solvent conditions and vice versa. The lateral expansion of the microgel at the interface provides a significant difference for this protocol (after the processes) compared to the initial state for these conditions. This comparison of lateral expansion in good and poor conditions before and after a change in solvent quality was also performed in the corresponding bulk situation where no difference was found between the initial and final states. For a microgel adsorbed in a poor solvent, passing through a whole cycle of solvent quality changes, a hysteresis in lateral expansion and surface pressure is found. The hysteresis was also investigated for different degrees of crosslinking, revealing that a greater hysteresis is achieved for a lower degree of crosslinking. Such behaviour is the result of the initial adsorbed microgel under poor conditions, which is presumably some kind of kinetically trapped state. Much longer times for the cycle of solvent quality changes observe the same amount of core-hysteresis.

In the slit-like interfacial system filled with microgels (many-body system), the microgels naturally relax in their adsorbed position. The pair interaction between the interfaces was then quantified by the effective osmotic pressure for different distances between the two interfaces. Both, a positive and negative osmotic pressure was found for small interfacial distances in good or poor solvent conditions and for a dense or (more) diluted microgel packing. A negative pressure was induced in poor solvent conditions for a diluted packing, and a repulsive pressure was found in all other situations.

In summary, core-shell particles at fluid interfaces add to the wide variety of different bulk phenomena and effects, and offer (in general or in particular) a wide range from basic effects such as hysteresis and inhomogeneous deformation/stress behaviour to application-related effects such as induced interactions between cores or interfaces. A natural addition would be a more detailed consideration of the surface tensions between the two interfacial immiscible fluids and the core-shell systems adsorbed at the interface in the theoretical description. This could be used to systematically adjust the contact angle and thus the penetration depth between each of the two fluids and the core-shell system and thus approach a better comparison with the experiments.

In a further step, even the interface itself could be modelled as a solvent-resolved set-up [77]. In this way, dynamic interface-forming effects could be taken into account. For the core-hysteresis of the microgel and the effect of corona formation occurring at the interface, an explicit solvent-resolved interface could have significant effects on these phenomena. For the coarse-grained description of general core-shell systems at interfaces, plastic deformations could be considered [87]. For this purpose, a quasi-static description is suitable, especially from a methodological point of view, which is extended to plastic deformations in addition to elastic deformations.

Miekle at al. [115–117] provides an elegant formalism for the inclusion of pure (quasi-static) plastic deformations in the framework of linear elasticity theory and thus offers the possibility to investigate quasi-static non-equilibrium effects, such as a hysteresis in the lateral deformation of a core-shell system.

# References

[1] F. Caruso, *Nanoengineering of Particle Surfaces*, Advanced Materials **13**, 11 (2001).

[2] W. Schärtl, *Current directions in core–shell nanoparticle design*, Nanoscale **2**, 829 (2010).

[3] P. N. Pusey, in *Liquids, Freezing and the Glass Transition* (edited by J. P. Hansen, D. Levesque and J. Zinn-Justin, Amsterdam, North-Holland, 1991).

[4] H. N. Lekkerkerker and R. Tuinier, in *Colloids and the Depletion Interaction* (Springer, Dordrecht, 2011).

[5] C. P. Royall, W. C. K. Poon, and E. R. Weeks, *In search of colloidal hard spheres*, Soft Matter **9**, 17 (2013).

[6] S. Förster, V. Abetz, and A. H. E. Müller. *Polyelectrolyte Block Copolymer Micelles*, pages 173–210. Springer, Berlin, Heidelberg, (2004).

[7] M. Rey, M. A. Fernandez-Rodriguez, M. Karg, L. Isa, and N. Vogel, *Poly-n-isopropylacrylamide nanogels and microgels at fluid interfaces*, Accounts of Chemical Research **53**, 414 (2020).

[8] M. Rey, X. Hou, J. S. J. Tang, and N. Vogel, *Interfacial arrangement and phase transitions of PNiPAm microgels with different crosslinking densities*, Soft Matter **13**, 8717 (2017).

[9] F. A. Plamper and W. Richtering, *Functional Microgels and Microgel Systems*, Accounts of Chemical Research **50**, 131 (2017).

[10] Z. Li and T. Ngai, *Microgel particles at the fluid-fluid interfaces*, Nanoscale **5**, 1399 (2013).

[11] T. Ngai, S. H. Behrens, and H. Auweter, *Novel emulsions stabilized by pH and temperature sensitive microgels*, Chemical Communications (2005).

[12] V. Schmitt and V. Ravaine, *Surface compaction versus stretching in Pickering emulsions stabilised by microgels*, Current Opinion in Colloid and Interface Science **18**, 532 (2013).

[13] M. A. Fernandez-Rodriguez, A. Martín-Molina, and J. Maldonado-Valderrama, *Microgels at interfaces, from mickering emulsions to flat interfaces and back*, Advances in Colloid and Interface Science **288**, 102350 (2020).

[14] M.-C. Tatry, P. Galanopoulo, L. Waldmann, V. Lapeyre, P. Garrigue, V. Schmitt, and V. Ravaine, *Pickering emulsions stabilized by thermoresponsive oligo(ethylene glycol)-based microgels: Effect of temperature-sensitivity on emulsion stability*, Journal of Colloid and Interface Science **589**, 96 (2021).

[15] D. Klinger and K. Landfester, *Stimuli-responsive microgels for the loading and release of functional compounds: Fundamental concepts and applications*, Polymer **53**, 5209 (2012).

[16] M. Karg, A. Pich, T. Hellweg, T. Hoare, L. A. Lyon, J. J. Crassous, D. Suzuki, R. A. Gumerov, S. Schneider, I. I. Potemkin, and W. Richtering, *Nanogels and Microgels: From Model Colloids to Applications, Recent Developments, and Future Trends*, Langmuir **35**, 6231 (2019).

[17] Z. Yang, L. Yang, Z. Zhang, N. Wu, J. Xie, and W. Cao, *Hollow spheres of silver synthesized using polyelectrolyte capsules as microreactors*, Colloids and Surfaces A: Physicochemical and Engineering Aspects **312**, 113 (2008).

[18] N. Liu, S. Zhao, Z. Yang, and B. Liu, *Patchy Templated Synthesis of Macroporous Colloidal Hollow Spheres and Their Application as Catalytic Microreactors*, ACS Applied Materials & Interfaces **11**, 47008 (2019).

[19] M. Motornov, Y. Roiter, I. Tokarev, and S. Minko, *Stimuli-responsive nanoparticles, nanogels and capsules for integrated multifunctional intelligent systems*, Progress in Polymer Science **35**, 174 (2010).

[20] S. Förster and T. Plantenberg, *From Self-Organizing Polymers to Nanohybrid and Biomaterials*, Angewandte Chemie International Edition **41**, 688 (2002).

[21] D. M. Heyes and P. J. Aston, *Square-well and square-shoulder fluids: Simulation and equations of state*, The Journal of Chemical Physics **97**, 5738 (1992).

[22] P. Bolhuis and D. Frenkel, *Isostructural solid-solid transitions in systems with a repulsive 'shoulder' potential*, Journal of Physics: Condensed Matter **9**, 381 (1997).

[23] A. R. Denton and H. Löwen, *Isostructural solid-solid transitions in square-shoulder systems*, Journal of Physics: Condensed Matter **9**, L1 (1997).

[24] E. A. Jagla, *Phase behavior of a system of particles with core collapse*, Physical Review E **58**, 1478 (1998).

[25] G. Malescio and G. Pellicane, *Stripe phases from isotropic repulsive interactions*, Nature Materials **2**, 97 (2003).

[26] G. J. Pauschenwein and G. Kahl, *Zero temperature phase diagram of the square-shoulder system*, The Journal of Chemical Physics **129**, 174107 (2008).

[27] S. B. Yuste, A. Santos, and M. López de Haro, *Structure of the square-shoulder fluid*, Molecular Physics **109**, 987 (2011).

[28] Y. Norizoe and T. Kawakatsu, *Particle Monte Carlo simulation of string-like colloidal assembly in two and three dimensions*, The Journal of Chemical Physics **137**, 024904 (2012).

[29] H. Pattabhiraman, A. P. Gantapara, and M. Dijkstra, *On the stability of a quasicrystal and its crystalline approximant in a system of hard disks with a soft corona*, The Journal of Chemical Physics **143**, 164905 (2015).

[30] A. Gabriëlse, H. Löwen, and F. Smallenburg, *Low-Temperature Crystal Structures of the Hard Core Square Shoulder Model*, Materials **10**, 1280 (2017).

[31] W. R. C. Somerville, A. D. Law, M. Rey, N. Vogel, A. J. Archer, and D. M. A. Buzza, *Pattern formation in two-dimensional hard-core/soft-shell systems with variable soft shell profiles*, Soft Matter **16**, 3564 (2020).

[32] A. Ivlev, G. Morfill, H. Löwen, and C. P. Royall, *Complex Plasmas and Colloidal Dispersions: Particle-resolved Studies of Classical Liquids and Solids* (World Scientific Publishing Company, Singapore, 2012).

[33] U. Gasser, *Crystallization in three-and two-dimensional colloidal suspensions*, Journal of Physics: Condensed Matter **21**, 203101 (2009).

[34] F. Wang, Z. Zheng, Y. Peng, Y. Han, and Z. Wang, *Imaging the Homogeneous Nucleation During the Melting of Superheated Colloidal Crystals*, Science **338**, 87 (2012).

[35] A. M. Alsayed, M. F. Islam, J. Zhang, P. J. Collings, and A. G. Yodh, *Premelting at Defects Within Bulk Colloidal Crystals*, Science **309**, 1207 (2005).

[36] Y. Peng, F. Wang, Z. Wang, A. M. Alsayed, Z. Zhang, A. G. Yodh, and Y. Han, *Two-step nucleation mechanism in solid-solid phase transitions*, Nature Materials **14**, 101 (2015).

[37] F. Grillo, M. A. Fernandez-Rodriguez, M. N. Antonopoulou, D. Gerber, and L. Isa, *Self-templating assembly of soft microparticles into complex tessellations*, Nature **582**, 219 (2020).

[38] S. Ciarella, M. Rey, J. Harrer, N. Holstein, M. Ickler, H. Löwen, N. Vogel, and L. M. C. Janssen, *Soft Particles at Liquid Interfaces: From Molecular Particle Architecture to Collective Phase Behavior*, Langmuir **37**, 5364 (2021).

[39] K. Volk, F. Deißenbeck, S. Mandal, H. Löwen, and M. Karg, *Moiré and honeycomb lattices through self-assembly of hard-core/soft-shell microgels: experiment and simulation*, Physical Chemistry Chemical Physics **21**, 19153 (2019).

[40] K. Shiraga, H. Naito, T. Suzuki, N. Kondo, and Y. Ogawa, *Hydration and Hydrogen Bond Network of Water during the Coil-to-Globule Transition in Poly(N -isopropylacrylamide) Aqueous Solution at Cloud Point Temperature*, Journal of Physical Chemistry B **119**, 5576 (2015).

[41] R. Keidel, A. Ghavami, D. M. Lugo, G. Lotze, O. Virtanen, P. Beumers, J. S. Pedersen, A. Bardow, R. G. Winkler, and W. Richtering, *Time-resolved structural evolution during the collapse of responsive hydrogels: The microgel-to-particle transition*, Science Advances **4**, (2018).

[42] G. M. Conley, S. Nöjd, M. Braibanti, P. Schurtenberger, and F. Scheffold, *Superresolution microscopy of the volume phase transition of pNIPAM microgels*, Colloids and Surfaces A: Physicochemical and Engineering Aspects **499**, 18 (2016).

[43] K. Kratz, T. Hellweg, and W. Eimer, *Structural changes in PNIPAM microgel particles as seen by SANS, DLS, and EM techniques*, Polymer **42**, 6631 (2001).

[44] L. Rovigatti, N. Gnan, and E. Zaccarelli, *Internal structure and swelling behaviour of in silico microgel particles*, Journal of Physics Condensed Matter **30**, 044001 (2018).

[45] F. Camerin, N. Gnan, L. Rovigatti, and E. Zaccarelli, *Modelling realistic microgels in an explicit solvent*, Scientific Reports **8**, 14426 (2018).

[46] N. Gnan, L. Rovigatti, M. Bergman, and E. Zaccarelli, *In Silico Synthesis of Microgel Particles*, Macromolecules **50**, 8777 (2017).

[47] G. Del Monte, A. Ninarello, F. Camerin, L. Rovigatti, N. Gnan, and E. Zaccarelli, *Numerical insights on ionic microgels: structure and swelling behaviour*, Soft Matter **15**, 8113 (2019).

[48] A. J. Moreno and F. Lo Verso, *Computational investigation of microgels: synthesis and effect of the microstructure on the deswelling behavior*, Soft Matter **14**, 7083 (2018).

[49] T. J. Weyer and A. R. Denton, *Concentration-dependent swelling and structure of ionic microgels: simulation and theory of a coarse-grained model*, Soft Matter **14**, 4530 (2018).

[50] M. Quesada-Pérez, J. Ramos, J. Forcada, and A. Martín-Molina, *Computer simulations of thermo-sensitive microgels: Quantitative comparison with experimental swelling data*, The Journal of Chemical Physics **136**, 244903 (2012).

[51] M. Brugnoni, A. Scotti, A. A. Rudov, A. P. Gelissen, T. Caumanns, A. Radulescu, T. Eckert, A. Pich, I. I. Potemkin, and W. Richtering, *Swelling of a Responsive Network within Different Constraints in Multi-Thermosensitive Microgels*, Macromolecules **51**, 2662 (2018).

[52] A. Scotti, A. R. Denton, M. Brugnoni, J. E. Houston, R. Schweins, I. I. Potemkin, and W. Richtering, *Deswelling of Microgels in Crowded Suspensions Depends on Cross-Link Density and Architecture*, Macromolecules **52**, 3995 (2019).

[53] S. Nikolov, A. Fernandez-Nieves, and A. Alexeev, *Mesoscale modeling of microgel mechanics and kinetics through the swelling transition*, Applied Mathematics and Mechanics **39**, 47 (2018).

[54] A. R. Denton and Q. Tang, *Counterion-induced swelling of ionic microgels*, The Journal of Chemical Physics **145**, 164901 (2016).

[55] M. M. Hedrick, J. K. Chung, and A. R. Denton, *Structure and osmotic pressure of ionic microgel dispersions*, The Journal of Chemical Physics **142**, 034904 (2015).

[56] G. Giupponi, D. M. A. Buzza, and D. B. Adolf, *Are Polyelectrolyte Dendrimers Stimuli Responsive?*, Macromolecules **40**, 5959 (2007).

[57] Y. Hertle, M. Zeiser, C. Hasenöhrl, P. Busch, and T. Hellweg, *Responsive P (NIPAM-co-NtBAM) microgels: Flory–Rehner description of the swelling behaviour*, Colloid and Polymer Science **288**, 1047 (2010).

[58] C. G. Lopez and W. Richtering, *Does Flory-Rehner theory quantitatively describe the swelling of thermoresponsive microgels?*, Soft Matter **13**, 8271 (2017).

[59] D. Zhi, Y. Huang, X. Han, H. Liu, and Y. Hu, *A molecular thermodynamic model for temperature- and solvent-sensitive hydrogels, application to the swelling behavior of PNIPAm hydrogels in ethanol/water mixtures*, Chemical Engineering Science **65**, 3223 (2010).

[60] W. Toh, T. Y. Ng, J. Hu, and Z. Liu, *Mechanics of inhomogeneous large deformation of photo-thermal sensitive hydrogels*, International Journal of Solids and Structures **51**, 4440 (2014).

[61] U. Baul and J. Dzubiella, *Structure and dynamics of responsive colloids with dynamical polydispersity*, Journal of Physics: Condensed Matter **33**, 174002 (2021).

[62] Y. C. Lin, B. Rotenberg, and J. Dzubiella, *Structure and position-dependent properties of inhomogeneous suspensions of responsive colloids*, Physical Review E **102**, 042602 (2020).

[63] A. Moncho-Jordá and J. Dzubiella, *Swelling of ionic microgel particles in the presence of excluded-volume interactions: a density functional approach*, Physical Chemistry Chemical Physics **18**, 5372 (2016).

[64] G. Giupponi and D. M. A. Buzza, *Monte carlo simulation of dendrimers in variable solvent quality*, The Journal of Chemical Physics **120**, 10290 (2004).

[65] S. Babaee, J. Shim, J. C. Weaver, E. R. Chen, N. Patel, and K. Bertoldi, *3D soft metamaterials with negative Poisson's ratio*, Advanced Materials **25**, 5044 (2013).

[66] Y. Jiang and Y. Li, *3D Printed Auxetic Mechanical Metamaterial with Chiral Cells and Re-entrant Cores*, Scientific Reports **8**, 2397 (2018).

[67] Y. Kim, H. Yuk, R. Zhao, S. A. Chester, and X. Zhao, *Printing ferromagnetic domains for untethered fast-transforming soft materials*, Nature **558**, 274 (2018).

[68] K. E. Evans, *Auxetic polymers: a new range of materials*, Endeavour **15**, 170 (1991).

[69] F. Bresme and M. Oettel, *Nanoparticles at fluid interfaces*, Journal of Physics: Condensed Matter **19**, 413101 (2007).

[70] J. Harrer, M. Rey, S. Ciarella, H. Löwen, L. M. Janssen, and N. Vogel, *Stimuli-Responsive Behavior of PNiPAm Microgels under Interfacial Confinement*, Langmuir **35**, 10512 (2019).

[71] J. Kolker, J. Harrer, S. Ciarella, M. Rey, M. Ickler, L. M. C. Janssen, N. Vogel, and H. Löwen, *Interface-induced hysteretic volume phase transition of microgels: simulation and experiment*, Soft Matter **17**, 5581 (2021).

[72] E. S. A. Goerlitzer, R. Mohammadi, S. Nechayev, K. Volk, M. Rey, P. Banzer, M. Karg, and N. Vogel, *Chiral Surface Lattice Resonances*, Advanced Materials **32**, 2001330 (2020).

[73] M. Rey, R. Elnathan, R. Ditcovski, K. Geisel, M. Zanini, M. A. Fernandez-Rodriguez, V. V. Naik, A. Frutiger, W. Richtering, T. Ellenbogen, N. H. Voelcker, and L. Isa, *Fully Tunable Silicon Nanowire Arrays Fabricated by Soft Nanoparticle Templating*, Nano Letters **16**, 157 (2016).

[74] S. Bochenek, A. Scotti, W. Ogieglo, M. Á. Fernández-Rodríguez, M. F. Schulte, R. A. Gumerov, N. V. Bushuev, I. I. Potemkin, M. Wessling, L. Isa, and W. Richtering, *Effect of the 3D Swelling of Microgels on Their 2D Phase Behavior at the Liquid-Liquid Interface*, Langmuir **35**, 16780 (2019).

[75] S. Bochenek, A. Scotti, and W. Richtering, *Temperature-sensitive soft microgels at interfaces: air–water versus oil–water*, Soft Matter **17**, 976 (2021).

[76] F. Camerin, N. Gnan, J. Ruiz-Franco, A. Ninarello, L. Rovigatti, and E. Zaccarelli, *Microgels at Interfaces Behave as 2D Elastic Particles Featuring Reentrant Dynamics*, Physical Review X **10**, 031012 (2020).

[77] F. Camerin, M. A. Fernández-Rodríguez, L. Rovigatti, M.-N. Antonopoulou, N. Gnan, A. Ninarello, L. Isa, and E. Zaccarelli, *Microgels Adsorbed at Liquid–Liquid Interfaces: A Joint Numerical and Experimental Study*, ACS Nano **13**, 4548 (2019).

[78] F. Barahona, E. Turiel, P. A. G. Cormack, and A. Martín-Esteban, *Chromatographic performance of molecularly imprinted polymers: Core-Shell microspheres by precipitation polymerization and grafted MIP films via iniferter-modified silica beads*, Journal of Polymer Science: Part A: Polymer Chemistry **48**, 1058 (2010).

[79] N. Marchyk, J. Maximilien, S. Beyazit, K. Haupt, and B. T. S. Bui, *One-pot synthesis of iniferter-bound polystyrene core nanoparticles for the controlled grafting of multilayer shells*, Nanoscale **6**, 2872 (2014).

[80] P. Liu and Z. Su, *Preparation of polystyrene grafted silica nanoparticles by two-steps UV induced reaction*, Journal of Photochemistry and Photobiology A: Chemistry **167**, 237 (2004).

[81] D. Vlassopoulos and G. Fytas. *From Polymers to Colloids: Engineering the Dynamic Properties of Hairy Particles*, pages 1–54. Springer Berlin Heidelberg, (2010).

[82] J. Menath, J. Eatson, R. Brilmayer, A. Andrieu-Brunsen, D. M. A. Buzza, and N. Vogel, *Defined core–shell particles as the key to complex interfacial self-assembly*, Proceedings of the National Academy of Sciences **118**, (2021).

[83] E. A. Jagla, *Minimum energy configurations of repelling particles in two dimensions*, The Journal of Chemical Physics **110**, 451 (1999).

[84] C. N. Likos, H. Löwen, M. Watzlawek, B. Abbas, O. Jucknischke, J. Allgaier, and D. Richter, *Star Polymers Viewed as Ultrasoft Colloidal Particles*, Physical Review Letters **80**, 4450 (1998).

[85] M. Watzlawek, C. N. Likos, and H. Löwen, *Phase Diagram of Star Polymer Solutions*, Physical Review Letters **82**, 5289 (1999).

[86] A. Lang, C. N. Likos, M. Watzlawek, and H. Löwen, *Fluid and solid phases of the Gaussian core model*, Journal of Physics: Condensed Matter **12**, 5087 (2000).

[87] R. W. Style, L. Isa, and E. R. Dufresne, *Adsorption of soft particles at fluid interfaces*, Soft Matter **11**, 7412 (2015).

[88] J. Hegemann, H.-H. Boltz, and J. Kierfeld, *Elastic capsules at liquid–liquid interfaces*, Soft Matter **14**, 5665 (2018).

[89] Z. Li, W. Richtering, and T. Ngai, *Poly(N-isopropylacrylamide) microgels at the oil-water interface: temperature effect*, Soft Matter **10**, 6182 (2014).

[90] P.-G. De Gennes, F. Brochard-Wyart, D. Quéré, et al., *Capillarity and Wetting Phenomena: Drops, Bubbles, Pearls, Waves* (Springer, New York, 2004).

[91] Y. Levin, *Thermodynamics of Surface Tension: Application to Electrolyte Solutions*, Journal of Statistical Physics **110**, 825 (2003).

[92] P. R. Couchman, W. A. Jesser, D. Kuhlmann-Wilsdorf, and J. P. Hirth, *On the concepts of surface stress and surface strain*, Surface Science **33**, 429 (1972).

[93] P. R. Couchman and W. A. Jesser, *On the thermodynamics of surfaces*, Surface Science **34**, 212 (1973).

[94] P. R. Couchman and D. H. Everett, *A comment on certain parameters and equations in surface thermodynamics*, Journal of Electroanalytical Chemistry and Interfacial Electrochemistry **67**, 382 (1976).

[95] R. G. Linford, *The Derivation of Thermodynamic Equations for Solid Surfaces*, Chemical Reviews **78**, 81 (1978).

[96] M. E. Schrader, *Young-Dupre Revisited*, Langmuir **11**, 3585 (1995).

[97] L. Landau and E. Lifshitz, *Theory of Elasticity (Third Edition)* (Butterworth-Heinemann, Oxford, England, 1986).

[98] M. Doi and S. F. Edwards, *The Theory of Polymer Dynamics* (Oxford University Press, Oxford, England, 1988).

[99] P.-G. De Gennes, *Scaling Concepts in Polymer Physics* (Cornell University Press, Ithaca, NY, 1979).

[100] J. D. Weeks, D. Chandler, and H. C. Andersen, *Role of Repulsive Forces in Determining the Equilibrium Structure of Simple Liquids*, The Journal of Chemical Physics **54**, 5237 (1971).

[101] J.-P. Hansen and I. R. McDonald, *Theory of Simple Liquids: with Applications to Soft Matter* (Academic press, Oxford, England, 2013).

[102] P. J. Flory, *Principles of Polymer Chemistry* (Cornell University Press, Ithaca, NY, 1953).

[103] M. Quesada-Pérez, J. A. Maroto-Centeno, J. Forcada, and R. Hidalgo-Alvarez, *Gel swelling theories: the classical formalism and recent approaches*, Soft Matter **7**, 10536 (2011).

[104] T. Soddemann, B. Dünweg, and K. Kremer, *A generic computer model for amphiphilic systems*, The European Physical Journal E **6**, 409 (2001).

[105] P. Langevin, *Sur la théorie du mouvement brownien*, Compt. Rendus **146**, 530 (1908).

[106] I. Snook, *The Langevin and Generalised Langevin Approach to the Dynamics of Atomic, Polymeric and Colloidal Systems* (Elsevier, Oxford, England, 2006).

[107] A. Einstein, *Über die von der Molekularkinetischen Theorie der Wärme geforderte Bewegung von in ruhenden Flüssigkeiten suspendierten Teilchen*, Annalen der Physik **4**, 549 (1905).

[108] A. L. B. Cauchy, *Exercices de mathématiques* (De Bure Frères, 1828).

[109] L. Verlet, *Computer "Experiments" on Classical Fluids. I. Thermodynamical Properties of Lennard-Jones Molecules*, Physical Review **159**, 98 (1967).

[110] J. A. Anderson, J. Glaser, and S. C. Glotzer, *HOOMD-blue: A Python package for high-performance molecular dynamics and hard particle Monte Carlo simulations*, Computational Materials Science **173**, 109363 (2020).

[111] F. E. Harris, *Mathematics for Physical Science and Engineering: Symbolic Computing Applications in Maple and Mathematica* (Academic Press, Waltham, USA, 2014).

[112] A. Stukowski, *Visualization and analysis of atomistic simulation data with OVITO–the Open Visualization Tool*, Modelling and Simulation in Materials Science and Engineering **18**, 015012 (2010).

[113] B. Keinert, M. Innmann, M. Sänger, and M. Stamminger, *Spherical Fibonacci Mapping*, ACM Transactions on Graphics **34**, 193 (2015).

[114] R. Marques, C. Bouville, M. Ribardière, L. P. Santos, and K. Bouatouch. *Spherical Fibonacci Point Sets for Illumination Integrals.* in *Computer Graphics Forum*, volume 32, pages 134–143. Wiley Online Library, (2013).

[115] A. Mielke and F. Theil, *On rate-independent hysteresis models*, Nonlinear Differential Equations and Applications NoDEA **11**, 151 (2004).

[116] A. Mielke, in *Handbook of Differential Equations Evolutionary Equations*, edited by C. Dafermos and E. Feireisl (Amsterdam, North-Holland, 2005).

[117] B. Schweizer, *Partielle Differentialgleichungen* (Springer, Berlin, 2013).